A SPECTRAL ANALYSIS OF THE POLARISATION OF DRIFTING SUB-PULSES

A THESIS SUBMITTED TO AUCKLAND UNIVERSITY OF TECHNOLOGY IN PARTIAL FULFILMENT OF THE REQUIREMENTS FOR THE DEGREE OF MASTER OF SCIENCE (RESEARCH)

Supervisors
A. Prof. W. van Straten
Prof. S. Gulyaev

2023

By
Ander Castelltort Schnaas
School of Engineering, Computer and Mathematical Sciences

Abstract

Pulsars are among the most extreme objects in the Universe. Each one is born during a supernova – a dramatic explosion that happens when a bright star many times bigger than our Sun runs out of fuel. The heavy core of the star collapses under its own weight into something more dense than the nucleus of an atom. Each pulsar has an inferred magnetic field that is millions of times stronger than any that can be produced here on the Earth. Like a cosmic lighthouse, this magnetic field generates beams that sweep across the Galaxy with each rotation of the star (Gold, 1968; Pacini, 1968); however, the underlying physics of the pulsar emission mechanism remains poorly understood after decades of study (Melrose & Yuen, 2016). Unlike the steady beam of a lighthouse, a pulsar's beam crackles and pops with lightning-like discharges of energy (Ruderman & Sutherland, 1975). By studying this highly dynamic signal, we learn about what generates the radio waves and what happens as they travel through the turbulent plasma in the pulsar's strong magnetic field.

A relatively rare number of pulsars exhibit quasi-periodic variations in the polarisation state of their emission (e.g. Primak et al., 2022). To provide new insight into the origin of this behaviour, we developed a novel statistical method, based on Principal Component Analysis of the Fourier Transforms of the Stokes parameters, that extends the work of Edwards (2004) such that it can be applied in the case of quasi-periodic polarisation fluctuations. We apply this technique to the first-discovered pulsar, compare and contrast the results with previous work, and present the first detection of quasi-periodic drift frequency modulation. The method can be applied to a wide range of radio pulsars in order to obtain a quantitative measure of the fraction of pulsars that exhibit quasi-periodic polarisation fluctuations. In doing so, the techniques developed for this research project will provide new experimental constraints on theories of radio emission and propagation in the pulsar magnetosphere, and facilitate a deeper understanding of the physics of relativistic plasmas in strong magnetic fields.

Contents

List of Figures

Attestation of Authorship

I hereby declare that this submission is my own work and that, to the best of my knowledge and belief, it contains no material previously published or written by another person nor material which to a substantial extent has been accepted for the qualification of any other degree or diploma of a university or other institution of higher learning.

Signature of student

Acknowledgements

The ideas for the research presented in this thesis were proposed by my supervisor, A. Prof. W. van Straten, whom I greatly thank for the opportunity to study one of the most extreme objects in the Universe. Your wealth of knowledge in the field, coupled with your ability to provide clear and illuminating explanations, has been instrumental in broadening my horizons and deepening my understanding of pulsar astronomy. With many thanks to Prof. T. S. Gulyaev, who stepped in as supervisor in untimely circumstances, for his challenging feedback and guidance throughout this project. The stimulating discussions were key to forming a comprehensive and objective critique.

I would like to thank my closest friends who have helped me throughout my journey at university: James Steyn (Bookclub Eric, Kingofdahighway, Jeyn), from late night walks to sharing in quiet-brain-mode, your unwavering friendship and devil's advocacy have been a constant source of inspiration; Hannah Wetzel, the Sun across my library, you have made the highs higher and the lows more manageable. Thank you for the constant encouragement to excel, even when we are still in the computer labs late at night and security comes to lock up; and Stella Pearless, for being the sounding board to my writing (accompanied by many coffees and almond croissants). Progress beyond writer's block can only be attributed to your patience. I am grateful for the enduring friendship from you all.

To my parents, Javier and Vivianne, whom I owe everything to. Your sacrifices, loving support, and promotive guidance have allowed me to pursue my ambitions, for which I am endlessly grateful.

Chapter 1

Introduction

1.1 Discovery of Pulsars

PSR B1919+21 is the first pulsar discovered by Jocelyn Bell in 1967 (Hewish et al., 1968). During a survey for compact extragalactic radio sources, Bell noticed unusual "bits of scruff" in the chart-recorder data, which were barely distinguishable from the surrounding noise in which it was buried. However, these anomalies reappeared exactly once every sidereal day, leading Bell to suggest that the source was of astronomical origin and located outside of our Solar System. Subsequent analysis revealed that the source was rapidly pulsating with remarkable precision and believed to be associated with the radio emission from a white dwarf or neutron star within our own galaxy.

The discovery of pulsars by Jocelyn Bell was a major scientific breakthrough that revolutionised our understanding of the Universe. Pulsars provided the first direct evidence for the existence of neutron stars (hypothesised by Baade & Zwicky, 1934), which are extremely dense, highly magnetised collapsed cores of massive stars that have exploded in supernovae. Additionally, pulsars provided the first concrete evidence for the existence of strong magnetic fields in the Universe, which are thought to play a key role in many astrophysical phenomena, such as the acceleration of cosmic rays and

the emission of jets from black holes.

Pulsars are also extremely stable clocks, with periods that can vary by only a few millionths of a second over billions of years. This makes them useful for a variety of applications, including the study of gravity (Kramer et al., 2006), the search for exoplanets (Wolszczan & Frail, 1992), and the measurement of galactic distances (Deller et al., 2009). The discovery of pulsars also opened new areas of research in astrophysics, including the study of the properties and evolution of neutron stars, including the equation of state of ultra-dense matter (Demorest et al., 2010), the physics of strong magnetic fields, and the mechanisms by which pulsars emit their radiation.

Jocelyn Bell's pioneering discovery of pulsars was a major breakthrough in the understanding of the Universe. Despite her fundamental contribution to the field, she was not recognised with a Nobel Prize in Physics in 1974, which was awarded solely to Antony Hewish and Martin Ryle. However, in 2018, Bell was awarded the Special Breakthrough Prize in Fundamental Physics, a true testament to her pioneering work and impact in the field of astrophysics.

1.2 Pulsar Structure and Electrodynamics

Rotating magnetic neutron stars are pulsating radio sources (Gold, 1968; Pacini, 1968), and are considered to be one of the most extreme objects in the Universe. Neutron stars originate from the collapsed cores of massive supergiant stars (Baade & Zwicky, 1934), about 9 to 25 times the mass of the Sun (Heger et al., 2003), that have reached the end of their stellar life cycle and undergone supernova explosions. As the stellar core implodes, conservation of angular momentum causes the rate of rotation to increase, much like that of a figure skater when they draw in their arms to spin faster. Young neutron stars rotate up to several hundred times per second and have inferred magnetic fields millions of times stronger than Earth's. This makes them unique natural laboratories

that cannot be found or reproduced anywhere in the Universe. Studying the radio signals from pulsars will enable a deeper understanding of the physics of radio wave emission and propagation in the ultra-relativistic plasma embedded in the pulsar's ultra-strong magnetic field.

Goldreich and Julian (1969) elucidated the simplest model, that is, of a rapidly rotating neutron star with a strong dipole magnetic field whose axis is aligned with the rotation axis. Its surrounding magnetosphere is embedded with a population of charged particles that corotate with the neutron star out to a distance known as the light cylinder, at which the corotating speed reaches the speed of light and exact corotation can no longer be maintained. Magnetic field lines within the corotating magnetospheric region close; those that cross the light cylinder remain open and charged particles flow along them. These streaming particles emit narrow beams of radiation that can span the electromagnetic spectrum from radio to gamma rays (Abdo et al., 2010). When the neutron star rotates about an axis different from that of the magnetic field, an oblique configuration applies (Pacini, 1968), and the polar beams sweep through interstellar space like a cosmic lighthouse (Gold, 1968). An observer in the line of sight of the beams will then detect a pulse of radiation at a rate that corresponds to the rotational period of the pulsar. Every rotation of the neutron star provides a window of insight into the physical phenomena that occur in the pulsar magnetosphere. However, after decades of study, the emission and propagation of radio waves in the pulsar magnetosphere remains poorly understood (Melrose & Yuen, 2016).

1.3 Possible Radio Emission Mechanisms

To better understand the electrodynamics of pulsars, we need to carefully study their radio emission. Possible mechanisms include coherent curvature emission, relativistic plasma emission and linear acceleration emission, among others; however, there is no

consensus on which is the most plausible (Melrose & Yuen, 2016).

Coherent curvature emission (CE) occurs when the charged particles that stream along the open magnetic field lines are accelerated by the Lorentz Force in a direction perpendicular to the field lines (Chugunov et al., 1975). This acceleration causes particles to emit curvature radiation, which is analogous to synchrotron emission. The radio emission produced by these highly relativistic charges is confined within a narrow beam that is tangent to the charged particle's trajectory along the open magnetic field lines. It is observed only if the beam sweeps the line of sight of an observer.

The relativistic plasma emission (RPE) process involves the generation of Langmuir-like waves through a beam instability, followed by partial conversion of the wave energy into escaping radiation. Langmuir waves, which are longitudinal plasma waves generated by the collective motion of electrons in a plasma, can be excited by high-energy electrons present in the pulsar magnetosphere. This can lead to the acceleration of particles to high energies and the generation of radio emission. However, the applicability of RPE to a pulsar magnetosphere is limited by certain challenges. Firstly, the existence of Langmuir-like waves in a pulsar plasma is only plausible under specific conditions, such as satisfying the Cerenkov resonance condition, which states that the phase velocity of the wave must be greater than the velocity of the particles in the plasma (Melrose & Gedalin, 1999). This condition is difficult to satisfy in a pulsar plasma, as it typically only occurs near the light cylinder in plasmas with a relativistic spread in energies. Secondly, the partial conversion of Langmuir-like wave energy into escaping radiation by nonlinear processes is an inefficient process, referred to as a 'bottleneck' (Usov, 2000). However, detailed investigations of the dispersive properties of plasma revealed that no nonlinear conversion is needed to produce escaping radiation, avoiding the problem of the 'bottleneck' in the conversion process entirely (Melrose & Gedalin, 1999; Melrose et al., 1999). Melrose and Yuen (2016) suggest that a variation of this form of plasma emission could be the most plausible pulsar radio emission mechanism.

In linear-acceleration emission (LAE), the acceleration of a charge is attributed to a non-zero parallel electric field, in which the acceleration of the charge is parallel to its velocity (Cocke, 1973; Melrose, 1978; Kroll & McMullin, 1979). An assumption of the simplest model is that the $E_{\|}$ oscillates with some frequency ω_0 and deviates the motion of a particle. The emitted radiation then satisfies the Cerenkov resonance $\omega - \mathbf{k} \cdot \mathbf{v} = \omega_0$, giving $\omega - \mathbf{k} \cdot \mathbf{v} \approx \gamma^2 \omega_0 / 2$ for emission in a vacuum by a highly relativistic particle. If the oscillation of $E_{\|}$ is associated with a propagating wave, then ω_0 is replaced by $\omega_0 - \mathbf{k}_0 \cdot v$, where $\mathbf{k}_0$ is the wave vector of the propagating wave. LAE in the form of maser emission is a possible interpretation of the radio emission mechanism (Melrose, 1978), where the amplification associated with LAE is possible for frequencies $\omega \ll \omega_0 \gamma^2$, provided the particle distribution satisfies additional constraints (Melrose, 2017). Although a maser-like LAE is possible, it has not been shown to be a plausible pulsar radio emission mechanism because the assumption that $E_{\|}$ perturbs the motion of a particle is not satisfied for oscillations with large amplitudes.

1.4 Observational Properties of the Pulsar Radio Signal

In parallel with progress on theoretical models of the pulsar emission mechanism, astronomers have been developing new methods of observing radio pulsars. Soon after the discovery of pulsars, it was noted that some exhibited periodic drifting of sub-pulse emission structure (Drake & Craft, 1968); however, the underlying physics remains poorly understood. A recent large study of the sub-pulse modulation properties of approximately 1200 pulsars found that about 35% of them exhibit drifting sub-pulses, suggesting that drifting sub-pulses are a common phenomenon among radio pulsars, and may be detectable in an estimated 60% of the overall pulsar population, assuming that integrated pulse profiles with $\mathrm{S/N} \sim 1000$ can be observed (Song et al., 2023).

Ruderman and Sutherland (1975) suggested the now well-established rotating carousel model to describe the drifting sub-pulse phenomenon, in which the primary beam of radio emission consists of sub-beams that circulate around the magnetic pole of the pulsar due to an $\mathbf{E} \times \mathbf{B}$ drift force, where $\mathbf{E}$ and $\mathbf{B}$ are the electric and magnetic fields, respectively, near the polar cap. Such sub-beams correspond to the sub-pulses, and because of the carousel motion, each sub-beam steadily drifts across the primary beam of emission. The sub-beams are observed to systematically drift as a function of pulse longitude (depicted in Figure 1.1).

The two periodicities, P_2 and P_3, define the pattern of the oblique intensity band structures, where P_2 is the longitudinal interval between two successive sub-pulses in a single pulse, and P_3 is the temporal separation between the diagonal drift bands (e.g. at a fixed longitude). The phenomenon has been studied using a wide variety of techniques. For example, Backer (1973) developed the fluctuation spectral analysis approach to study drifting of the total intensity in the pulsar spin-frequency domain. The longitude-resolved fluctuation spectrum (LRFS; Backer, 1973) is the result of computing multiple one-dimensional discrete Fourier transforms of the total intensity of contiguous single-pulse sequences, each one at a different pulse longitude, and provides information on the periodic amplitude modulation due to the drifting sub-pulses. Backer had the notion that a generalised drifting-sub-pulse phenomenon was responsible for all short-period systematic variations of pulse energies and explicitly showed this for PSR B1919+21 (Backer, 1970); however, no convincing physical interpretation of sub-pulse variability was known at the time. It was not until 1975 that the carousel model was introduced (Ruderman & Sutherland, 1975), and then later revised to include interpretations for the relatively rare drift-synchronous switching between orthogonally polarised modes (Rankin & Ramachandran, 2003).

An observational approach that explores the polarisation characteristics of pulsar radio emission is integral to understanding the coherent radio emission. The observed

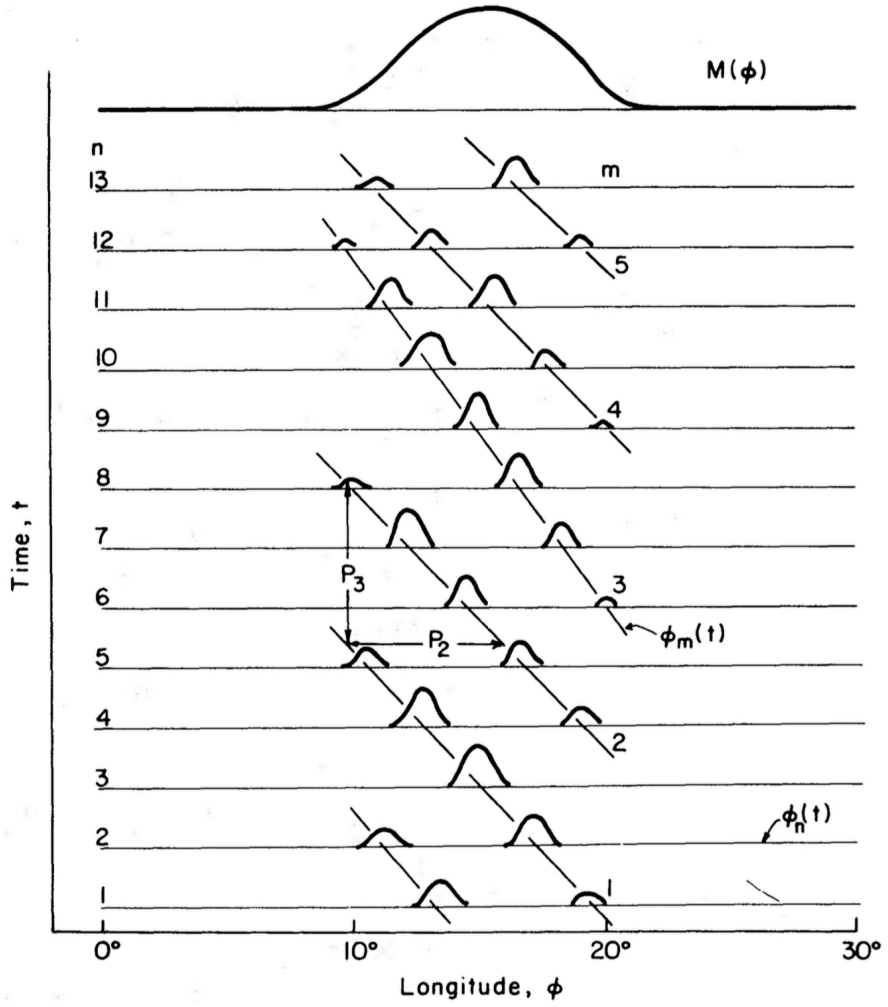

Figure 1.1: Schematic (after Backer 1973) of an integrated pulse profile, arrival times of individual pulses, and definition of P_2 and P_3 for those pulsars showing the "drifting sub-pulse" phenomenon. Arrival times of individual pulses are given in terms of a longitude for which 360° corresponds to the full pulsar period [from Ruderman and Sutherland (1975)].

radio emission has been altered by propagation through the pulsar magnetosphere, and it is necessary to understand such processes in order to constrain the physics of both the pulsar radio emission mechanism and the magnetospheric environment. The position angle of the predominantly linear polarisation, as predicted by the inclination of magnetic field lines in the neighbourhood of the polar cap (rotating vector model, RVM; Radhakrishnan & Cooke, 1969), traces a characteristic S-shaped sweep throughout the on-pulse window. While most pulsars in the population exhibit an RVM-like sweep in position angle, a significant number of pulsars deviate from this pattern and display polarisation characteristics that are more complex (Johnston et al., 2022; Oswald et al., 2023).

The RVM is often disrupted by abrupt 90° jumps in the position angle caused by the coexistence of two orthogonally polarised modes (OPMs) of radiation, the Ordinary mode (O mode) and the eXtraordinary mode (X mode) (Stinebring et al., 1984; McKinnon & Stinebring, 2000; McKinnon, 2002), which switch in dominance from one to the other within different parts of the pulse profile (Manchester et al., 1975; Backer et al., 1976).

Early one-dimensional histograms of the position angle of single-pulses integrated over selected regions of pulse longitude revealed bimodal distributions, where two distinct features were separated by about 90°. This provided evidence for the coexistence of the two OPMs (Ekers & Moffet, 1969; Manchester et al., 1975). At the time, this finding appeared to support the RVM's prediction of a characteristic S-shaped sweep in position angle. Even when Manchester et al. (1975) showed the first longitude-resolved position angles over single-pulse variability in total intensity and polarisation, the position angle of the linearly polarised radiation was still observed to vary smoothly between orthogonal angles throughout some of the individual pulses.

Stinebring et al. (1984) introduced two-dimensional longitude-resolved single-pulse position angle histograms. They showed the coexistence of the two OPMs as

two significant overlapping bands separated by 90° and revealed the sharp transitions between the OPMs within a narrow portion of the pulse window. As noted by Ekers and Moffet (1969), Stinebring et al. (1984) found that the degree of linear polarisation decreases where the two OPMs coexisted or sharply switched, resulting in depolarisation of the signal. This is due to the anti-parallel nature of the Stokes polarisation vectors associated with OPMs, which result in an average near zero when summed together incoherently. Several authors (Melrose, 1979; Allen & Melrose, 1982; Arons & Barnard, 1986) suggest that the two OPMs are the two elliptically-polarised natural modes of propagation in the highly relativistic magnetospheric plasma, which is considered a birefringent medium. However, the underlying mechanisms that give rise to the OPMs, and the reasons for their dominance in different parts of the pulse profile, remain uncertain (Ilie et al., 2020).

Edwards and Stappers (2004) took discrete intervals of the pulse profile and projected the distribution of the polarisation state onto the surface of the Poincaré sphere, thereby creating a graphical tool for visually representing the polarisation state in terms of the three polarisation Stokes parameters (Stokes Q, U, and V). Antipodal points on the sphere denote orthogonally polarised states, such that transitions between OPMs would appear as a bimodal distribution on the Poincaré sphere, with significant power at two antipodal points. Unexpectedly, distributions of the polarisation state from the on-pulse window of PSR B0329+54 exhibit an annular distribution, which Edwards and Stappers (2004) found could be modelled in terms of Generalised Faraday Rotation (GFR). Faraday Rotation occurs in the cold, collision-less plasma of the ISM, where the natural modes of propagation are circularly polarised and birefringence causes the linear polarisation state to rotate about the line of sight as a function of radio frequency. In a relativistic plasma like that of the pulsar magnetosphere, the natural modes may be elliptically polarised and birefringence causes the polarisation state to rotate about an axis defined by the linearly-polarised natural modes. Therefore, the observed annular

distributions in Edwards and Stappers (2004) could arise from a partially phase coherent superposition of elliptically-polarised OPMs (cf. Dykes et al., 2021; Oswald et al., 2023).

1.5 Drift-Synchronous Polarisation Variations

In several rare cases, the polarisation state of the radio emission sharply switches between orthogonally polarised modes synchronously with the periodic amplitude modulations of the drifting sub-pulses. To date, drift-synchronous polarisation modulation has been observed in only six pulsars: PSR B0809+74 (Taylor et al., 1971; Ramachandran et al., 2002), PSR B1237+25 (Rankin & Ramachandran, 2003), PSR B0320+39, PSR B0818−13 (Edwards, 2004), PSR B0031−07 (Ilie et al., 2020), and PSR B1919+21 (Primak et al., 2022). Four of these pulsars (PSR B0320+39, PSR B0818−13, PSR B0031−07, and PSR B1919+21) also exhibit periodic modulations in which the Stokes polarisation vector traces a three-dimensional ellipse on each drift cycle. It is currently unknown what fraction of the pulsar population exhibits periodic modulations of the Stokes parameters and there may be more such sources to be discovered through a systematic survey.

Rankin and Ramachandran (2003) proposed a single circulating carousel system to explain the drift-synchronous switching between OPMs. In this model, two spatially separated beams, or "images", of the pulsar radio emission are produced, each corresponding to one of the two natural modes of propagation, or OPMs. For each sub-beam within the primary beam that drifts through the line of sight of an observer, the polarisation state will switch between the OPMs. Spatially separated and orthogonally polarised beams would be a natural consequence of birefringence in the pulsar magnetosphere (Rankin et al., 2006). The X mode is not affected by refraction; thus it propagates in a straight path from where it was emitted. The O mode experiences refraction and

propagates on a curved path before escaping the pulsar magnetosphere (Petrova & Lyubarskii, 2000; Petrova, 2001; Lyutikov, 2002; Weltevrede et al., 2003). Refraction allows radiation from emission regions not directly beneath the line of sight to be observed, which complicates the physical interpretation of the observable properties of the pulsar radio emission.

To produce one- and two-dimensional histograms of single-pulse polarisation states (Ekers & Moffet, 1969; Manchester et al., 1975; Backer et al., 1976; Stinebring et al., 1984; McKinnon & Stinebring, 2000; McKinnon, 2002; Edwards & Stappers, 2004) it must be possible to detect individual pulses; however, most pulsars are not sufficiently bright and these techniques cannot be applied. This results in the reliance on a limited number of the brightest pulsars for studies, which may be subject to biases (van Straten & Tiburzi, 2017). To advance our understanding of the physics underlying single-pulse variability, novel statistical methods (e.g. Backer, 1970; Edwards 2004; van Straten & Tiburzi 2017; and Primak et al. 2022) are required to investigate and analyse phenomena that are observed only in rare cases among the pulsar population. The pulse-to-pulse variability of PSR B1919+21 is particularly noteworthy, exhibiting rare and unexpected characteristics such as an oblate spheroidal distribution of the Stokes polarisation vector in $\boldsymbol{p}$-space and drifting in only polarised flux (and not in total intensity). Despite being the first discovered pulsar and possibly one of the most studied, there is still much to learn about PSR B1919+21 as new phenomena continue to be uncovered more than 50 years after its discovery (Hewish et al., 1968).

1.6 Polarisation of Drifting sub-pulses

The polarisation longitude-resolved fluctuation spectrum (PLRFS) method was introduced by Edwards (2004) as an extension and generalisation of the LRFS to study the behaviour of polarisation states associated with highly periodic drifting sub-pulses in more

detail. The PLRFS is obtained by taking the one-dimensional discrete Fourier transform along short data sequences (along the pulse number axis) of a three-dimensional vector signal representing the Stokes polarisation vector at different pulse longitudes and pulse numbers. The PLRFS-based approach provides the most sensitive and direct means of analysing the elliptical paths that are traced by the Stokes polarisation vector on each drift cycle.

The PLRFS-based approach was used to study the behaviour of polarisation states in three highly-periodic pulsars (PSR B0320+39, PSR B0818−13, and PSR B0809+74) by Edwards (2004), who found that, at certain pulse longitudes, the Stokes polarisation vector periodically cycles as a function of pulse number around an elliptical path in $\boldsymbol{p}$-space in synchrony with the drifting sub-pulse modulation observed in the total intensity. Given the sufficiently coherent nature of the drift period (P_3) in the three pulsars studied, all information of the fluctuations is constrained to a single complex-valued harmonic of the PLRFS. In the case of quasi-periodic modulations, like those observed in PSR B1919+21, Edwards (2004) suggested that it is possible in principle to integrate the Hermitian spectral density tensor over a finite range of the fluctuation spectrum and obtain information on the fluctuation statistics of the data over the corresponding frequency range.

At each pulse longitude, the three-dimensional distribution of the Stokes polarisation vector can be described by performing an eigendecomposition of the 3×3 symmetric real-valued covariance matrix formed by summing over all fluctuation frequencies (Edwards, 2004), which is equivalent to the analysis of auto- and cross-correlations between the Stokes parameters computed in the time domain (Primak et al., 2022). A prolate spheroidal distribution, characterised by one significant eigenvalue ($\sigma_1 > \sigma_2 = \sigma_3$, where σ_i are the standard deviations of the eigenvalues, $i = 0, 1, 2, 3$, and typically $\sigma_0 > \sigma_1$), is commonly observed in radio pulsars, as expected for incoherent OPM superposition (van Straten & Tiburzi, 2017). An oblate spheroidal distribution, characterised by two

significant eigenvalues ($\sigma_1 \approx \sigma_2 > \sigma_3$), has been observed in only one pulsar (PSR B1919+21; Primak et al., 2022).

The longitude-resolved polarisation state of PSR B1919+21 was studied by Primak et al. (2022) using statistical techniques such as Principle Component Analysis of the Stokes parameters (van Straten & Tiburzi, 2017), analysis of the cross-correlations between the Stokes parameters (Prószyński & Wolszczan, 1986; Taylor et al., 1975), and P_3-folding (Taylor et al., 1971; Edwards, 2004). Through these techniques, Primak et al. (2022) discovered elliptical cycling of the polarisation state in PSR B1919+21, which was found to be synchronous with the periodicity of the drifting sub-pulses. This occurs in the region where Primak et al. (2022) first noticed a distribution of the Stokes polarisation vector in the shape of an uncommon oblate spheroid, which is inconsistent with incoherent OPM superposition (van Straten & Tiburzi, 2017). Further study of the oblate spheroidal distribution in longitude-resolved scatter plots (reproduced in Appendix C) led to the discovery of a toroidal distribution of polarisation states. They concluded that the torus is formed by the quasi-periodic cycling of the Stokes polarisation vector about an elliptical path in $\boldsymbol{p}$-space.

The P_3-folding technique used by Primak et al. (2022) is an effective way to study synchronous fluctuations between OPM switching and drifting sub-pulses. This is done by searching for periodic signals using the LRFS and PLRFS in single-pulse data and then computing drift phase and pulse-longitude resolved averages of the Stokes parameters (Taylor et al., 1971; Edwards, 2004; Ilie et al., 2020; Primak et al., 2022). The resulting two-dimensional data can be analysed in terms of total intensity and polarisation, as well as position angle and ellipticity angle, as shown in Figure 8 of Primak et al. (2022).

1.7 Research Aim

In this research, the novelty lies in building upon the work introduced by Edwards (2004) by extending the PLRFS-based analysis to study quasi-periodic drifting sub-pulses (with fluctuation power that spans a finite range of harmonics), which was previously only suggested in theory. We demonstrate the effectiveness of this technique by applying it to the first-discovered pulsar, PSR B1919+21. To reveal the drift synchronicity in this pulsar, we implement the LRFS and PLRFS analysis using the one-dimensional discrete Fourier transforms of the total intensity (Stokes I) and the components of the longitude-resolved Stokes polarisation vector (Stokes Q, Stokes U, and Stokes V). The correlations between these components manifest as an elliptical oscillation in $\boldsymbol{p}$-space with a period related to that of the drifting sub-pulse modulation. To further refine our analysis and model the elliptical paths of the Stokes polarisation vector in $\boldsymbol{p}$-space, we perform an eigendecomposition on the 3×3 Hermitian coherency matrix formed by summing over the fluctuation frequencies associated with quasi-periodic modulations.

The extension of the PLRFS-based approach improves upon the analysis of auto- and cross-correlations between the Stokes parameters (e.g. Primak et al. 2022) that characterise fluctuations in total intensity and polarised flux as a function of lag (time delay). This novel approach also independently verifies the elliptical cycling of polarisation state discovered by Primak et al. (2022), has greater experimental sensitivity to periodic modulations of polarisation state and enables more direct analysis and interpretation.

In the future, we plan to generalise and apply the extension of the PLRFS method to a wider range of radio pulsars in order to obtain a quantitative measure of the prevalence of quasi-periodic fluctuations in total intensity and polarised flux, and the synchronous fluctuations of polarisation state in pulsars with drifting sub-pulses. The exploratory nature of the work presented in this thesis also allows for the possibility of discovering pulsars that exhibit quasi-periodic fluctuations of polarisation state where there is no

evidence of drifting in total intensity. By producing statistical descriptions of quasi-periodic polarisation fluctuations in the signals from radio pulsars, we hope to facilitate physical interpretation of the drifting phenomenon, provide new constraints on existing theories, and ultimately enable a deeper understanding of the physics of relativistic plasmas in strong magnetic fields.

The methodology implemented in this work is outlined in Chapter 2, explicitly contrasting between the PLRFS-based approach introduced by Edwards (2004) and the extension of that work applied to a pulsar with known quasi-periodic behaviour, PSR B1919+21. Chapter 3 presents a summary of the findings and demonstrates the effectiveness of the PLRFS to analyse quasi-periodic modulations in total intensity and polarisation, and explores the anomalous behaviour in the different components of the pulse profile using a variety of techniques. We discuss plausible explanations for the origin of the observed phenomena in Chapter 4, and speculate physical interpretations of the periodicity and polarisation behaviour. Chapter 5 concludes the thesis and proposes future applications of the novel statistical methods presented in this work to a wider range of radio pulsars.

Chapter 2

Methodology

2.1 Dataset

The dataset analysed in this thesis consists of highly-sensitive single-pulse observations of PSR B1919+1 at a central frequency of 1414 MHz (bandwidth of 20Mhz), recorded at the Arecibo Observatory on November 21, 1992, as part of a larger dataset (Hankins & Rankin, 2010). The interval between pulse longitude bins in these data is ~ $1.206\mathrm{ms}$, and the signal is gated such that there are 105 pulse longitude bins centred on the peak of the pulsar. This gate spans ~ $127\mathrm{ms}$ which is approximately 9.5% of the spin period $P_1 \simeq 1.3374$ s. An additional 31 off-pulse longitude bins are also recorded; these contribute to characterising the system equivalent flux density as described in Section 2.2.1. Primak et al. (2022) discovered that PSR B1919+21 exhibits phase-resolved fluctuations that are anomalous compared to the 31 other observed pulsars, first noted as an oblate spheroidal distribution of the Stokes polarisation vector at each pulse longitude over a broad region of the pulse profile. This distribution is inconsistent with the expected prolate spheroidal distribution of incoherent OPM superposition (van Straten & Tiburzi, 2017). The observation of PSR B1919+21 was selected for this research to reproduce and extend the results of Primak et al. (2022) in more detail using

novel statistical methods. Additionally, we demonstrate an extension of the PLRFS-based approach (Edwards, 2004) on a pulsar known to exhibit quasi-periodic sub-pulse modulation in total intensity and polarisation. The analysis presented in this thesis is primarily performed using our self-developed Python software, and also requires PSRCHIVE, an open-source software library for pulsar astronomy (Hotan et al., 2004; van Straten et al., 2012). The Python software we have developed will be generalised and applied to the wider pulsar population, and will also be made publicly available as a component of the Pulsar Radio Emission Statistical Survey (PRESS) Project [1].

2.2 Noise Reduction

In our single-pulse data set, we model the total power detected by the radio telescope as

$$P_{tl} = g(t)S_{tl} + S_{\mathrm{sys}}(t) \tag{2.1}$$

where t is the pulse number, l is the pulse longitude, $g(t)$ is the product of antenna gain and amplification due to interstellar scintillation (discussed in Section 2.2.2), S_{tl} is the intensity of the pulsar, and $S_{\mathrm{sys}}(t)$ is the system equivalent flux density (SEFD). We are interested in analysing only the pulsar intrinsic signal, thus it is necessary to remove biases due to phenomena that are not intrinsic to the pulsar.

2.2.1 System Equivalent Flux Density

The SEFD is a measure of the noise in a system, including the receiver noise temperature, which is a measure of the amount of thermal noise generated by the receiver electronics and other components; atmospheric noise, which is caused by atmospheric gases,

[1] https://sites.google.com/view/psr-press

water vapor, and other sources, and can vary depending on the weather conditions; and sky noise, which is caused by galactic synchrotron emission; and radio frequency interference (RFI) from antenna gain and human-made sources such as mobile phones, TV, and radio broadcasts.

The SEFD,

$$S_{\rm sys}(t) = \frac{T_{\rm sys}}{G(t)} \tag{2.2}$$

where $T_{\rm sys}$ is the system temperature, typically dominated by thermal noise in the receiver, and $G(t)$ is the gain of the antenna which varies with time at Arecibo because, owing to projection, its effective area varies with the elevation of the source.

The SEFD can be determined by analysing the time varying baseline of the pulse profile. To do this, a classification algorithm, which is defined in Section 2.4, was developed and used to differentiate between on-pulse and off-pulse regions of pulse phase. The average total intensity of the off-pulse regions is then calculated for each pulse, and is subsequently subtracted from the pulse profile to remove the SEFD (see Figure 2.1). The SEFD appears to increase with time because these data have been calibrated to an absolute flux scale (Hankins & Rankin, 2010), and the gain of the antenna decreased with time in these observations as the source moved away from zenith.

2.2.2 Scintillation-Induced Variability

After we calibrated the direction-dependent gain of the antenna (Section 2.2.1), there remains slow variations in the apparent flux density of the pulsar owing to scintillation; these can be modelled as a variable gain (Armstrong et al., 1995). This wave interference pattern is caused by the scattering of radio waves as they pass through the ionised interstellar medium, similar to the way stars twinkle due to scattering in Earth's atmosphere. The scattering causes radio waves to travel along multiple paths, resulting

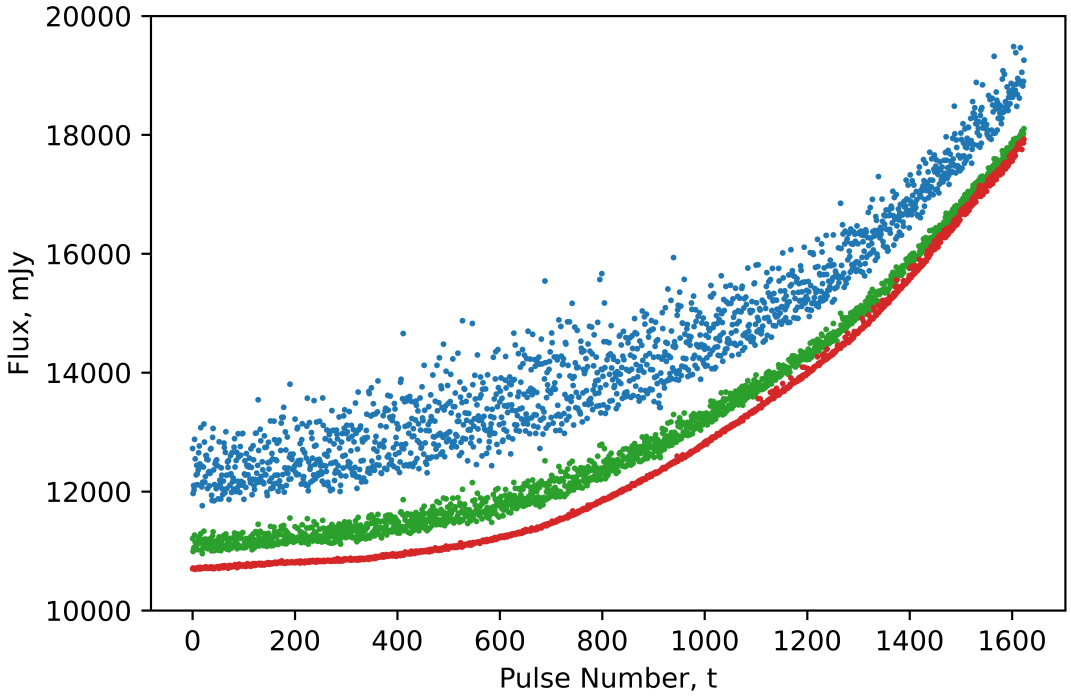

Figure 2.1: Average total intensity of the source data integrated over different regions of the pulse profile as a function of pulse number. The blue, green, and red dots represent the data integrated over the on-pulse window, full profile, and off-pulse regions, respectively. Note the gradual increase of the system equivalent flux density (SEFD) over the duration of the observation.

in fluctuations in the received signal's total intensity, which appear as additional variability on top of the intrinsic pulsar signal. The power spectral density of this pattern is typically red, meaning its power decreases with increasing frequency, in contrast to white noise which has a constant power spectral density across all frequencies. The amplitude of scintillation-induced red noise variations can be significant, therefore, it is necessary to compensate/correct for scintillation before the variability that is intrinsic to the pulsar can be studied.

The gain variation caused by scintillation affects only the pulsar signal. Therefore, the variable gain (Equation 2.3) is computed using the average total intensity integrated over the on-pulse window of each pulsar rotation. A rolling average is then taken over this average total intensity data from all pulses, and because the scintillation time of PSR B1919+21 at 1.4 GHz is approximately 500 to 1500 seconds (Cordes, 1986; Bhat

et al., 1999), we use a window size of 100 pulses. In principle, this method will also absorb any pulsar-intrinsic flux variations that occur on a similar timescale; however, the 128-pulse short Fourier transforms used in this study (Section 2.3) are only marginally longer than this timescale, therefore the subtracted flux would affect only primarily the DC bin.

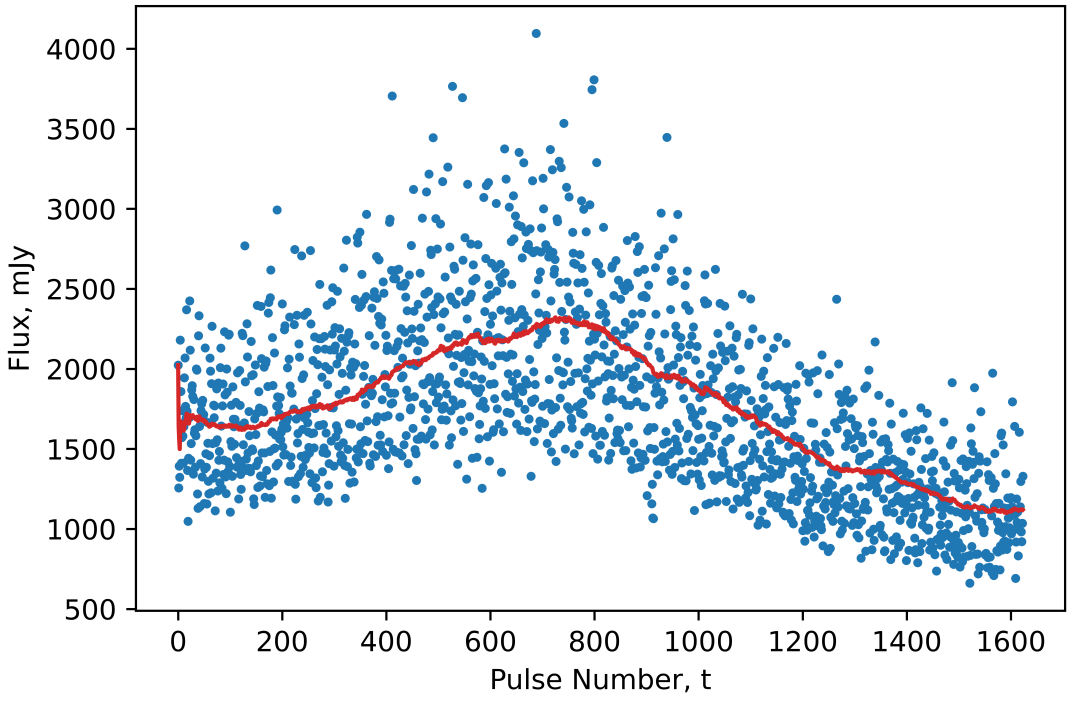

Figure 2.2: Moving average of the on-pulse total intensity (red solid line) computed over 100-pulse windows, where the single-pulse intensities (blue dots) are integrated over their own on-pulse window.

The gain can be seen as a steady rise and fall of the total intensity over the duration of the observation attributed to the low frequency modulations induced by scintillation through the ionised interstellar medium (Figure 2.2). Finally, the moving/rolling average is divided by the global average to determine the gain correction. To correct for the scintillation-induced variability, we divide Stokes parameters (total intensity and polarisation vector) observed at time t by the gain correction, $g(t)$. It is important to note that scintillation-induced variability scales all four Stokes parameters by the same factor; therefore, the rolling average need not be taken over the polarisation vector,

and we can divide the polarisation data by the rolling average determined for the total intensity. The use of the rolling average helps to smooth out any fluctuations and provide a more accurate representation of the gain. Given the estimated values of $S_{\text{sys}}(t)$ and $g(t)$, we compute the pulsar-intrinsic intensity

$$S_{tl} = \frac{P_{tl} - S_{\text{sys}}(t)}{g(t)} \tag{2.3}$$

where $g(t) = \frac{\langle I(t) \rangle}{\langle I \rangle}$, $\langle I(t) \rangle$ is the moving average of the total intensity as a function of time, and $\langle I \rangle$ is the global average of the total intensity over all pulse longitudes and time. The post-correction plot (Figure 2.3) of the total intensity demonstrates a significant reduction in biases resulting from low-frequency scintillation-induced variability.

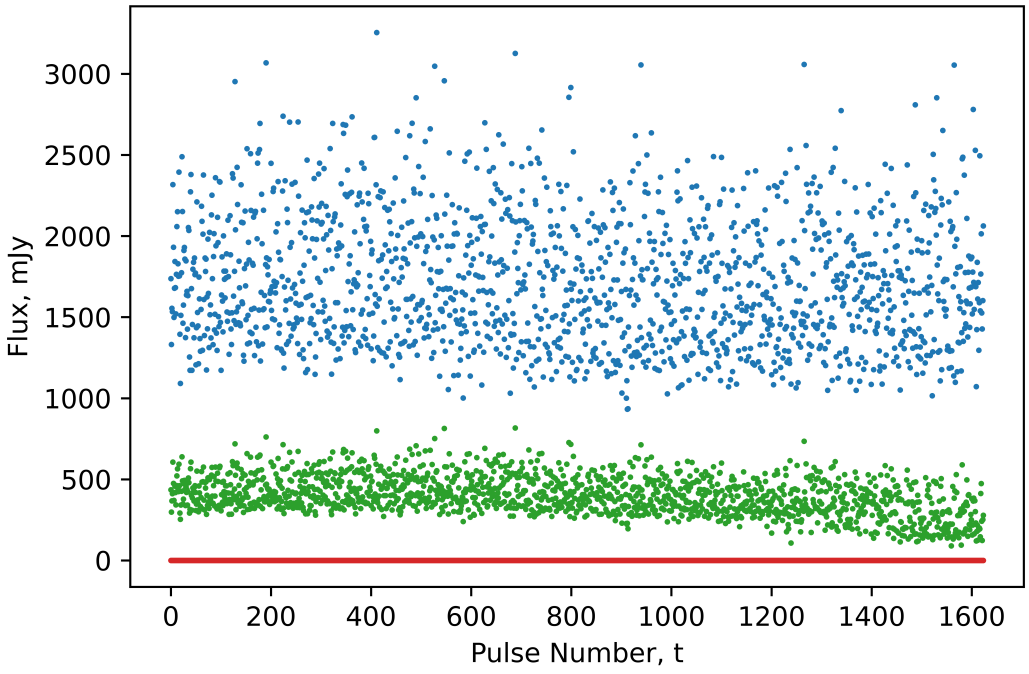

Figure 2.3: Average total intensity integrated over different regions of the pulse profile as a function of pulse number after removing biases owing to SEFD and gain. The blue, green, and red dots represent the data integrated over the on-pulse window, full profile, and off-pulse regions, respectively.

2.3 Discrete Fourier Transform

This research builds on the PLRFS-based analysis introduced by Edwards (2004) for studying the behaviour of polarisation states associated with highly-periodic drifting sub-pulses (with phase-coherent fluctuation power constrained to a single bin in the fluctuation power spectrum, or harmonic). Edwards (2004) suggested that in principle the PLRFS-based approach could also be applied to study quasi-periodic drifting sub-pulses (with fluctuation power that spans a finite range of harmonics), such as those observed in PSR B1919+21 (Primak et al., 2022); however, the pulsars studied by Edwards (2004) (e.g., PSR B0320+39, PSR B0818−13, and PSR B0809+74) had sufficiently stable drift-period modulations, and the extension of the PLRFS-based analysis to quasi-periodic pulsars was not demonstrated. The recent discovery of quasi-periodic drift-synchronous polarisation fluctuations in PSR B1919+21 (Primak et al., 2022) provides an opportunity to test the extension of the PLRFS-based analysis proposed by Edwards (2004) on a pulsar known to exhibit such fluctuations, which forms the original motivation for this thesis.

The PLRFS is a multivariate analysis of the covariances between the harmonics of discrete Fourier transforms of the elements of the Stokes polarisation vector used to analyse the association between the polarisation states of sub-pulses and their tendency to periodically drift across the pulse window. Maintaining the nomenclature of Edwards (2004), the general analysis begins by considering the total intensity, I_{tl}, and the sample mean Stokes polarisation vector, $\boldsymbol{p}_{tl} = (QUV)^{\intercal}$, as a function of pulse number t and pulse longitude l. The analyses of the four sample mean Stokes parameters is performed separately for I_{tl} and $\boldsymbol{p}_{tl}$.

The LRFS and PLRFS are obtained for I_{tl} and $\boldsymbol{p}_{tl}$, respectively, by taking the one-dimensional discrete Fourier transforms of each Stokes parameter at each pulse longitude as a function of time. This involves dividing the data into T contiguous

sequences of N pulses and, for each pulse longitude, taking four separate Fourier transforms; one on each Stokes parameter:

$$L_{Tkl} = \frac{1}{N} \sum_{t \to 1+(TN)}^{N(T+1)} e^{-2\pi itk/N} \left(I_{tl} - \langle I_l \rangle \right) \tag{2.4}$$

$$\boldsymbol{P}_{Tkl} = \frac{1}{N} \sum_{t \to 1+(TN)}^{N(T+1)} e^{-2\pi itk/N} \left(\boldsymbol{p}_{tl} - \langle \boldsymbol{p}_l \rangle \right) \tag{2.5}$$

where i is the imaginary unit, N is the number of pulses in each sequence, T is the sequence index starting at zero, and the angle brackets denote an average over pulse number, computed for each sequence of pulses. We define $K = [0, N)$ as the domain of harmonic bins in a fluctuation spectrum. The DC bin ($k = 0$) of the LRFS and PLRFS in a given pulse sequence and pulse longitude is forced to zero by the subtraction of the averages $\langle I_l \rangle$ and $\langle \boldsymbol{p}_l \rangle$ of each sequence. We denote $K_+ = [0, N/2)$ as the range of all harmonic bins in the spectrum of the analytical signal, where the harmonic bins in $k \in [N/2, N)$ are omitted as they are simply the complex-conjugates of the harmonic bins in $k \in [0, N/2)$ and contain no additional information (i.e., $\boldsymbol{P}_{kl} = \boldsymbol{P}^*_{(-k)l}$; Edwards 2004).

In this work, $N = 128$ pulses, and therefore adjacent harmonics of the FFT are separated by:

$$\Delta\nu_3 = \frac{1}{N \cdot P_1} = 0.005841567 \text{ Hz}, \tag{2.6}$$

where P_1 is the fundamental spin frequency of the pulsar. Throughout this work, normalised drift frequencies $f_3 = \nu_3 \cdot P_1$ are used.

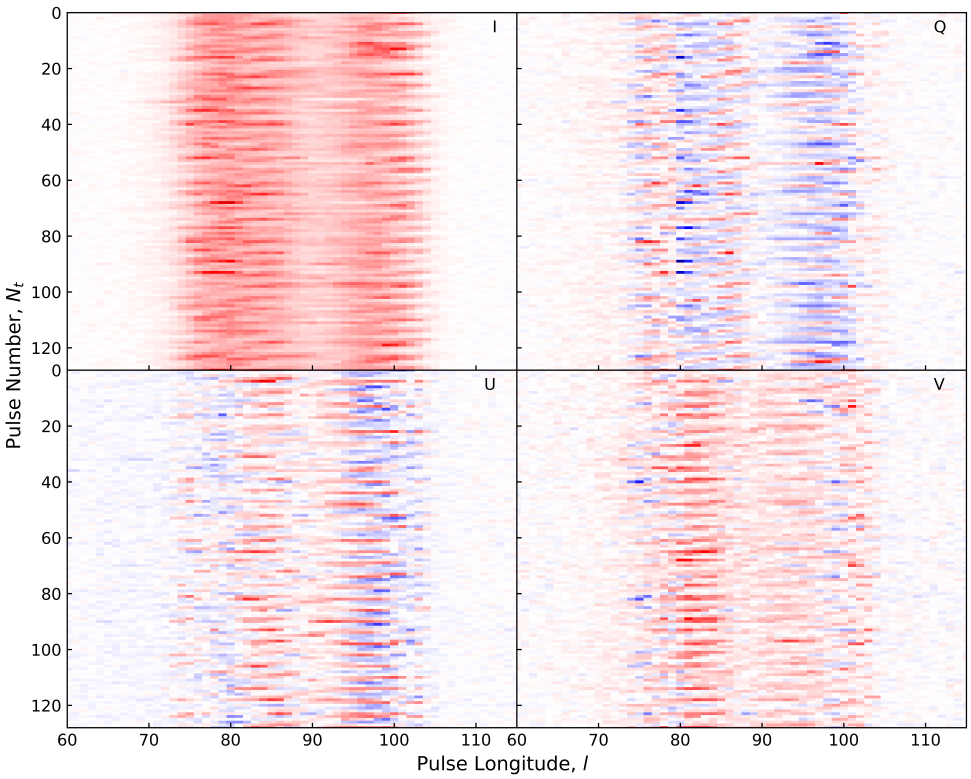

Figure 2.4: Pulse-stack in total intensity and polarisation of 128 consecutive pulses of PSR B1919+21, where the blue values are negative, and red values are positive.

2.4 Subset Classification

The extension of the PLRFS-based approach is formed on the basis that analysing any subset of K_+ of the PLRFS yields insights into the fluctuation statistics of the data within the corresponding frequency range (Edwards, 2004). Three distinct subsets of harmonic bins are identified for our analysis of quasi-periodic modulations of the drift-frequency: the on-signal range, $K_{\rm on}(l,T) \subset K_+$, in which the quasi-periodic signal is confined; the off-signal range, $K_{\rm off}(l,T) \subset K_+$, which characterises the white self-noise of the pulsar and the SEFD; and the full fluctuation spectrum (K), which contains all fluctuation frequencies (including the complex-conjugates of the analytic signal). Typically $|K_+| > |K_{\rm off}(l,T)| > |K_{\rm on}(l,T)|$, where $|A|$ is the cardinality of set

A. We determine on-signal ranges only for fluctuation spectra corresponding to pulse longitude bins that belong to the on-pulse window, which is determined as described in Section 2.4.1. Therefore, for off-pulse longitudes, the off-signal range is set equal to the full spectrum.

To determine the frequency ranges of interest, a threshold of three times the Median Absolute Deviation from the Median (MADM) is used. The MADM is a measure of statistical dispersion that robustly quantifies the spread of a dataset around its median and serves as a proxy for the standard deviation of the noise in a given fluctuation spectrum. Compared to the standard deviation, the MADM is less sensitive to outliers. The MADM is computed by first finding the median of the PLRFS and then calculating the absolute deviation of each data point from the median. The threshold for the analysis of all selected subsets is then set at three times the MADM above the median, denoted as $3 \times \mathrm{MADM}$.

The power spectral density has an exponential distribution, and for an exponential distribution, $\mathrm{MADM} = \ln(2)\sigma$, where σ is the standard deviation. Therefore, a threshold of $3 \times \mathrm{MADM}$ is approximately equivalent to a 2σ threshold, which for an exponential distribution corresponds to false detection rate of 13.5%. Although this leads to an increase in false detections, we further constrain the selection by choosing only contiguous ranges of significant power.

2.4.1 On-Pulse Window

The on-pulse window, denoted as $\Phi_{\mathrm{on}}(T)$, is determined so that we may focus our analysis on the pulse longitude bins associated with the pulse profile, and differentiate the pulsar signal from the noise of the off-pulse regions where the radio emission beam is outside the line of sight (Figure 2.5). The on-pulse window is defined as the range of contiguous pulse longitude bins that exceed the set threshold ($3 \times \mathrm{MADM}$) and contains

the greatest total intensity. This is repeated for every pulsar rotation, so that each may have its own determined on-pulse window. In single pulses that consist of multiple discrete sub-pulses, this technique will select only the brightest sub-pulse. This is not an issue for the remainder of our analysis for the following two reasons. First, because we lose the ability to resolve individual pulsar rotations in the frequency domain, an overall on-pulse window is determined for each sequence of pulses. The on-pulse window for each sequence is then the contiguous range of pulse longitude bins confined within the minimum lower boundary and maximum upper boundary of all on-pulse windows in the given pulse sequence. Second, although this technique may underestimate single-pulse flux densities (Figure 2.2), we smooth over 100 pulses to estimate the average gain variations.

2.4.2 Off-Pulse Regions

Off-pulse regions, denoted as $\Phi_{\text{off}}(T)$, contain all of the pulse longitude bins that are not within ±3 pulse longitude bins of the on-pulse window ($\Phi_{\text{off}} = \{l | \max(\Phi_{\text{on}}) + 3 < l \text{ or } \min(\Phi_{\text{on}}) - 3 > l\}$) and have a total intensity below the set threshold ($3 \times \text{MADM}$). The noise and fluctuation spectra measured in the off-pulse regions characterises the SEFD which allows us to correct for biases and obtain the pulsar-intrinsic signal. As outlined in Section 2.2, we remove biases due to SEFD by subtracting the baseline average of the off-pulse regions from the total intensity of all pulse longitude bins.

2.4.3 On-Signal Range

The on-signal range is determined for fluctuation spectra computed in pulse longitude bins that belong to the on-pulse window of a given sequence of pulses (i.e. $\boldsymbol{P}_{Tkl}$, where $k \in K_{\text{on}}$ and $l \in \Phi_{\text{on}}$). Analogous to the on-pulse window, it is defined as the range of contiguous harmonic bins that exceed the set threshold ($3 \times \text{MADM}$) and contains

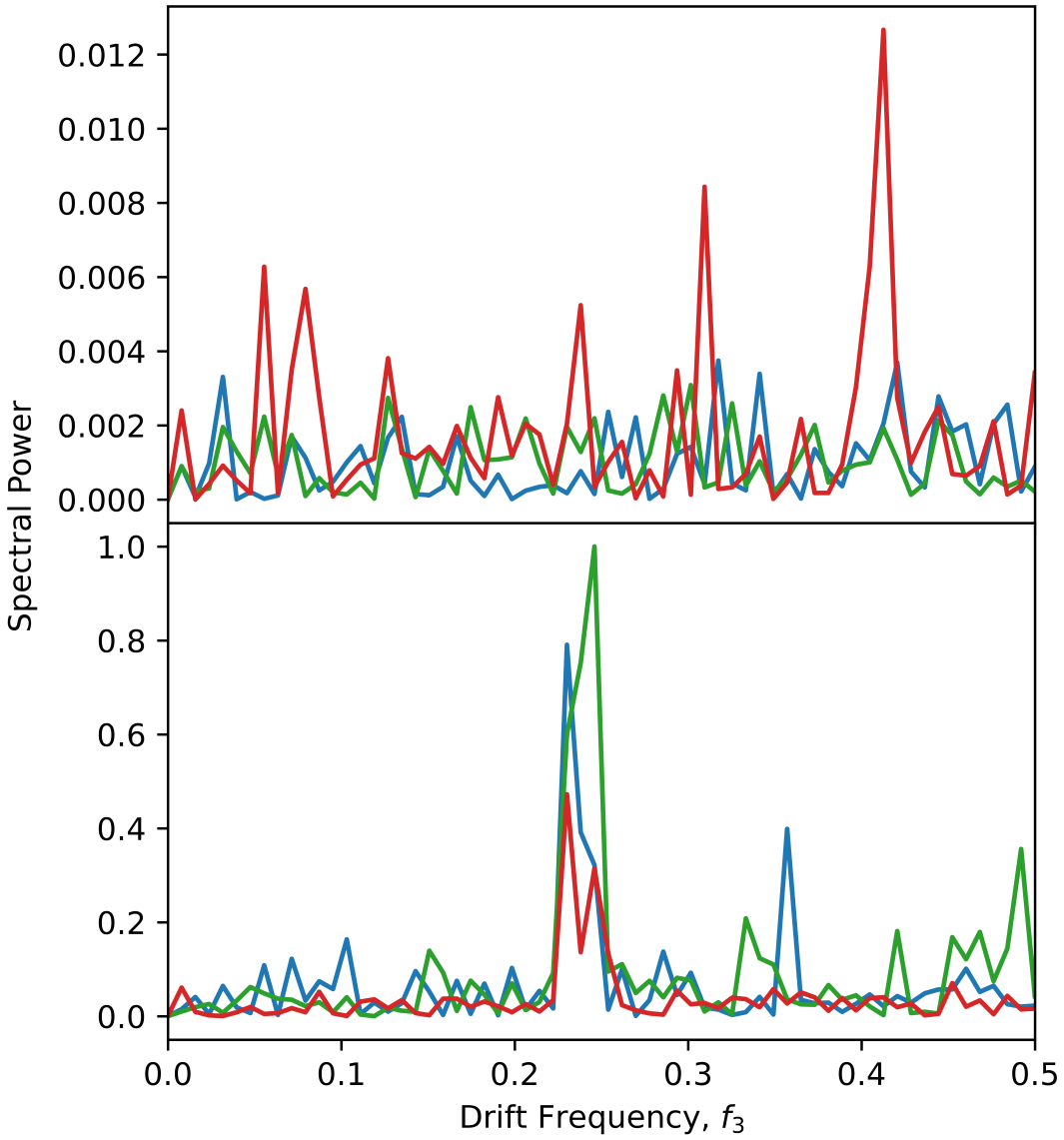

Figure 2.5: PLRFS computed over the first sequence of pulses at two different pulse longitude bins. *Upper panel*: Computed at the 40th pulse longitude bin belonging to the off-pulse region, $\boldsymbol{P}_{Tkl}$ where $l \in \Phi_{\rm off}(\kappa)$. *Lower panel*: Computed at the 99th pulse longitude bin belonging to the on-pulse window, $\boldsymbol{P}_{Tkl}$ where $l \in \Phi_{\rm on}(\kappa)$. The green, blue, and red solid lines are the elements of the PLRFS, and represent the fluctuation spectra of Stokes Q, U, and V, respectively.

the greatest spectral power. It is important to note that, for a given sequence T and pulse longitude bin l, a different on-signal range is detected in the fluctuation spectra of each of the four Stokes parameters. Thus, we define the on-signal range of each PLRFS to be the range that encompasses all detected ranges, from the minimum lower boundary to the maximum upper boundary of all Stokes parameters. For example, in the fluctuation spectrum of the first sequence at pulse longitude $l = 96$ the on-signal ranges of Stokes Q, U, and V span $[28, 29, 30]$, $[28, 29]$, and $[27, 28, 29]$, respectively. Therefore, the on-signal $K_{\rm on}$ is the union of the three sets: $[27, 28, 29, 30]$. Because the span of the fundamental response for a given Stokes parameter may be narrower than the length of the overall on-signal subset, $K_{\rm on}$, we accept the inevitable integration of white self-noise, which has equal intensity over the full spectrum (K) and will reduce the signal-to-noise ratio and sensitivity of the analysis.

2.4.4 Off-Signal Ranges

The off-signal ranges need not be determined for off-pulse longitudes of a given pulse sequence since they are set equal to the full spectrum by default. For on-pulse longitudes, the off-signal ranges are defined as all harmonic bins (need not be contiguous) with spectral power below the set threshold ($3 \times \mathrm{MADM}$), and not within ± 5 harmonic bins of the on-signal range of the corresponding sequence. The latter criteria is necessary to avoid biases due to residual on-signal spectral power that did not exceed the set threshold ($3 \times \mathrm{MADM}$), but is still significant enough to introduce biases. Harmonics above 80% of the Nyquist frequency are excluded from the off-signal ranges to avoid integration of spectral power at double the quasi-periodic modulation frequency ($2 \times k$, where $k \in K_{\rm on}$) that arises due to overlapping drift bands that are 180° out of phase (as seen in Figure 8 of Primak et al. 2022 at pulse longitude $\phi \simeq -5.4°$). The off-signal ranges then characterise the white self-noise of the pulsar and the SEFD, which can be

used to correct for biases in the quasi-periodic signal contained in the on-signal range.

2.5 PLRFS-Based Approach

The novel methodology that was developed for this research project follows the approach suggested by Edwards (2004) for analysing pulsars that exhibit a quasi-periodic drifting modulation pattern. Section 2.5.1 describes the analysis demonstrated by Edwards (2004) for pulsars whose drifting is highly-periodic to elucidate the simplest approach. Then, the novel extension to the PLRFS-based approach is described in Section 2.5.2, which is specifically designed to adapt to and interpret quasi-periodic behaviour in pulsars like PSR B1919+21. Both sections are described in general terms to provide a statistical framework for future studies of the wider pulsar population.

2.5.1 Highly-Periodic Drifting

The segmentation of data over pulse number was important for optimising the sensitivity in the analysis of Edwards (2004), as the fundamental response of the imperfect periodicity of drifting sub-pulses is not typically confined to a single harmonic bin in the fluctuation spectrum. In order to address this issue, contiguous sequences of short 128-pulse lengths were used, over which the fundamental response was typically confined to a single coefficient for sufficiently coherent signals. As a result, all information about drift frequencies was concentrated in a single harmonic bin of each fluctuation spectrum. By phase-coherently integrating (Edwards et al., 2003) the corresponding harmonic bins from each PLRFS over all time, longitude-dependent complex polarisation envelopes were formed. Each of the three components of the Stokes polarisation vector ($\boldsymbol{p}$) have differing phase and amplitudes, and the elements of the complex polarisation envelopes

define the parameters of elliptical paths about which $\boldsymbol{p}$ cycles in $\boldsymbol{p}$-space.

$$\boldsymbol{P} = (\boldsymbol{A} + i\boldsymbol{B})e^{i\phi} \tag{2.7}$$

where $\boldsymbol{A}$ and $\boldsymbol{B}$ are real vectors that point in the direction of the semi-major ($|\boldsymbol{A}|$) and semi-minor ($|\boldsymbol{B}|$) axes of the elliptical paths and define the amplitude of sub-pulse modulations in polarisation (see top panel of Figure 4 and Equation 3 in Edwards, 2004). $\boldsymbol{A}$ and $\boldsymbol{B}$ are perpendicular when $\boldsymbol{P} \cdot \boldsymbol{P}$ is real-valued, which is achieved by appropriately choosing the overall vector phase ϕ (Appendix B). Further polarisation fluctuation statistics of the data, including covariance terms, can be derived from the polarisation fluctuation cross spectrum (PFCS) which is obtained by taking the outer product of the PLRFS (Equation 9; Edwards, 2004):

$$\boldsymbol{S}_{kl} = \boldsymbol{P}_{kl}\boldsymbol{P}_{kl}^{\dagger} \tag{2.8}$$

where † denotes the Hermitian transpose, which is the transpose, then complex conjugate, of a matrix or vector. There is no absolute phase information in $\boldsymbol{S}_{kl}$ since the term containing it, $e^{i\phi}$, is cancelled out by multiplication with its complex conjugate in Equation 2.8. Thus, the PFCS can be summed over multiple pulse sequences without the need to compensate for an arbitrary phase-offset. In the analysis of Edwards (2004), the PFCS is integrated over all pulse sequences and over the set of all harmonic bins, K, the result of which is a one-dimensional (longitude-resolved) array of 3×3 real-valued covariance matrices between the elements of $\boldsymbol{p}$, equivalent to that computed in Primak et al. (2022) in the time domain (refer to Section 3.2.1 for a definition and verification of Parseval's Theorem).

Where Edwards (2004) refers to the spectral density tensor derived from Equation 2.8 (see also Samson, 1973; Carozzi et al., 2000; Dennis 2004), we refer to it as

the "polarisation fluctuation cross spectrum" (PFCS) for the following reasons: the "cross spectrum" is a simplified version of the cross power spectral density; inclusion of "fluctuation" is in reference to the term introduced by Backer (1973), which allows it to become clear that our purpose is to define the power spectral density of fluctuations in flux density (at frequencies around Hz to kHz, related to the rotational frequency of the pulsar); finally, "polarisation" elucidates that we are studying the cross spectral densities of fluctuations in the Stokes parameters.

Eigendecomposition of the real-valued covariance matrix provides information on the magnitude and orientation of the fluctuations of the three-dimensional elements of the Stokes polarisation vector formed in $\boldsymbol{p}$-space (McKinnon, 2004; Edwards & Stappers, 2004). Modelled as an ellipsoidal cloud, the eigenvectors form its axes, and the eigenvalues (σ_i, where $i = 0, 1, 2, 3$) define its shape: one single significant eigenvalue ($\sigma_1 > \sigma_2 = \sigma_3$) suggests a prolate spheroidal distribution; and two significant eigenvalues ($\sigma_1 \approx \sigma_2 > \sigma_3$) suggest an oblate spheroidal distribution. The elliptical path described by Equation 2.7 is confined within the shape of the cloud in $\boldsymbol{p}$-space.

2.5.2 Quasi-Periodic Drifting

For pulsars that are not sufficiently coherent or exhibit quasi-periodic behaviour, such as PSR B1919+21 (Primak et al., 2022), the fundamental response of the unstable drift-frequency (P_3) is washed out over multiple harmonic bins of the fluctuation spectrum computed over all pulses (Figure 2.6). Since it is necessary for the drift period to remain stable over a sufficiently long period of time to be confined within a single harmonic bin of the fluctuation spectrum, phase-integration of multiple FFTs over all time is not possible. The complex polarisation envelope studied by Edwards (2004) can therefore be obtained only for highly-coherent pulsars (Section 2.5.1). Therefore, to determine the parameters of the elliptical paths that $\boldsymbol{p}$ cycles about in $\boldsymbol{p}$-space, an

alternative complex vector $\boldsymbol{P}$ must be considered. To arrive at an appropriate $\boldsymbol{P}$ that describes the fluctuations that correspond to quasi-periodic drift-frequencies, we must analyse the finite range of harmonic bins in each fluctuation spectrum that confines the signal of interest (e.g., the on-signal range, $K_{\rm on}$; Section 2.4.3).

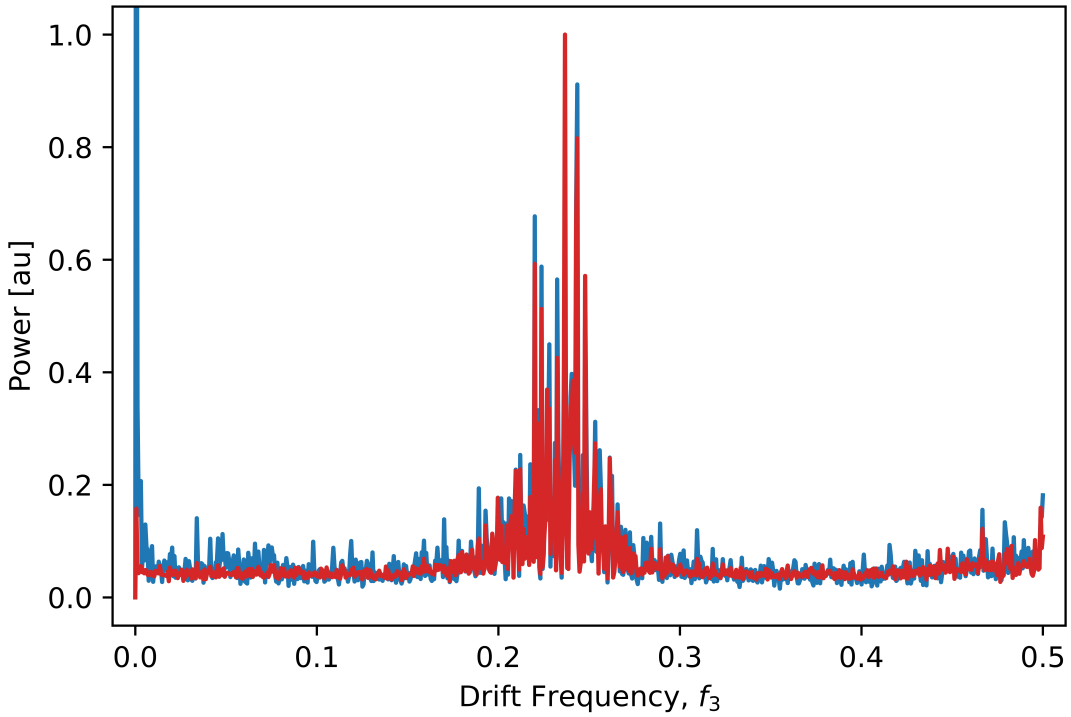

Figure 2.6: Fluctuation spectrum computed over all pulses (all time) and integrated over all pulse longitudes. The blue and red solid lines show the total and polarised ($Q^2 + U^2 + V^2$) fluctuation power spectral density, respectively. The fluctuation power spectral density in the first harmonic is approximately 2.2 times the peak of the quasi-periodic on-signal. The broad range of harmonic bins over which the drift period oscillates is attributed to the quasi-periodic nature of PSR B1919+21.

While segmentation of the data into sequences of pulses does not strictly confine quasi-periodic or incoherent signals to a single harmonic bin, it is effective in narrowing the range of harmonic bins over which quasi-periodic modulations occur in each PLRFS. This is because the peak of the fundamental response may oscillate between different pulse sequences, resulting in a variable distribution of the quasi-periodic signal across harmonic bins. Independent analysis of each sequence enables isolation of the specific range of harmonic bins that contains the signal of interest in each PLRFS, thereby

increasing the sensitivity of the analysis (see Section 2.4.3). Additionally, segmentation allows us to analyse variations in the modulations of the quasi-periodic drift period as a function of time, whereas a single FFT over the duration of the observation yields only a single fluctuation spectrum that includes all periodic and non-periodic information. Further investigation (Section 3.1.4) of the time-varying P_3 led to the unexpected discovery of the quasi-periodic drifting of the drift period.

The on-signal range derived from the fluctuation spectrum computed over all pulses (Figure 2.6) is so broad that it inevitably contains a high level of white self-noise of the pulsar. The detection of the on-signal range (Section 2.4.3) becomes more accurate over fluctuation spectra in which the drift period (P_3) is confined to a narrower bandwidth, and avoiding integration of harmonic bins that do not have the quasi-periodic signal of interest increases the signal-to-noise ratio. Thus, through segmentation of the data, the integration of white self-noise is minimised and we are able to characterise its behaviour more accurately (the more accurate $K_{\rm on}$ is, the more accurate $K_{\rm off}$ will be).

Sequences of pulses need not be contiguous (with an FFT step equivalent to the length of each sequence) as in the analysis of Edwards (2004). Rather, the one-dimensional discrete Fourier transforms can be computed over pulse sequences that overlap by some arbitrary amount. The pulse sequences analysed in this research were overlapped by 50% and 75%, with an FFT step of 64 and 32 pulses, respectively. This increased the number of sequences that were analysed without having to decrease the length of the sequence from 128 pulses. The total number of pulse sequences is then:

$$N_T = \frac{N_t - N}{N_{\rm step}}, \tag{2.9}$$

where N_t is the total number of pulses in the dataset, N is the FFT length and $N_{\rm step}$ is the step between FFTs (i.e., if $N_{\rm step} = N$, the pulse sequences will be contiguous. If $N_{\rm step} = \frac{N}{2}$, the pulse sequences will overlap by 50%, and so on). Note that N_T is

truncated to the lowest integer.

As suggested by Edwards (2004) in principle, one can sum the PFCS over any subset of K_+ to obtain the fluctuation statistics of the data over the corresponding frequencies. Equation 2.10 is an adaption of Equation 9 from Edwards (2004), and forms the polarisation fluctuation coherency matrix (PFCM), $\mathbf{C}$, as a function of any number of given subsets, κ, after integrating the resultant of the outer product over all harmonic bins in the subset κ and all sequences of pulses, N_T, along a constant pulse longitude:

$$\mathbf{C}_l(\kappa) = \frac{\sum_{T=0}^{N_T} \sum_{k \in \kappa_T} \boldsymbol{P}_{Tkl} \boldsymbol{P}_{Tkl}^{\dagger}}{\sum_{T=0}^{N_T} |\kappa_T|} \tag{2.10}$$

where $|\kappa_T|$ is the number of harmonic bins in the subset being analysed, and $\kappa \in (K_{\rm on}(l,T), K_{\rm off}(l,T), K)$ is one of the three different subsets of interest in this research (Section 2.4). As in Equation 2.8, all phase information is lost in the outer product operation, hence we are able to sum the PFCS (outer product resultant) over multiple sequences of pulses. $\kappa = K$ (the full spectrum) is the special case where the result computed over the full fluctuation spectrum is a real-valued covariance matrix of the data, and any $\mathbf{C}_l(\kappa)$ computed over a finite range of harmonic bins (i.e., $\kappa = K_{\rm on}(l,T)$ or $\kappa = K_{\rm off}(l,T)$) yields a one-dimensional (longitude-resolved) array of 3×3 Hermitian coherency matrices, referred to as the PFCM. In practice, the sum over $K_{\rm off}$ computed in Equation 2.10 is subtracted from the sum over $K_{\rm on}$.

The polarisation fluctuation coherency matrices $\mathbf{C}_l(K_{\rm off})$ and $\mathbf{C}_l(K_{\rm on})$ (Equation 2.10) are fourth moment covariances that cannot be linearly combined in the same way as the second order moments of statistically independent signals. A correction factor must be considered, as described by Equation 42 of van Straten and Tiburzi (2017):

$$\bar{C}_S = \bar{C}_A + \bar{C}_B + n^{-1} A \tilde{\odot} B \tag{2.11}$$

where $\bar{C}_A$ and $\bar{C}_B$ can correspond to the PFCM of the on-signal and off-signal subsets

of K. The correction factor $n^{-1}A\tilde{\odot}B$ decreases with integration length, i.e., when n is large, the correction becomes small and can be ignored. In the observation of PSR B1919+21, the sample rate is $20\mathrm{MHz}$ (20×10^6 samples of the Stokes parameters per second) and each pulse longitude bin spans approximately $1.206\mathrm{ms}$. This means that the sample mean Stokes parameters are integrated over $n \approx 24 \times 10^3$ samples per pulse longitude bin, which is very large. Therefore, $n^{-1}A\tilde{\odot}B$ is negligible and we can treat the fourth moment coherency matrices $\mathbf{C}_l(K_{\mathrm{off}})$ and $\mathbf{C}_l(K_{\mathrm{on}})$ as second moment variances.

Owing to the design of the subset classification algorithm in Section 2.4, all pulse longitude bins that belong to an on-pulse window have a PFCM derived from both the on-signal and off-signal ranges (i.e., $\mathbf{C}_l(\kappa)$, if $l \in \Phi_{\mathrm{on}}$, then $\kappa = K_{\mathrm{on}}$ or $\kappa = K_{\mathrm{off}}$) in order to characterise the quasi-periodic and white-noise components of the pulsar-intrinsic signal. Similarly, all pulse longitude bins that belong to off-pulse regions have a PFCM computed over the full fluctuation spectrum (i.e., $\mathbf{C}_l(\kappa)$, if $l \in \Phi_{\mathrm{off}}$, then $\kappa = K$) in order to characterise and analyse the white noise contribution of the SEFD, or "measurement noise". The presence of white self-noise in the quasi-periodic drifting signal is mostly corrected for by subtracting the average PFCM derived from the off-signal ranges from the PFCM determined for K_{on}, i.e., $\mathbf{C}_l(K_{\mathrm{on}})' = \mathbf{C}_l(K_{\mathrm{on}}) - \langle \mathbf{C}_l(K_{\mathrm{off}}) \rangle$.

The coherency matrices from each of the different subsets ($\mathbf{C}_l(K_{\mathrm{on}})$, $\mathbf{C}_l(K_{\mathrm{off}})$, and $\mathbf{C}_l(K)$) are subject to eigendecomposition in order to model the three-dimensional distribution of $\boldsymbol{p}$ in $\boldsymbol{p}$-space and the shape of the elliptical paths that are traced by $\boldsymbol{p}$ on each drift cycle. Unlike the eigenvalues derived from the analysis of the full fluctuation spectrum (e.g., Edwards, 2004; Primak et al., 2022) (Section 2.5.1), which describe the three-dimensional distribution of the ellipsoidal cloud in $\boldsymbol{p}$-space, the longitude-resolved complex-valued eigenvectors derived from a subset of harmonic bins characterise elliptical paths in $\boldsymbol{p}$-space around which the Stokes polarisation vector cycles quasi-periodically. One significant eigenvalue at a given pulse longitude bin denotes a single quasi-periodic process present in the corresponding fluctuation spectrum, and the

associated eigenvector describes an elliptical path about which $\boldsymbol{p}$ cycles as a function of time.

Analogous to the complex polarisation envelope defined in Section 2.5.1, every eigenvector is a complex-valued vector $\boldsymbol{P}$ (Equation 2.7) that provides information on the orientation and ellipsoidal shape of quasi-periodic sub-pulse modulations in polarisation. The lengths of its real ($\boldsymbol{A}$) and imaginary ($\boldsymbol{B}$) parts define the ellipse's semi-major and semi-minor axes (Equation 3; Edwards, 2004). The normal to the ellipse is obtained by computing a cross-product between the vectors $\boldsymbol{A}$ and $\boldsymbol{B}$ $(\boldsymbol{c} = \boldsymbol{A} \times \boldsymbol{B})$ of the primary eigenvector, which under certain assumptions provides information about the level of total linear polarisation ($L = |\sqrt{\boldsymbol{c}_1^2 + \boldsymbol{c}_2^2}|$) and circular polarisation ($|\boldsymbol{c}_3|$) of the natural modes.

Chapter 3

Results and Analysis

3.1 Spectral Analysis

3.1.1 Stokes Longitude-Resolved Fluctuation Spectra

As in Backer (1973) and Edwards (2004) we first studied the periodic behaviour of the drifting sub-pulses and Stokes polarisation vector by computing the one-dimensional discrete Fourier transform along vectors of constant pulse longitude segmented into sequences of 128 pulses (Equations 2.4 and 2.5). Consider the term Stokes longitude-resolved fluctuation spectrum, or SLRFS, to denote the longitude-resolved fluctuation spectra in both total intensity (LRFS) and polarisation (PLRFS). Then, the SLRFS shown in Figure 3.2 is integrated over all sequences of pulses and describes the average fluctuations at a given pulse longitude:

$$S_{kl\mu} = \sum_{T=0}^{N_T} \boldsymbol{P}_{Tkl\mu} \boldsymbol{P}_{Tkl\mu}{}^{*} \tag{3.1}$$

where $\mu = 0, 1, 2, 3$ for each of the Stokes parameters (I, Q, U, and V). The relative drift frequency, $f_3 = P_1/P_3$, along the y-axis is related to the fundamental spin-period of the

pulsar, P_1:

$$f_3 = \frac{k}{N} \tag{3.2}$$

where k denotes harmonic bin number and N is the number of pulses in a sequence, which is also equal to the Fourier transform length. In the upper panel of Figure 3.2, the SLRFS is normalised by the maximum value (over all pulse longitudes and harmonic bins of the Stokes Q, U, and V) of the LRFS such that all spectral power is on a scale between 0 and 1. In the lower panel, only the PLRFS is normalised by the maximum value (over all pulse longitudes and harmonic bins) of the PLRFS to discern the periodic and non-periodic fluctuations that are otherwise more difficult to distinguish in the upper panel.

The quasi-periodic nature of the drifting sub-pulses and oscillation of the Stokes polarisation vector is indicated by the presence of bands of spectral power that span a finite range of frequencies in both the LRFS and PLRFS. Three dominant drift bands appear centred at pulse longitudes: l = 76, l = 83.5, and l = 101 in total intensity; l = 76, l = 81, l = 86, and l = 97 in Stokes Q; l = 84 and l = 97 in Stokes U; and l = 82 in Stokes V, with a minor band at l = 99. All of the spectral bands observed in the SLRFS share a fundamental response at $f_3 \approx 0.24 f_1$, which reflects the synchronous relationship between the drifting sub-pulse modulation period and quasi-periodic cycling of the Stokes polarisation vector in $\boldsymbol{p}$-space (Primak et al., 2022).

Over the region of pulse longitude $85 \lesssim l \lesssim 98$, which approximately overlaps the saddle region between the leading and trailing components of the pulse profile, we observe evidence of strong periodicity in the linear components of the PLRFS (Stokes Q and U) where there is little to none in total intensity (Backer, 1973; Primak et al., 2022). This occurs in the region where Primak et al. (2022) reported quasi-periodic cycling of the Stokes polarisation vector about an elliptical path in $\boldsymbol{p}$-space.

The SLRFS also highlights bands of stochastic white noise (or white self-noise of

the pulsar in the LRFS) in regions of pulse longitude that correspond to the leading and trailing components of the average pulse profile ($74 \lesssim l \lesssim 85$ and $96 \lesssim l \lesssim 103$, respectively). The noise is more apparent at pulse longitude $l = 80$ in the top row of the lower panel, which is also where a transition between OPMs takes place (Figure 3.1) (e.g. Primak et al. 2022). Enhanced intensity modulation in regions of pulse longitude where there is a transition between OPMs has been observed in previous studies (McKinnon, 2004); however, it remains to be tested if the statistical origin proposed by van Straten (2009) is sufficient to explain the observed modulation.

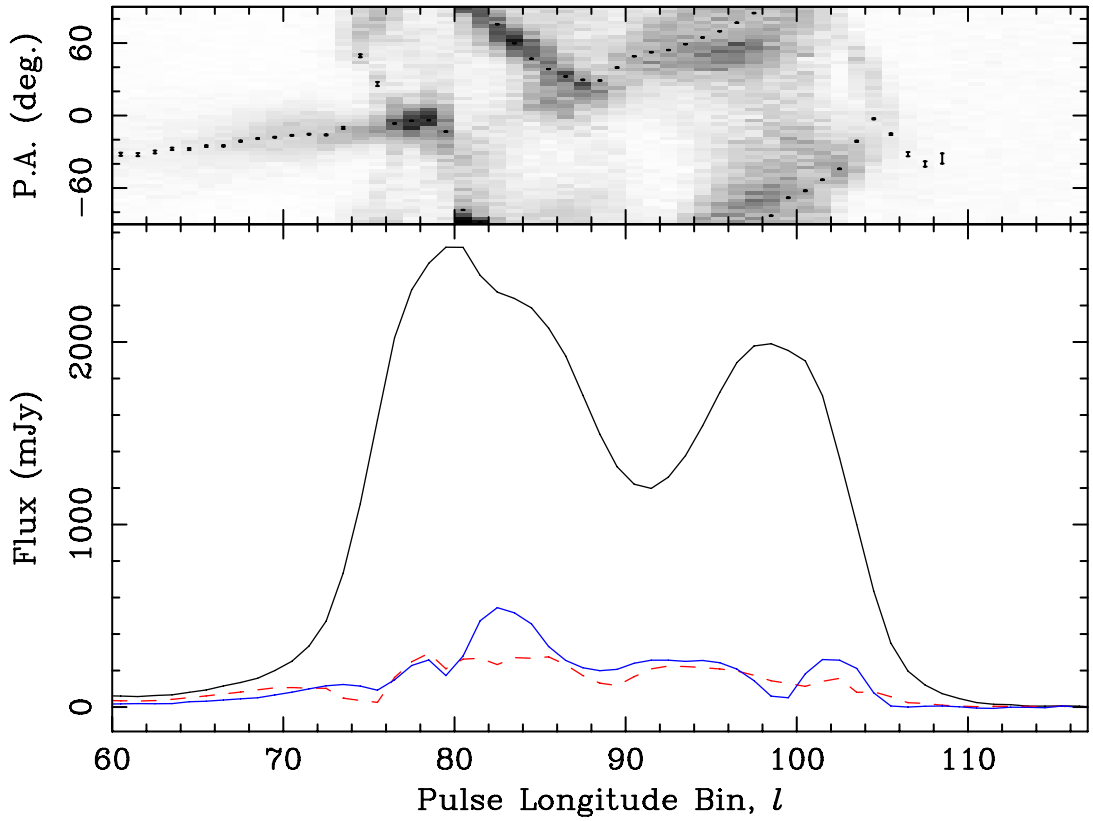

Figure 3.1: Longitude-resolved polarisation of PSR B1919+21. *Upper panel*: the position angle of the average Stokes parameters (vertical error bars) and a histogram of the position angles of the individual pulses (greyscale intensity). *Lower panel*: average Stokes parameters, including total intensity (black, upper solid), linear (red, dashed) and circular polarisation (blue, lower solid).

An additional frequency feature above $f_3 \sim 0.39 f_1$ is also evident in several pulse longitude bins of the leading component in the LRFS of Figure 3.2. The spectral power of this feature is in harmonic bins that are approximately twice that of the fundamental response of the quasi-periodic signal, which has also been reported by several authors for PSR B1919+21 (Weltevrede et al., 2007; Primak et al., 2022), and can be explained by the 180 degree phase shift between the drift bands that overlap at these pulse longitudes.

The above features are discussed in more detail in the following section, which focuses on the fluctuation spectra at specific pulse longitudes.

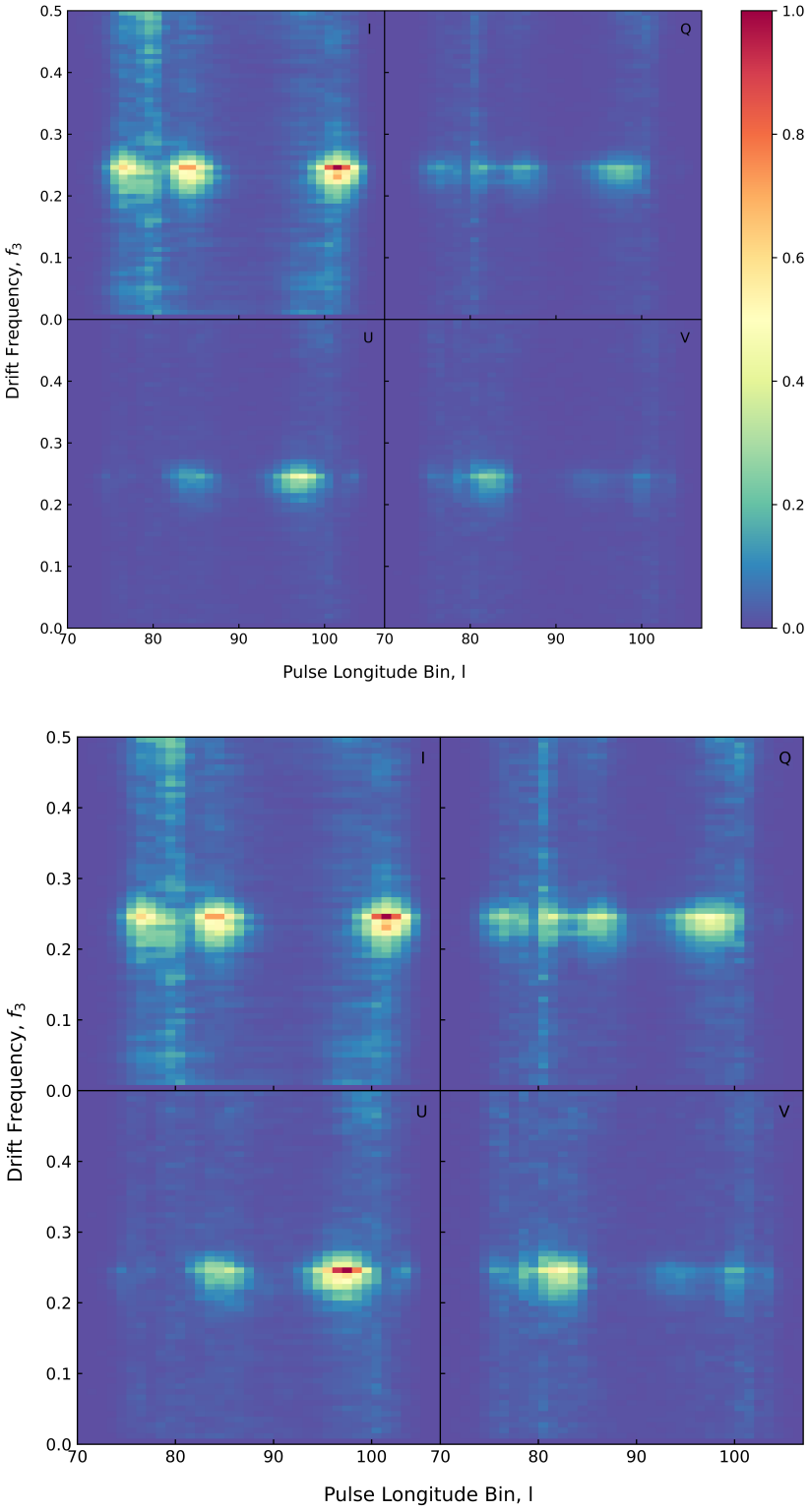

Figure 3.2: Longitude-resolved fluctuation spectra of the four Stokes parameters, integrated over all pulse sequences. The upper and lower panels show the region of the pulse profile that corresponds to the on-pulse window. The upper panel is normalised by the peak spectral power of the LRFS (total intensity). In the lower panel, only the PLRFS is normalised by the peak spectral power of Stokes Q, U, and V. The units of spectral power are arbitrary.

3.1.2 Slices of the SLRFS

There are several features of interest in the SLRFS that we explore further by plotting one-dimensional slices of the fluctuation spectra of the total intensity and polarisation at individual pulse longitude bins. In these plots, it is easier to estimate the significance of features and directly compare the periodic behaviour of all four Stokes parameters. The features that stand out as anomalous occur multiple times in several regions of the pulse profile, but in different configurations. We report on them in terms of the pulse longitude or range of pulse longitudes in which they appear.

Pulse longitude bins $75 \lesssim \mathrm{l} \lesssim 81$: Near the centre of the leading component, there is the fundamental response of the quasi-periodic signal in total intensity, Stokes Q and Stokes V. In the total intensity, there is a contiguous series of high-frequency harmonic bins that appear to exhibit fluctuations above the mean spectral power of the off-signal subset ($f_3 \gtrsim 0.39$; Figure 3.3). We refer to these modulations as a "double-frequency feature". Similarly, this range of pulse longitudes exhibits some modulations at low frequencies between $0.03 \lesssim f_3 \lesssim 0.08$ that could also be statistically significant. Stokes Q exhibits more significant white noise, resulting in the bright vertical band at l = 80 (Figure 3.2). l = 80 is where a longitudinal transition between primarily incoherent and partially coherent mode superposition occurs (Primak et al., 2022), and denotes a prolate spheroidal distribution of polarisation state in $\boldsymbol{p}$-space, consistent with incoherent OPM superposition (van Straten & Tiburzi, 2017).

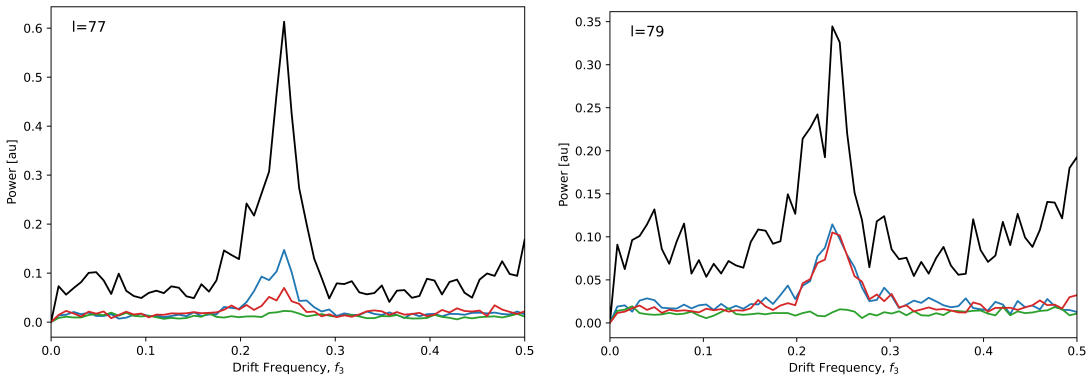

Figure 3.3: Stokes fluctuation spectra at pulse longitude bin l = 77 and l = 79, normalised by the peak fluctuation power in the SLRFS. The black solid line shows the fluctuation spectrum of the total intensity. The blue, green, and red solid lines show the fluctuation spectra of Stokes Q, U, and V, respectively.

Pulse longitude bins $83 \lesssim l \lesssim 89$: This region of pulse longitude exhibits bands of spectral power at only the fundamental response in all Stokes parameters, and there is little evidence of significant features at low frequencies or at double the frequency in any of the Stokes parameters (Figure 3.4). In pulse longitudes that are closer to the centre of the saddle region, the intensity of Stokes V drops off and fluctuations in Stokes Q and U rise to be dominant.

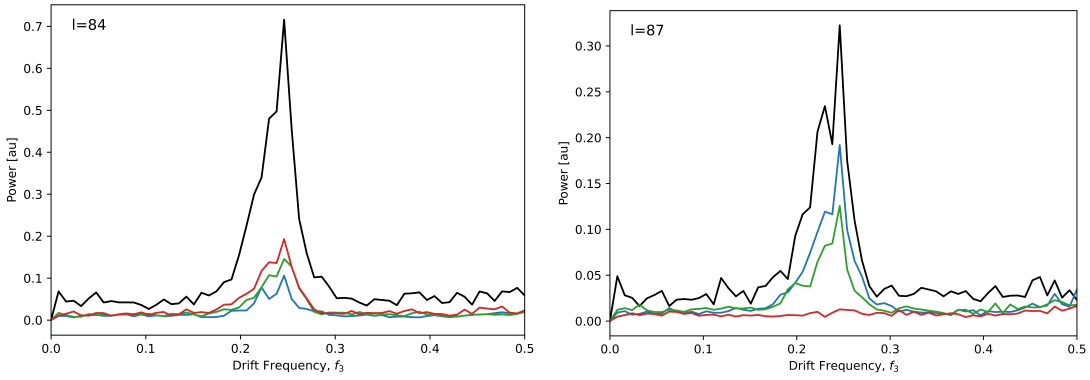

Figure 3.4: As in the caption of Figure 3.3, Stokes fluctuation spectra at pulse longitude bin l = 84 and l = 87.

Pulse longitude bins $93 \lesssim l \lesssim 95$: On the approximate boundary between the saddle region and the trailing component, the fundamental response is significant in only the elements of the Stokes polarisation vector, and fluctuations in total intensity

are weakened throughout most of the fluctuation spectrum; however, the spectral power of harmonic bins at double the frequency is marginally higher than the mean of the total intensity (e.g. at l = 93 in Figure 3.5). It is clear to see in the SLRFS (Figure 3.2) that the bands of spectral power in polarisation lead in the trailing component, and the band in total intensity lags in pulse longitude.

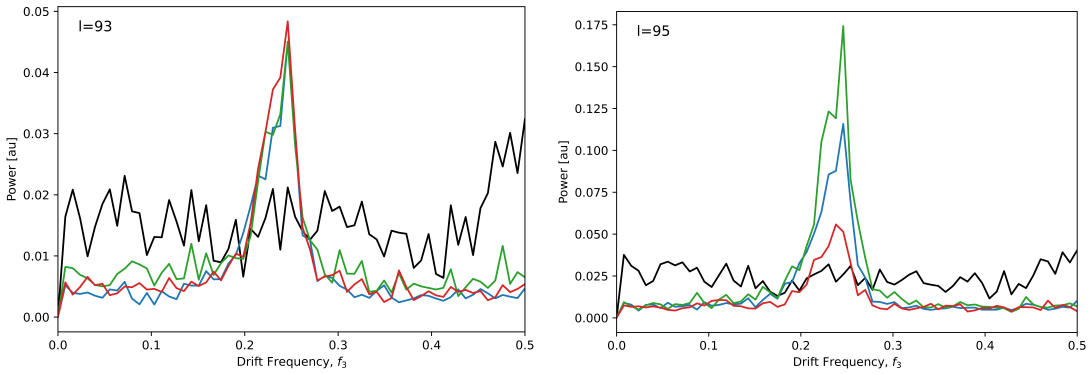

Figure 3.5: As in the caption of Figure 3.3, Stokes fluctuation spectra at pulse longitude bin l = 93 and l = 95.

Pulse longitude bins 96 $\lesssim$ l $\lesssim$ 98: Fluctuations of the Stokes parameters Q and U in the trailing component peak while there are little to no significant fluctuations in the total intensity. Although the fluctuation spectrum of the total intensity appears to be without significant periodic features, the slope of contiguous harmonic bins at low ($f_3 \lesssim 0.07$) and high ($f_3 \gtrsim 0.40$) frequencies suggest marginal evidence of spectral power. Pulse longitude l = 98 is similar to l = 96 and l = 97 in certain respects, but it is where the spectral power at double the frequency in Stokes Q and U begins to appear significant (Figure 3.7). The increase in intensity of this double-frequency feature in polarisation continues in the rest of the trailing component, and diminishes outside of the on-pulse window. The toroidal distributions of polarisation state and elliptical cycling are observed at these pulse longitude bins (Figure C.2).

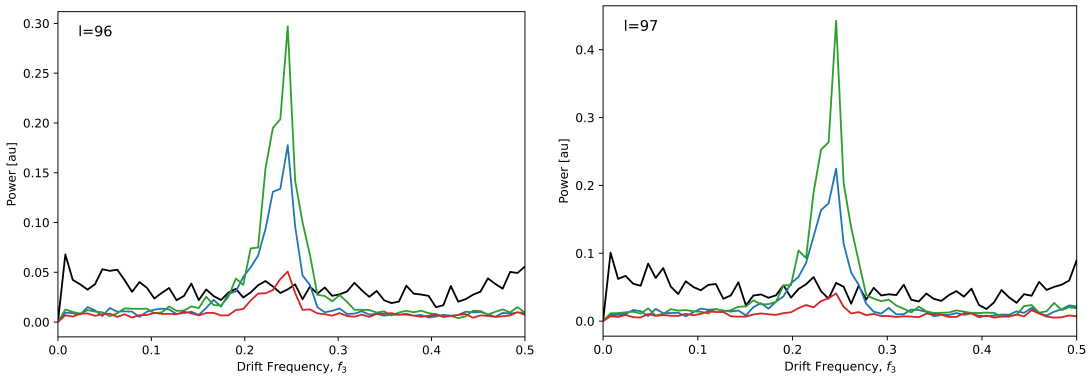

Figure 3.6: As in the caption of Figure 3.3, Stokes fluctuation spectra at pulse longitude bin l = 96 and l = 97.

Pulse longitude bin l = 99: The fluctuation spectra of the total intensity, Stokes Q, and Stokes U display a double-frequency feature that is significantly greater than the mean of the range of off-signal harmonic bins. Quasi-periodic features at low frequencies ($0.04 \lesssim f_3 \lesssim 0.07$ and $f_3 \approx 0.12$) are clearly above the mean of the fluctuation spectrum in total intensity. Periodicity is not exclusive to polarisation, but the fundamental response in Stokes U is greater than that of the total intensity.

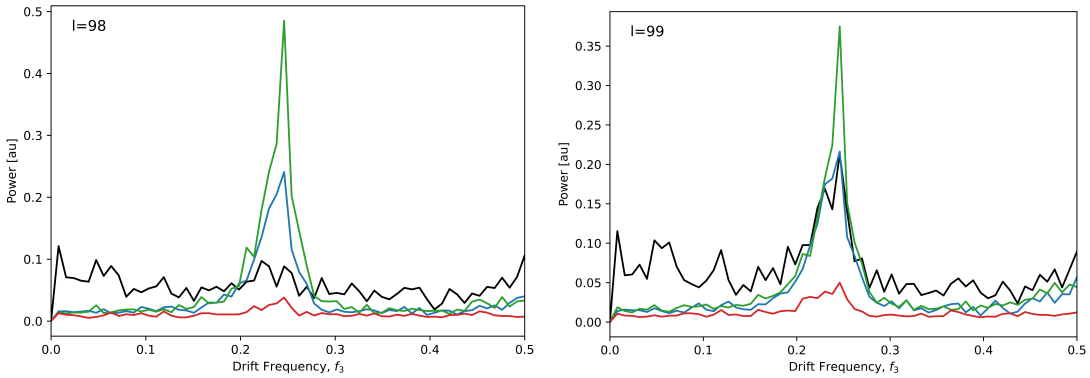

Figure 3.7: As in the caption of Figure 3.3, Stokes fluctuation spectra at pulse longitude bin l = 98 and l = 99.

Pulse longitude bins $100 \lesssim$ l $\lesssim 102$: The dominance of the fundamental response has swapped from polarisation to total intensity. In other words, a transition occurred from the bands of spectral power in Stokes Q and Stokes V, to that of the total intensity

(Figure 3.2). The double-frequency feature in polarisation (e.g. at l = 100 in Figure 3.8) is arguably significant, whereas the feature in total intensity has reduced down to mostly noise in comparison to the rest of the fluctuation spectrum. In like manner, the quasi-periodic features at low frequencies (as in Figure 3.7) go from being significant to blending in with the other non-periodic fluctuations.

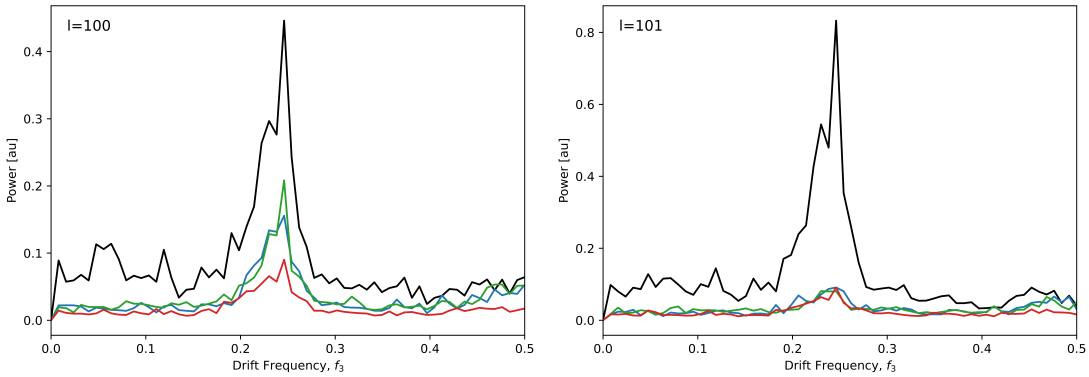

Figure 3.8: As in the caption of Figure 3.3, Stokes fluctuation spectra at pulse longitude bin l = 100 and l = 101.

The longitude-resolved fluctuation spectra of the on-pulse window exhibit a variety of periodic and non-periodic fluctuations in total intensity and polarisation. The occurrence of quasi-periodic fluctuations, which manifest as a characteristic broad fundamental response over a finite range of harmonic bins in the components of the Stokes polarisation vector, while being absent in the fluctuation spectrum of the total intensity, is an unexpected finding. Furthermore, frequencies in total intensity at double that of the fundamental response are evident in the absence of the fundamental response itself. Periodicity of the quasi-periodic signal exclusive to polarisation in any region of the pulse profile is extremely rare, and was first noted by Primak et al. (2022); the Fourier-based analysis developed in this thesis provides more sensitive limits on the existence of periodic modulations.

Pulse longitude l = 80 corresponds to the pulse longitude $\phi = -5.4°$ in Figure 8, Total Intensity, of Primak et al. (2022) where it is reported that two separate drift bands

that are 180° out of phase overlap. The observed rise in spectral power at frequencies double that of the fundamental response in the total intensity (e.g., Figure 3.3), which almost reaches an equivalent intensity of the peak, could be attributed to this overlap of drift bands. Weltevrede et al. (2007) refers to this spectral power excess as a "$P_3 = 2P_0$ flickering". The double-frequency feature is also observed in Stokes Q and Stokes U, but unlike the plausible explanations for its presence in total intensity, it becomes challenging to give an explanation for its appearance in polarisation.

Some pulse longitude bins in the on-pulse window also have a spectral response at low-frequency harmonic bins (e.g., $l = 81$, $l = 90$, and $l = 99$). We identify the low-frequency and double-frequency features as series of contiguous harmonic bins that appear to exhibit spectral power above the mean of the fluctuation spectrum; however, statistical quantification of the significance of these features is required in order to consider them in any conclusions we derive about the quasi-periodic behaviour of PSR B1919+21.

A plausible explanation for the origin of the drifting sub-pulses and synchronous quasi-periodic cycling of the Stokes polarisation vector around an elliptical path in $\boldsymbol{p}$-space should be able to encompass all of the periodic and non-periodic features observed in the longitude-resolved fluctuation spectra in polarisation and total intensity, and be able to describe the different configurations in which the features appear.

3.1.3 Quasi-Periodicity of the Drift Frequency

To observe how the quasi-periodic modulations of the drift period P_3 in total intensity and polarisation vary over time, the SLRFS computed for each N-pulse sequence is integrated over the pulse longitude bins that belong to the on-pulse window and is

plotted as a function of drift frequency and time (Figure 3.9):

$$S_{k\mu}(T) = \sum_{l \epsilon \Phi_{\mathrm{on}}} \boldsymbol{P}_{Tkl\mu} \boldsymbol{P}_{Tkl\mu}{}^{*} \tag{3.3}$$

The modulation pattern of $S_{k\mu}(T)$ in Figure 3.9 is almost identical across all four Stokes parameters, with slight variations in spectral power. This is consistent with the evidence for the drift-synchronous polarisation modulations of PSR B1919+21 discovered by Primak et al. (2022) and shown in Figure 3.2.

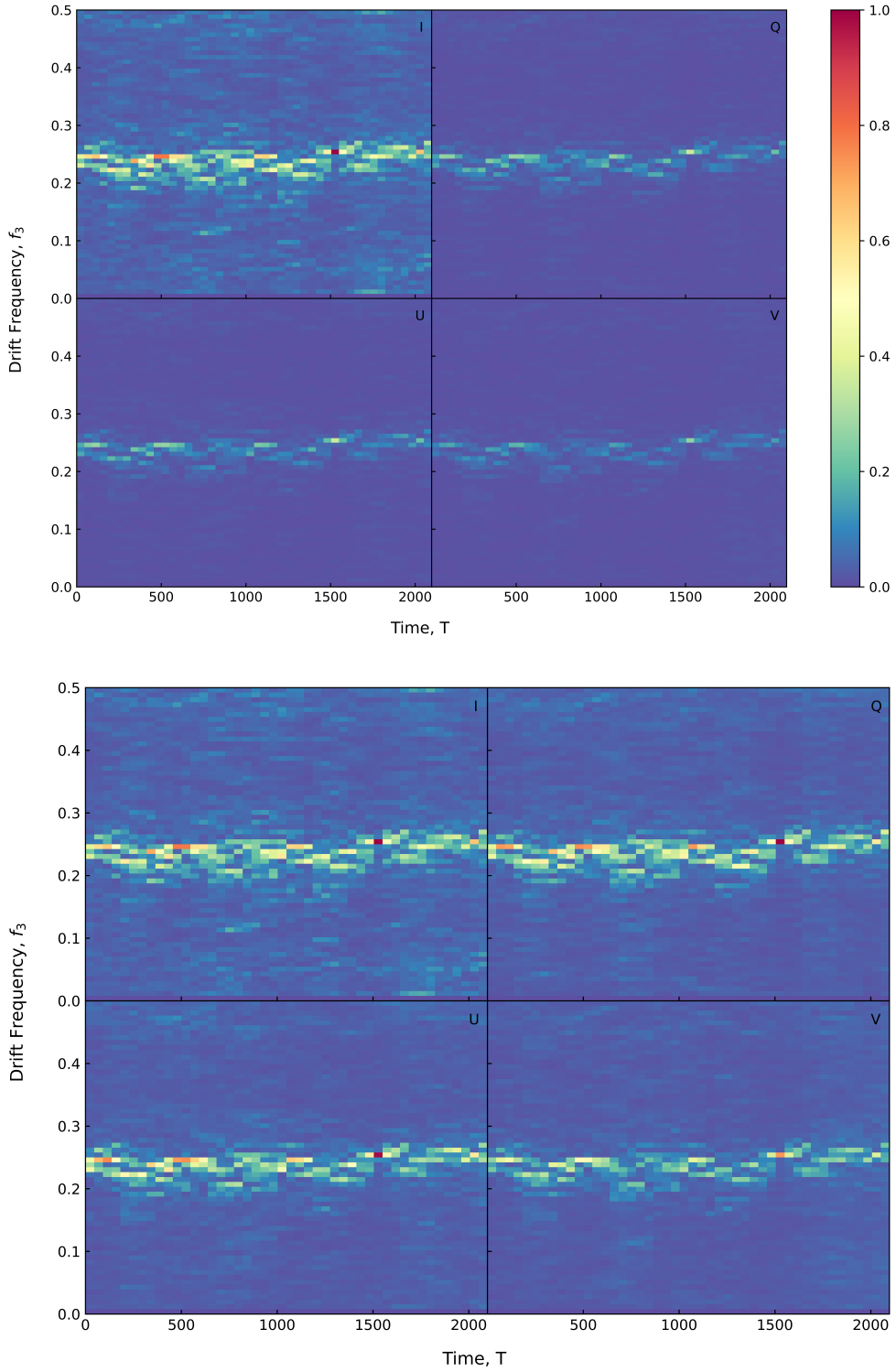

Figure 3.9: Fluctuation spectra as a function of time T (seconds) in total intensity and polarisation, integrated over the on-pulse window and derived from a spectral analysis with an FFT step size of 32 pulses (Equation 2.9). Refer to the caption of Figure 3.2 for further details on the normalisation of the panels and units.

Time-dependent variations of the drift frequency appear systematic, analogous to a drift-band modulation pattern (e.g. Figure 1.1). Periodic modulation of the drift frequency is unexpected and, to the best of our knowledge, has not been previously reported in the published literature on P_3 variations. Approximately five cycles of P_3 variations are evident in Figure 3.9, with peaks in both drift frequency and fluctuation intensity across all elements of the SLRFS. The first three peaks have a drift frequency of $f_3 \approx 0.24$, and the other two of $f_3 \approx 0.25$. Figure 3.10 below presents the sum of three on-signal harmonic bins in the time-dependent fluctuation spectrum of the total intensity. The maxima tend to occur on the trailing edge of each peak; therefore, we use these to define the time of each peak as $T_1 \approx 100$, $T_2 \approx 550$, $T_3 \approx 1100$, $T_4 \approx 1500$, and $T_5 \approx 2050$. The average interval between the peaks provides an estimate of the average period of the drift frequency as 487.5 seconds.

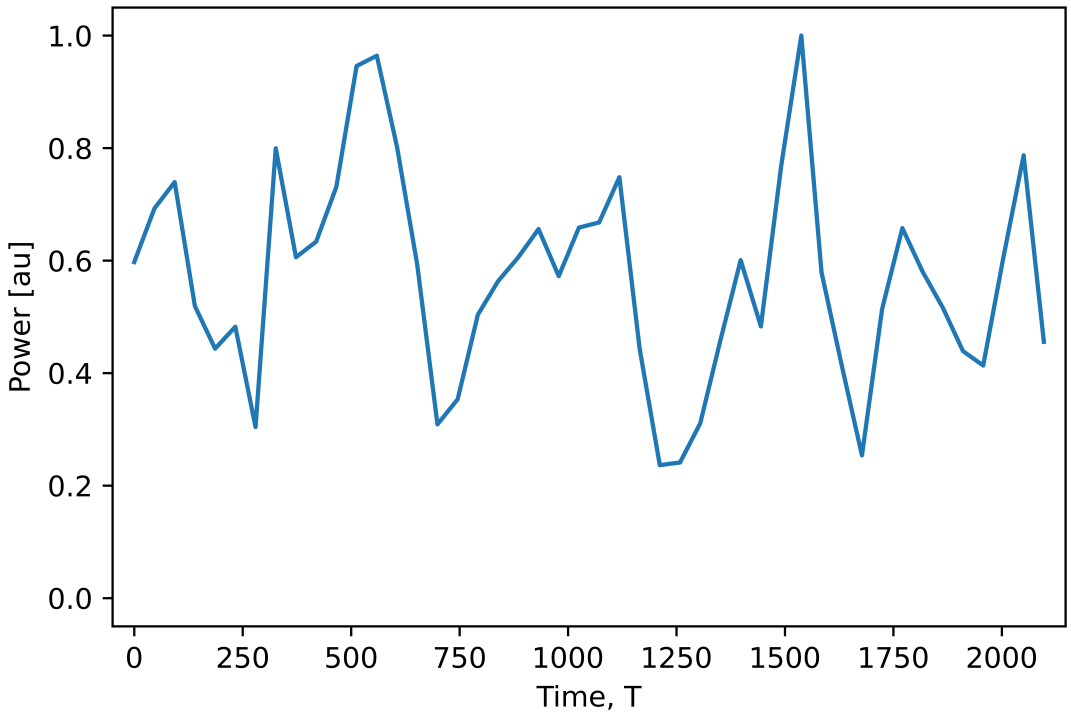

Figure 3.10: Sum of three on-signal harmonic bins (k = 30, k = 31, and k = 32) from $S_{k\mu}(T)$, where μ = 0, normalised by the maximum. There are approximately five cycles of P_3 variations.

The stochastic white noise in all elements of the SLRFS also exhibits low-frequency background modulations, particularly observed as vertical minima in $S_{k\mu}(T)$ that are aligned with the brightest peaks in the periodic cycles of $S_{k\mu}(T)$. Initially, we speculated that the discrete Fourier transform may be sensitive to steps ($N_{\rm step}$; Equation 2.9) with a power of 2 (i.e., 2^n), and that a separation between pulse sequences that is not 2^n may remove the background noise modulation artifact. The spectral analysis was repeated multiple times using FFT step sizes that did not have a power of 2, and many of them were prime numbers. These included $N_{\rm step}$ = 10, $N_{\rm step}$ = 13, $N_{\rm step}$ = 23, $N_{\rm step}$ = 37, and $N_{\rm step}$ = 49. This analysis showed that the long-period stochastic white noise modulations remain in the fluctuation spectra after a spectral analysis with an FFT step of any size, and that the modulation pattern of P_3 is consistent and smoothed over periods of T. For example, the spectral analysis with an FFT step size of $N_{\rm step}$ = 10 is presented in Figure 3.11.

In the following section (Section 3.1.4), we estimate the period of the observed drift frequency and stochastic white noise modulations and support our estimation by computing a one-dimensional Fourier transform of $S_{k\mu}(T)$ along vectors of constant harmonic bin.

The leading and trailing components of the pulse profile are separated by the saddle region where the flux density of the total intensity is diminished ($89 \lesssim l \lesssim 95$). To ensure that the modulation pattern of P_3 observed in Figure 3.9 spans the whole emission region, and is not just a factor of integrating the LRFS and PLRFS over all of the pulse longitude bins that belong to the on-pulse window, we performed the integration of the LRFS and PLRFS over discrete portions of the pulse profile that correspond to the leading and trailing components. The time-varying drift SLRFS, $S_{k\mu}(T)$, for each component is shown in Figures 3.12 and 3.13, respectively, which shows that the periodic modulation pattern in total intensity and polarisation is consistent between the leading and trailing regions of pulse longitude.

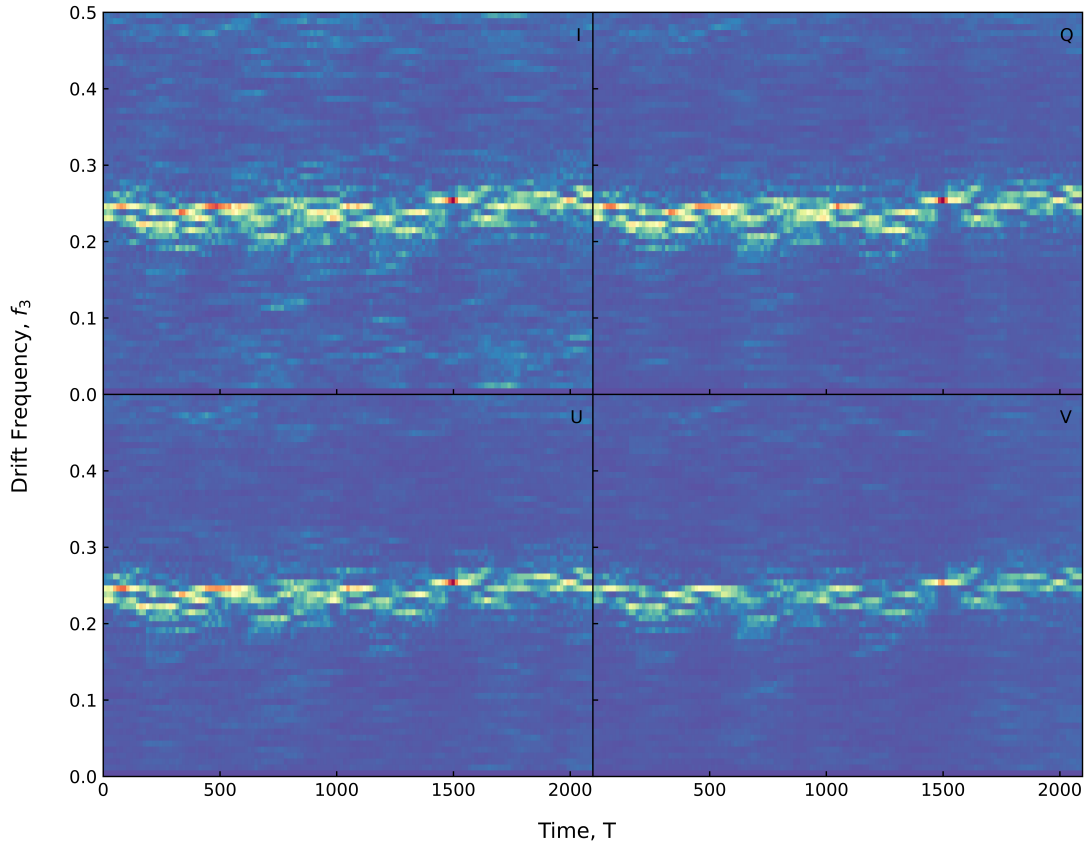

Figure 3.11: The fluctuation spectra in this figure are derived from a spectral analysis with an FFT step size of 10 pulses (Equation 2.9). Refer to the caption of Figure 3.9 for further details.

$S_{k\mu}(T)$ of the trailing component shows a cluster of low-frequency points in total intensity at periods of time above $T > 1500$; however, there is not enough evidence in the fluctuation spectrum to form an analogy to the low-frequency feature reported in the literature (Backer, 1973; Lang, 1969; Rickett, 1970). The trailing component also shows greater overall spectral power when compared to the fluctuation spectra of the leading component, possibly because the leading component (more clearly) exhibits the existence of two overlapping drift bands that are 180 degrees out of phase, and such overlap reduces the modulations at the fundamental frequency. There is more evidence of periodicity in the Stokes Q and U elements of the trailing component than there is in the leading component, which exhibits more evidence for periodicity in the element of circular polarisation (Stokes V). The background white noise modulations are more

apparent in the lower panel of Figure 3.12, possibly owing to the diminished level of spectral power that allows smaller variations to have a greater contrast on the colour gradient of the plot. The lower panel of Figure 3.2 highlights bands of spectral power in regions of pulse longitude that correspond to the leading and trailing components. The independent analysis of each pulse profile component and the overall spectral power in each of the Stokes parameters is consistent with the bands of spectral power in the Stokes longitude-resolved fluctuation spectra (Figure 3.2).

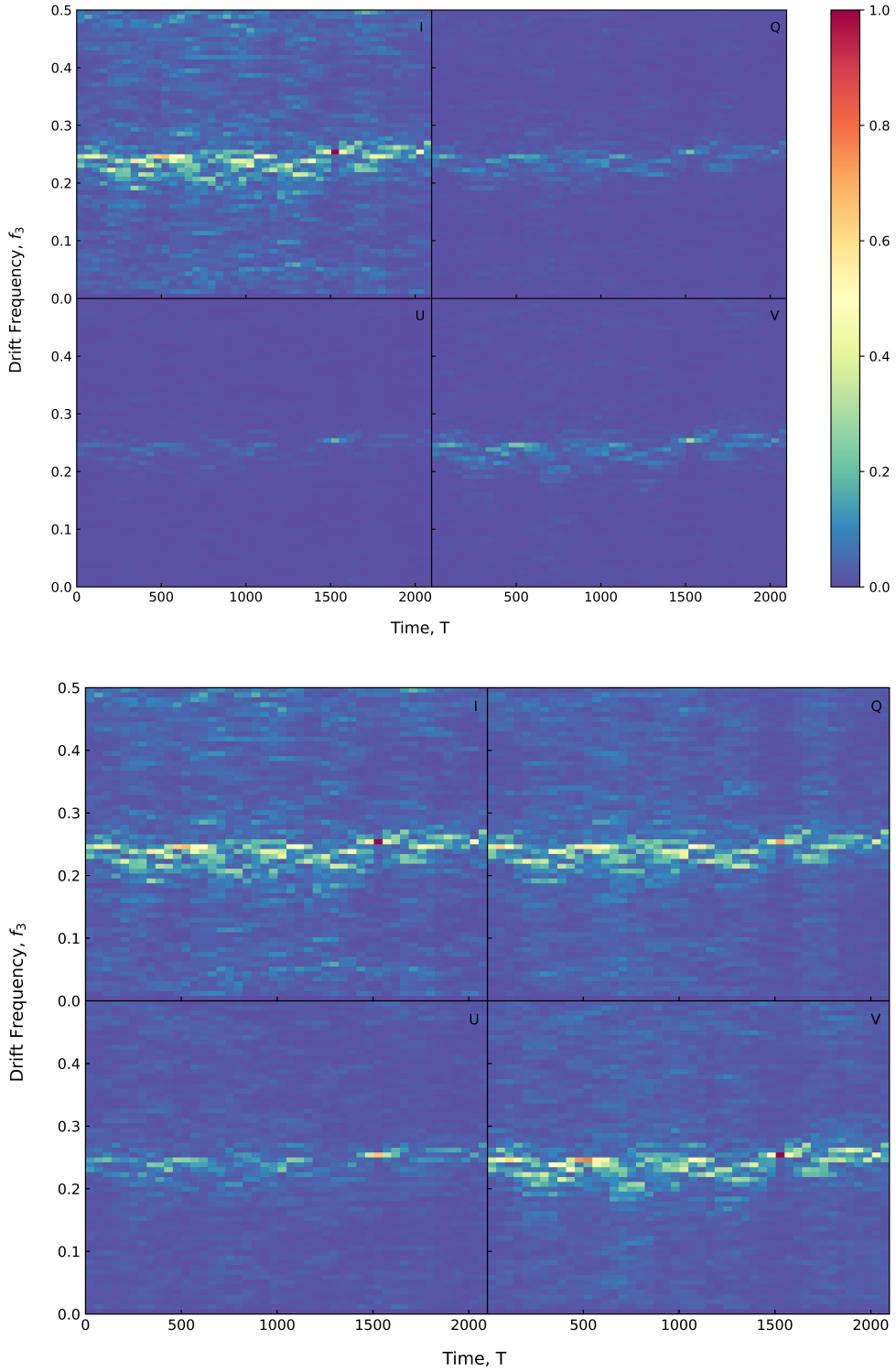

Figure 3.12: Fluctuation spectra integrated over the leading component of the pulse profile. Refer to the caption of Figure 3.9 for further details.

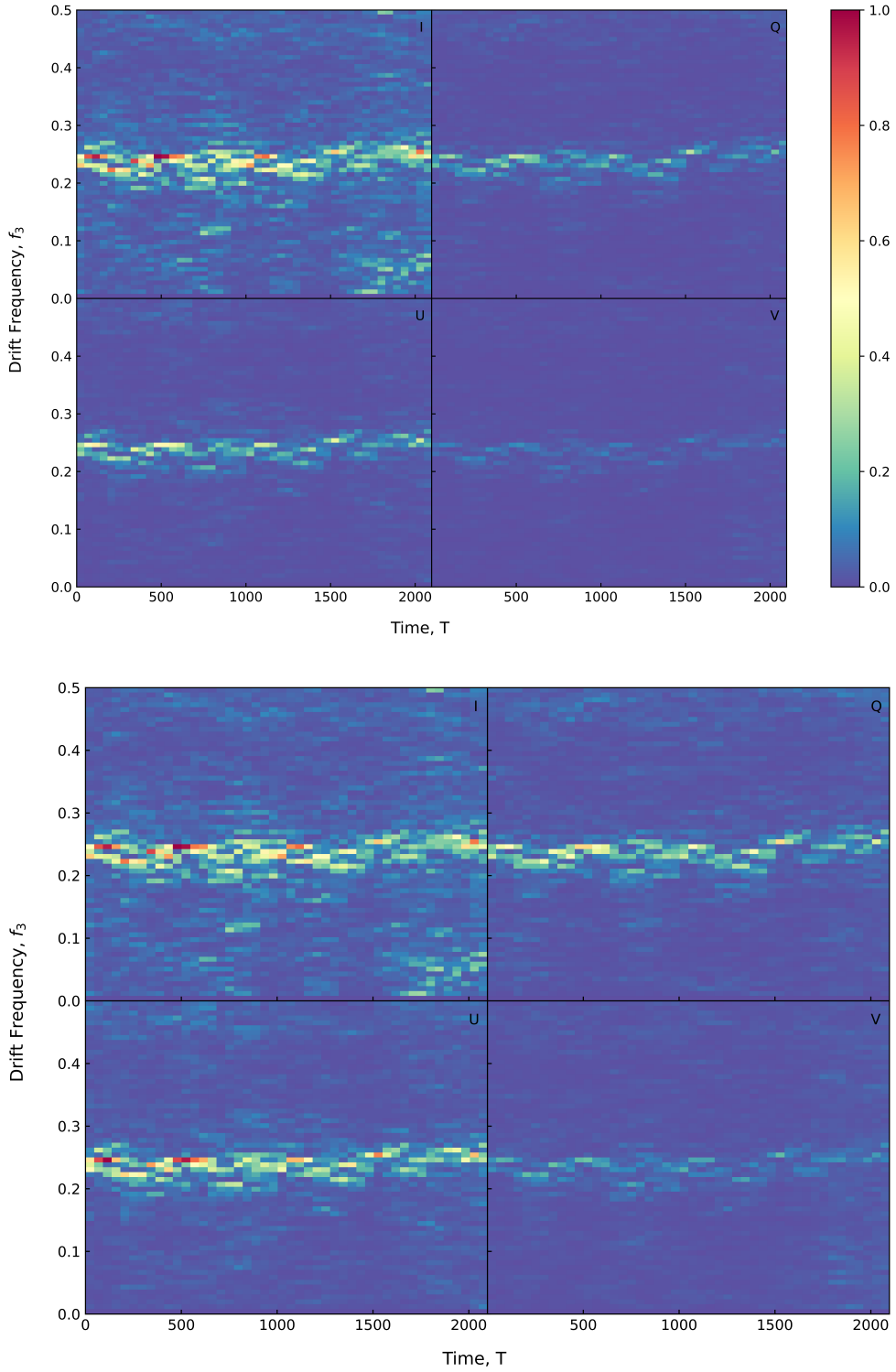

Figure 3.13: Fluctuation spectra integrated over the trailing component of the pulse profile. Refer to the caption of Figure 3.9 for further details.

3.1.4 Average Period of the Drift Frequency Variations

The drift period P_3 (Section 3.1.3) exhibits time-varying behaviour that suggests periodic frequency modulation or drifting of the drift period, characterised by a drift-band-like structure in Figure 3.9. This type of quasi-periodic drift frequency modulation has never been reported before. Staelin et al. (1970) discuss periodic fluctuations of the total intensity of PSR B1919+21 and do not report that the frequency of Stokes I modulations fluctuate; on the contrary, they report that P_3 is "relatively stable". They observed long-period variations in total intensity in the form of strong pulse-intensity bursts with a period of approximately $P_4 \approx 345$ seconds. Counter to their assertion of the relative stability of the drift period P_3, our analysis in Section 2.5.2 shows that it is in fact quasi-periodic (Figure 3.9), as evidenced by the span of the fundamental response over finite ranges of harmonic bins in the longitude-resolved and time-resolved fluctuation spectra (Figures 3.2 and 3.9, respectively).

The dataset from Hankins and Rankin (2010) provides 1624 single pulses from PSR B1919+21. This spectral analysis consists of 1568 of those pulses that span a total integration length of approximately 2097.04 seconds, which is just over 500 more pulses than what Staelin et al. (1970) studied. Each of the five cycles (highlighted in Section 3.1.3) then has an average period of P_4 = 419.41 seconds, which is approximately 20% greater than the long-period variations of the total intensity observed by Staelin et al. (1970). The dissimilarities between the observed periodic frequency modulations of the drift period and the value for P_4 from the literature may arise due to the difference in number of pulses analysed in each of the studies, the fact that the periodicity is not well defined (Figure 3.14), and that it may fluctuate on arbitrary timescales, including the possibility that it evolved between 1970 and 1992.

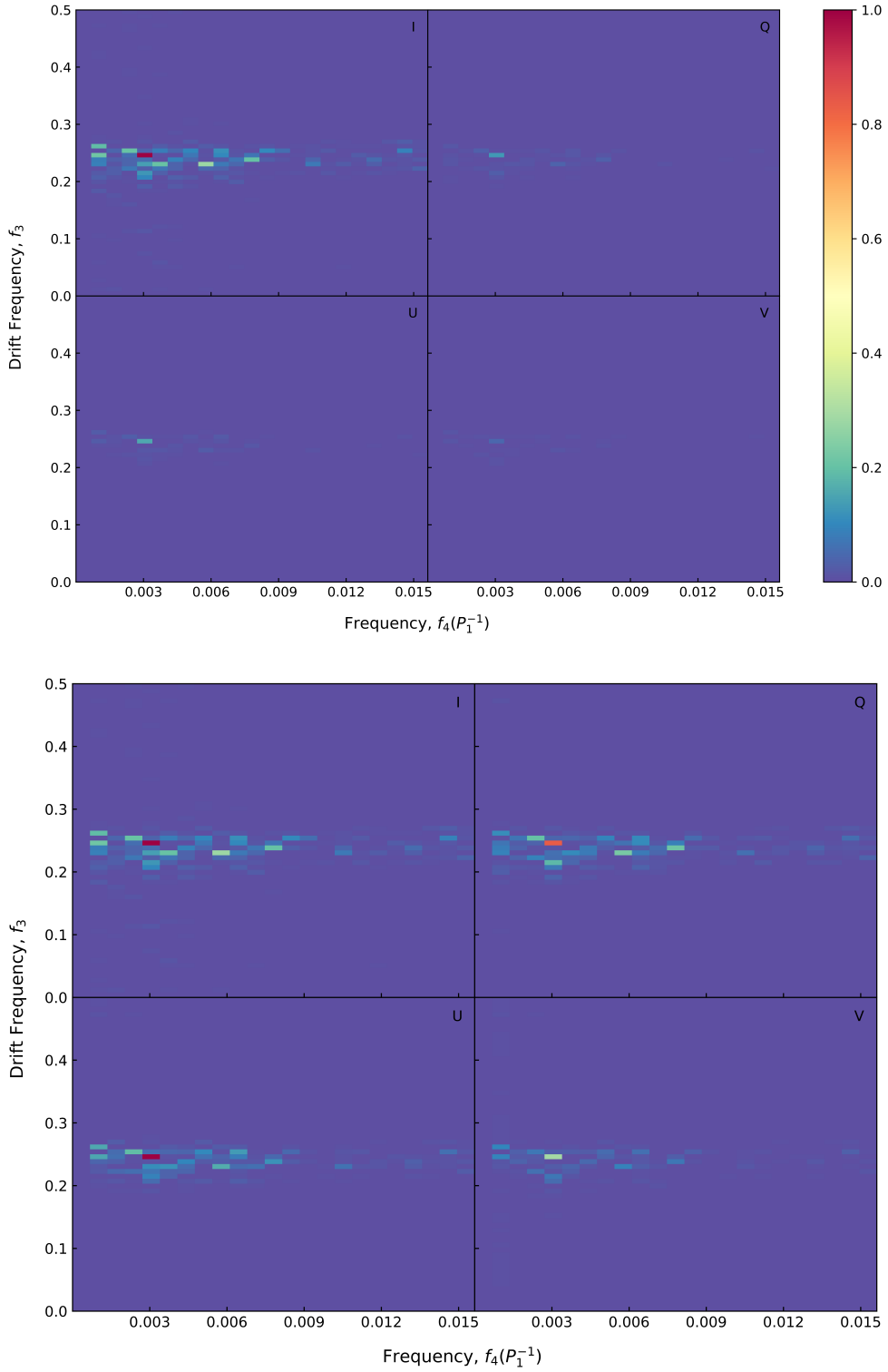

Figure 3.14: Fluctuation spectra of the periodic fluctuations of the drift frequency as observed in Figure 3.9. Refer to the caption of Figure 3.2 for further details on the normalisation of the panels and units.

We further investigated the modulation pattern of the drift period and performed a one-dimensional Fourier transform along vectors of constant drift frequency (harmonic bin, k), resulting in a two-dimensional fluctuation spectrum, the P4FS. In Figure 3.14, the y-axis represents the drift frequency f_3 (defined in Section 3.1.1), while the x-axis corresponds to the frequency of the quasi-periodic modulation of the fluctuation power in each harmonic bin, $f_4 = \frac{1}{P_4}$. The lower panel of Figure 3.14 shows that the total intensity and polarisation exhibit a fundamental response at $k = 4$, indicating that the periodic drifting of the drift frequency is synchronous across all of the Stokes parameters. Stokes V exhibits a band of spectral power that spans the full f_3 spectrum at $k = 1$.

The number of pulse sequences the Fourier transform was computed over was small ($N_T = 46$ sequences). For confidence and consistency, the spectral analysis of $S_{k\mu}(T)$ was repeated several times where the fluctuation spectra of the drift period were derived utilising different FFT step sizes. According to Equation 2.9, decreasing the number of pulses in each FFT step size, $N_{\rm step}$, increases the number of pulse sequences N_T. The non-normalised P4FS derived from the analyses with $N_{\rm step} = 10$ and $N_{\rm step} = 23$ are shown in the upper and lower panels, respectively, of Figure 3.15. Owing to rounding, the total time spanned by the sequence of pulse sequences changes slightly with different values of $N_{\rm step}$, where the upper panel spans 2150.54 seconds, and the lower panel spans 2139.84 seconds. The span of each harmonic bin in the P4FS, Δf, is a reciprocal of the total time and therefore changes only by about 0.5%. Therefore, the spectral content of the periodic drifting of the drift period observed in the fluctuation spectra should not change that much, or at all, when the Fourier transform is computed over sequences of pulse sequences of marginally different lengths. This is seen in the similarities shared between the features of the P4FS derived from spectral analyses with differing FFT step sizes in Figure 3.15. Its presence in all of the elements of the Stokes polarisation vector shows that what is observed in total intensity is also exhibited synchronously in

polarisation. This is an unexpected finding of the research and development undertaken as part of this thesis. Its discovery exemplifies the potential for the extension of the PLRFS-based approach to learn more about the wider population of pulsars that exhibit quasi-periodic sub-pulse drifting.

The spectral power of the long-period cycling of drift frequency is contained in the first 5 harmonics of the fluctuation spectrum shown in Figure 2.6. We subtracted the power in the DC bin of this spectrum by removing the average over pulse number ($\langle I_l \rangle$ and $\langle \boldsymbol{p}_l \rangle$ in Equations 2.4 and 2.5, respectively). We also modelled the SEFD and gain variations as a function of time in Section 2.2), which in principle should subtract some low-frequency power in the fluctuation spectrum; however, this procedure did not (and fundamentally could not) remove the frequency modulation that is observed in Figures 3.9 and 3.14. Therefore, it is plausible that the quasi-periodic drift frequency modulation is the source of the residual low-frequency power seen in Figure 2.6. Similarly, this quasi-periodic drift frequency modulation should be distinguished from, though it may be related to, the low-frequency intensity modulation first noted by Lang (1969) and Rickett (1970).

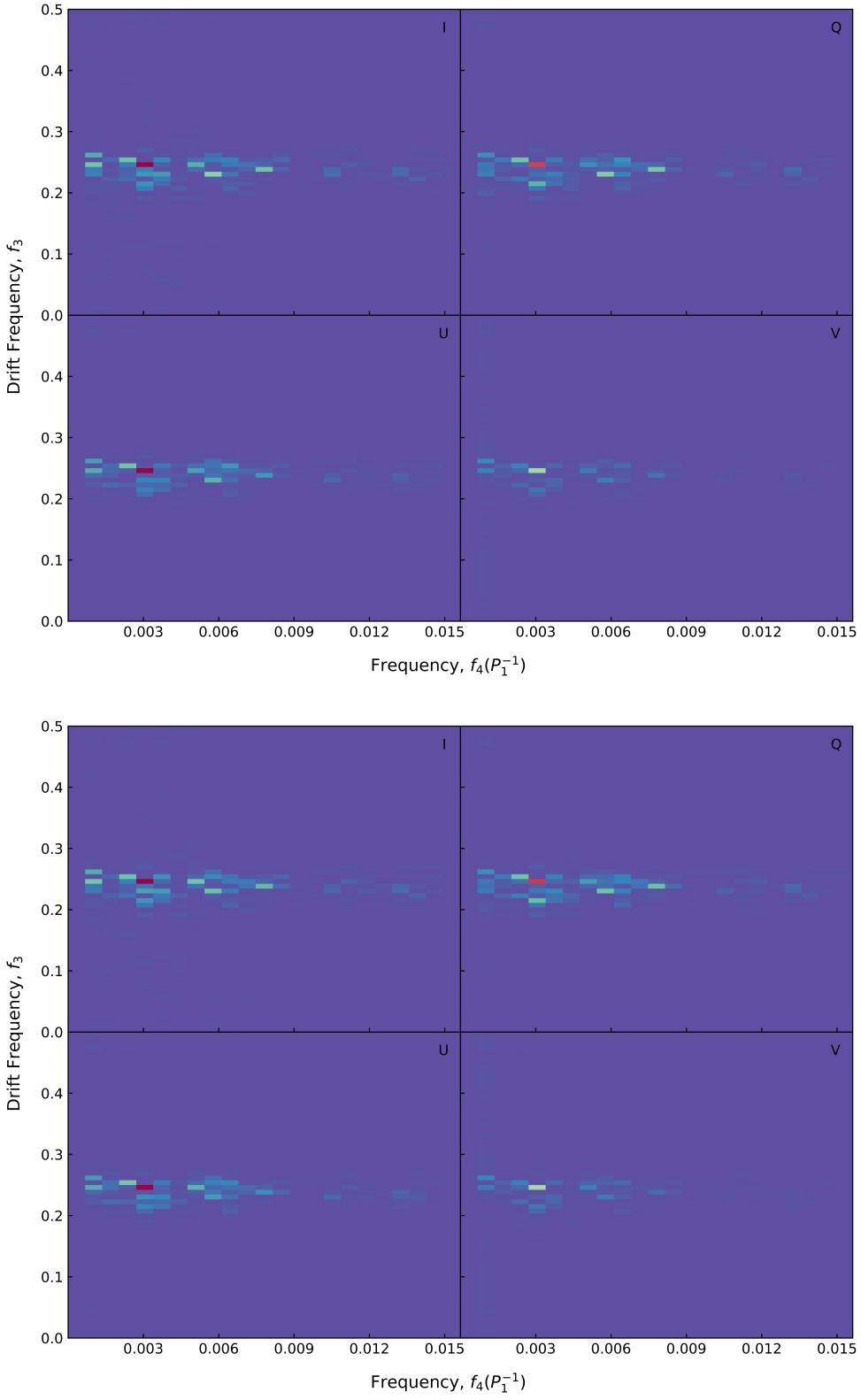

Figure 3.15: Fluctuation spectra of the periodic fluctuations of the drift period (P_4) as observed in Figure 3.9. The $S_{k\mu}(T)$ used to obtain the upper and lower panels are derived from the spectral analysis with FFT step sizes of 10 and 23 pulses, respectively. Refer to the caption of Figure 3.2 for further details on the normalisation of the panels and units.

3.2 Polarisation Statistics

3.2.1 Parseval's Theorem

Parseval's Theorem states that the total energy of a signal can be computed by integrating the squared amplitude of the signal over time or by integrating the squared amplitude of its Fourier transform over frequency. By extension, in our multivariate analysis of the Stokes parameters, the polarisation fluctuation coherency matrix (PFCM) that we compute by integrating the polarisation fluctuation cross spectrum (PFCS) over the full spectrum, K, is equivalent to the real-valued covariance matrix derived from the auto- and cross-correlations between the Stokes parameters (Primak et al., 2022). This equivalence enables us to verify the consistency between the frequency-domain methodology developed as part of this thesis and the time domain methods used in previous studies. Figure 3.16 demonstrates the expected consistency by comparing the complex-valued full-spectrum PFCM to the real-valued covariance matrix computed in the time domain by Primak et al., (2022), and is discussed further in Section 3.2.2.

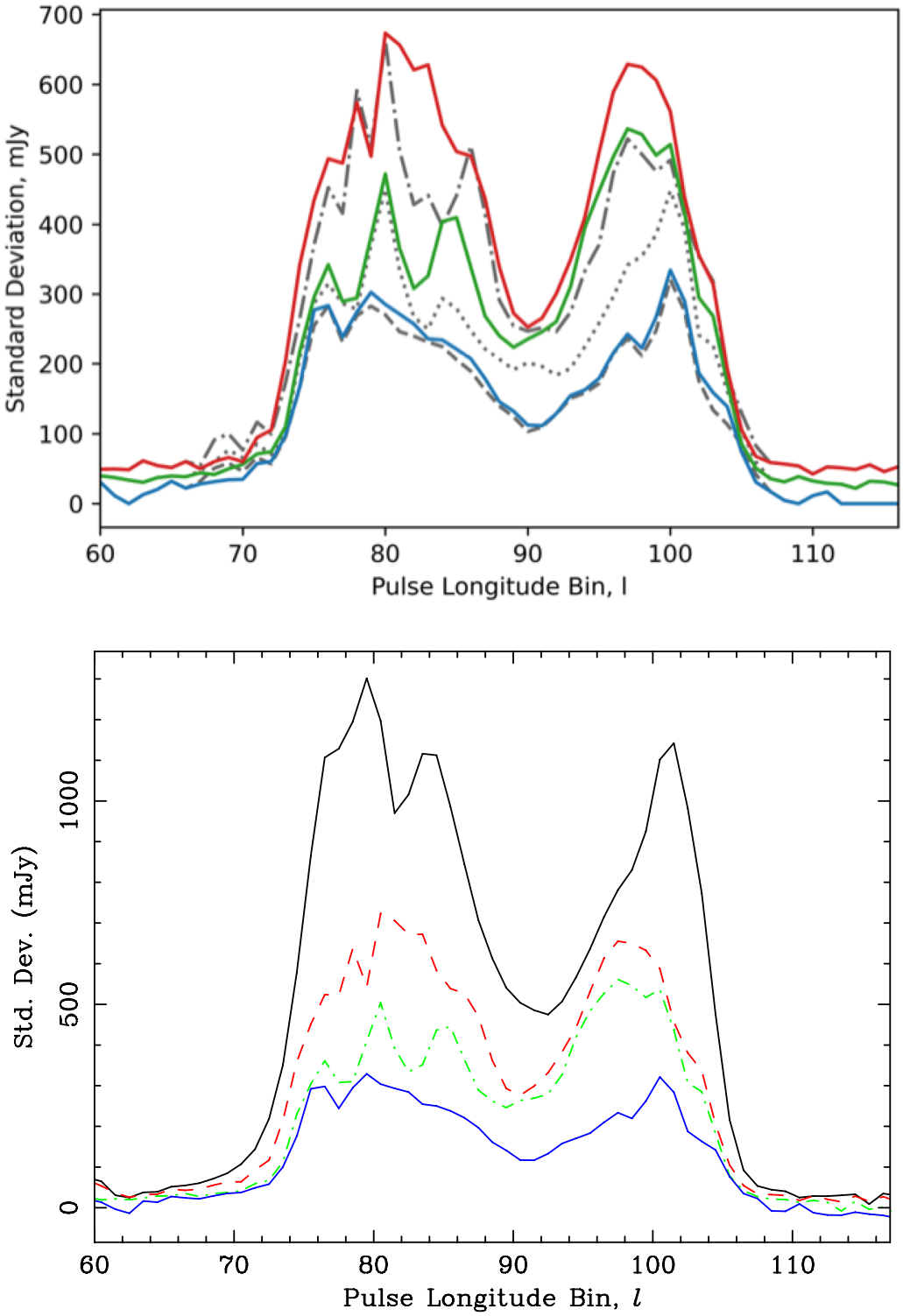

Figure 3.16: The red, green, and blue lines of both panels show the square-roots of the eigenvalues (in descending order, respectively). *Upper panel*: The coloured eigenvalues are derived from the spectral analysis of the full spectrum, $\mathbf{C}_l(K)$. The grey dash-dotted, dotted, and dashed eigenvalues (in descending order, respectively) are derived from the off-signal ranges of the PLRFS, $\mathbf{C}_l(K_{\rm off})$, that characterise the white self-noise of the pulsar. *Lower panel*: The black solid line shows the standard deviation of the total intensity.

3.2.2 Eigenvalues

Figure 3.16 displays the eigenvalues derived from both the frequency and time domains (Section 3.2.1). The upper panel also includes the eigenvalues derived from the analysis of the off-signal harmonic bins, $K_{\rm off}$, which characterise the white self-noise components of the pulsar-intrinsic signal and can be used to quantify the significance of the quasi-periodic modulations in the elements of the Stokes polarisation vector. For example, let $\sigma_{i,l}(K)$ and $\sigma_{i,l}(K_{\rm off})$ ($i = 1, 2, 3$) denote the longitude-resolved eigenvalues derived from the eigendecomposition of $\mathbf{C}_l(K)$ and $\mathbf{C}_l(K_{\rm off})$, respectively (Equation 2.10). Where $\sigma_{i,l}(K) = \sigma_{i,l}(K_{\rm off})$, there is no evidence for the presence of a periodic process of sub-pulse modulations. Pulse longitude bins where $\sigma_{i,l}(K) \gg \sigma_{i,l}(K_{\rm off})$ provide evidence of periodic fluctuations in the fluctuation spectra of the corresponding pulse longitude bins.

The eigenvalues derived from the eigendecomposition of the full-spectrum PFCM, $\sigma_{i,l}(K)$, in the upper panel of Figure 3.16 define the shape of the ellipsoidal cloud formed in $\boldsymbol{p}$-space. As highlighted by Primak et al. (2022), the range $94 \lesssim l \lesssim 98$ exhibits an unexpected oblate spheroidal distribution of $\boldsymbol{p}$ ($\sigma_1 \approx \sigma_2 > \sigma_3$), inconsistent with the prolate spheroidal distribution expected for an incoherent superposition of OPMs (van Straten & Tiburzi, 2017). The eigenvalue that corresponds to the blue solid line in the upper panel of Figure 3.16 is approximately equal to the smallest (dashed) white self-noise eigenvalue across most pulse longitude bins. This suggests that there are no significant periodic fluctuations in the direction of the eigenvector in $\boldsymbol{p}$-space that is associated with the smallest eigenvalue. The red and the green (largest and second-largest) eigenvalues are greater than the dash-dotted and dotted white-noise eigenvalues (respectively) over most of the on-pulse window from $l = 82$ to $l = 100$. This suggests that periodic fluctuations contribute significantly to the ellipsoidal distribution of the Stokes polarisation vector over most of the emission.

The eigenvalues $\sigma_{i,l}(K_{\rm on})$ that were computed over the finite range of on-signal harmonic bins (shown in Figure 3.17) do not describe the three-dimensional distribution of the Stokes polarisation vector in $\boldsymbol{p}$-space in the same way that the full spectrum eigenvalues $\sigma_{i,l}(K)$ do. Rather, they indicate the presence of quasi-periodic variations in the signal. This method is necessary only for quasi-periodic signals because, in the case of pulsars that exhibit periodic or coherent drifting sub-pulses, the fundamental response would be confined to a single coefficient of the fluctuation spectrum and the extension of the PLRFS-based approach would not be required (Edwards, 2004). An on-signal eigenvalue with significant intensity at a given pulse longitude bin denotes a single quasi-periodic oscillation of the Stokes polarisation vector around an elliptical path in $\boldsymbol{p}$-space. Each significant eigenvalue has a corresponding eigenvector that describes the geometry of the elliptical path, such as its shape (semi-major and semi-minor axes) and orientation (direction of the normal to the elliptical path). Over the entire emission region in Figure 3.17 a single eigenvalue has significantly greater intensity than the grey white self-noise eigenvalues (i.e., $\sigma_{1,l}(K) \gg \sigma_{i,l}(K_{\rm off})$, where $68 \lesssim l \lesssim 106$), indicating the existence of a single elliptical path in $\boldsymbol{p}$-space around which the Stokes polarisation vector cycles quasi-periodically. The primary eigenvector corresponding to the single significant eigenvalue is defined and analysed in the following section.

No evidence of periodicity is expected in the off-pulse regions of the pulse profile since the radio emission beam is outside of the line of sight of the observer/receiver. The coloured eigenvalues should then be equal to the grey white noise eigenvalues at pulse longitudes that do not belong in the on-pulse window ($l \lesssim 68$ and $l \gtrsim 105$). The result of our analysis of the on-signal subset of the full spectrum in Figure 3.17 is consistent with the design of the subset classification algorithm in Section 2.4 and the derivation of the PFCM $\mathbf{C}_l(K)$, where $l \in \Phi_{\rm on}$, in Section 2.5.2.

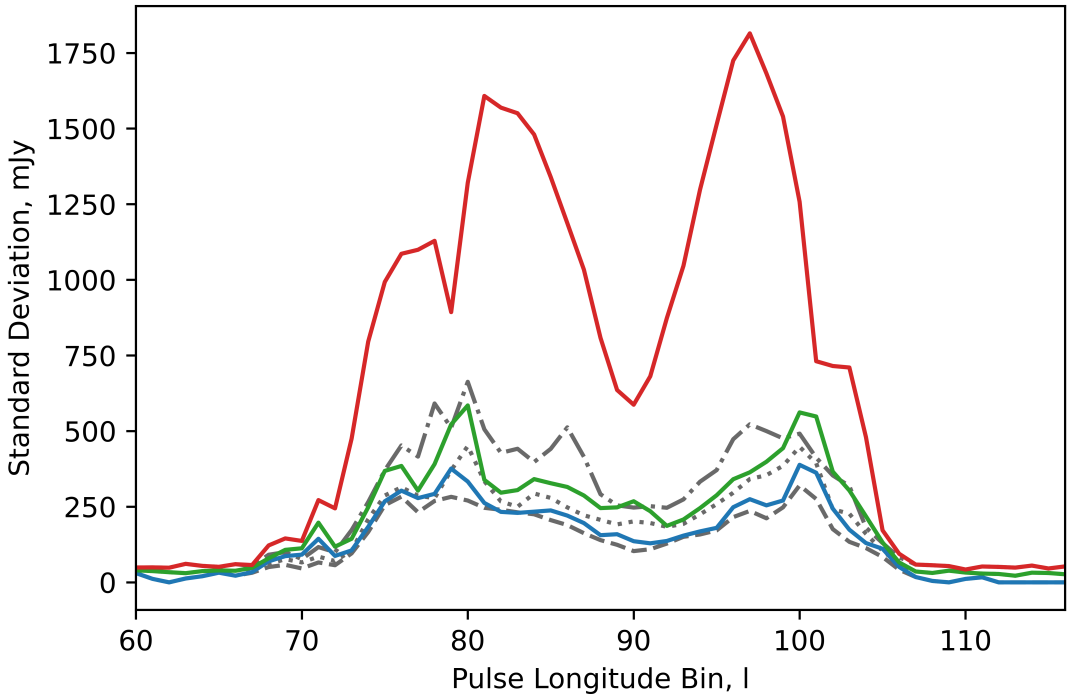

Figure 3.17: The red, green, and blue solid lines show the square roots of the eigenvalues (in descending order, respectively) derived from a subset of the full spectrum, $K_{\rm on} \subset K$, that confines the quasi-periodic signal. The grey dash-dotted, dotted, and dashed lines (in descending order, respectively) are derived from the off-signal ranges, $K_{\rm off}$, that characterise the white self-noise of the pulsar and are the same as those shown in the upper panel of Figure 3.16.

3.2.3 Eigenvectors

In the case of pulsars that exhibit quasi-periodic drifting, the primary eigenvector corresponding to the largest eigenvalue is substituted as the complex vector **P** in Equation 2.7 and used to describe the parameters of the elliptical path quasi-periodically traced by the Stokes polarisation vector in ***p***-space (Section 2.5.2). The lengths of the real and imaginary parts of **P** correspond to the semi-major (|**A**|) and semi-minor (|**B**|) axes of the ellipse, respectively. If the Stokes polarisation parameters (Stokes Q, U, and V) oscillate along a line, the length of **B** would be zero and |**A**| would be significant. Where |**A**| and |**B**| are almost equal, the elliptical path can be characterised as a near perfect circle and, if the energy of the quasi-periodic variations is significantly larger than that of the

white noise (both instrumental and intrinsic to the pulsar), then an oblate spheroidal distribution would be observed in ***p***-space. A prolate spheroidal distribution occurs when $|\mathbf{B}|$ is zero, and an ellipsoid arises as the length of **B** increases to a significant level.

Figure 3.18 shows how the shape of the elliptical path varies as a function of pulse longitude between a narrow ellipse and an approximate circle. Over the region of pulse longitude approximately between $90 \lesssim l \lesssim 100$, both lengths $|\mathbf{A}|$ and $|\mathbf{B}|$ are significant, which is consistent with the region roughly defined by $-5^\circ \lesssim \phi \lesssim 3^\circ$ over which Primak et al. (2022) discovered the unexpected toroidal distribution of the Stokes polarisation vector in ***p***-space. They also observe that the levels of the eigenvalues characterise a prolate spheroidal distribution at pulse longitudes $\phi \lesssim -5.4^\circ$. Similarly, we observe that the length of **A** is more significant than that of **B** at pulse longitudes preceding the moment where the semi-major and semi-minor axes are nearly equal, producing a peak in the axial ratio at $l \approx 79$ in the upper panel of Figure 3.18. This longitude precedes the transition between orthogonally polarised modes seen in the position angle (upper panel of Figure 3.1) and the transition between overlapping drift bands that are 180° out of phase (Figure 8 of Primak et al., 2022).

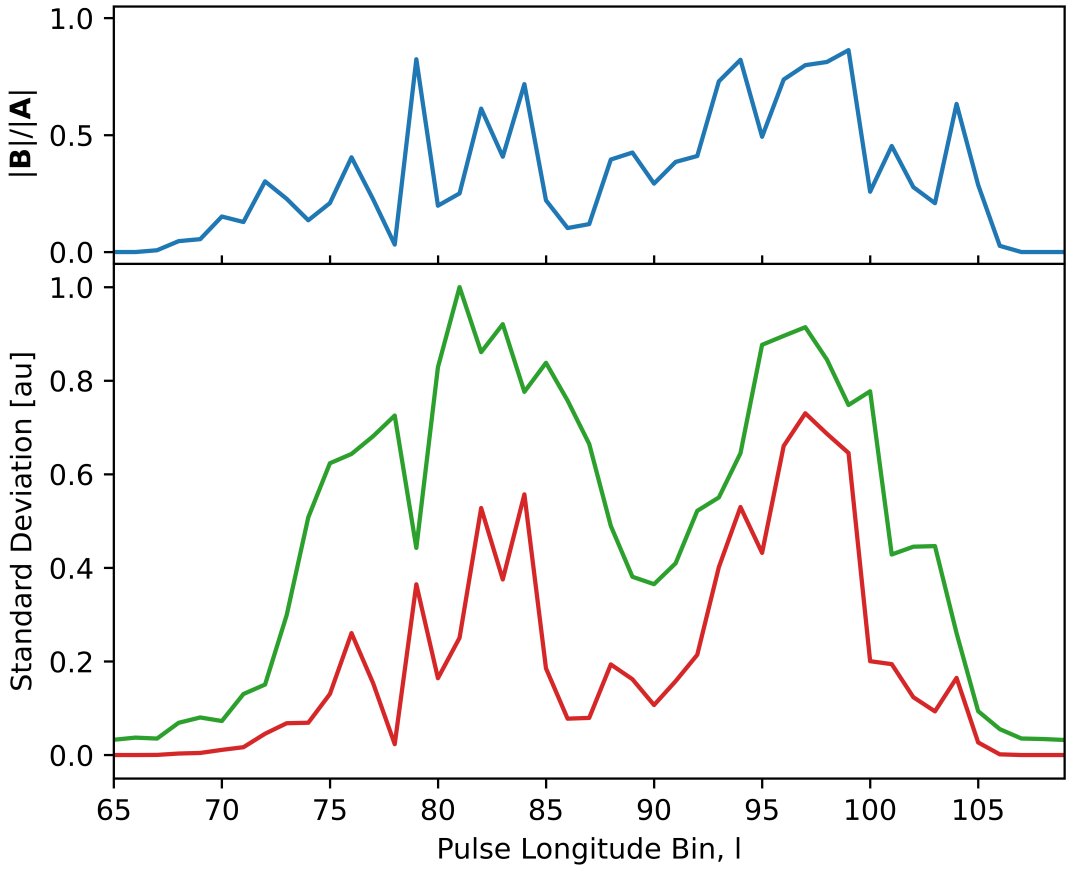

Figure 3.18: *Upper panel*: Axial ratio (blue solid line) is equal to $|\boldsymbol{B}|$ divided by $|\boldsymbol{A}|$. *Lower panel*: Fluctuations of the semi-major ($|\boldsymbol{A}|$; green solid line) and semi-minor ($|\boldsymbol{B}|$; red solid line) axes of the elliptical path about which the Stokes polarisation vector cycles quasi-periodically.

Computing the cross-product between the vectors **A** and **B** from Equation 2.7, multiplied by the square root of the eigenvalue, yields a 3-vector that is normal to the plane of the elliptical path. The normal describes the orientation of the ellipse in $\boldsymbol{p}$-space, and, if it is assumed that the polarisation states on the locus described by the ellipse are the result of a (partially) coherent superposition of orthogonally polarised modes, the normal to this ellipse describes the polarisation state of the natural modes as a function of pulse longitude. The polarisation state of the natural modes can be visualised by plotting the total linear polarisation $L = |\sqrt{\boldsymbol{c}_1^2 + \boldsymbol{c}_2^2}|$ and amount of circular polarisation $|\boldsymbol{c}_3|$, where c_i $(i = 1, 2, 3)$ denotes the elements of the normal vector and are treated as analogous to the three elements of the Stokes polarisation vector. Certain

pulse longitude bins, such as $l \approx 84$ and $l \approx 98$, exhibit a higher than expected level of circular polarisation while simultaneously the total linear polarisation is much less significant. Circularly polarised natural modes are unexpected because the natural modes of a relativistic plasma are expected to be highly linearly polarised (Kennett & Melrose, 1998).

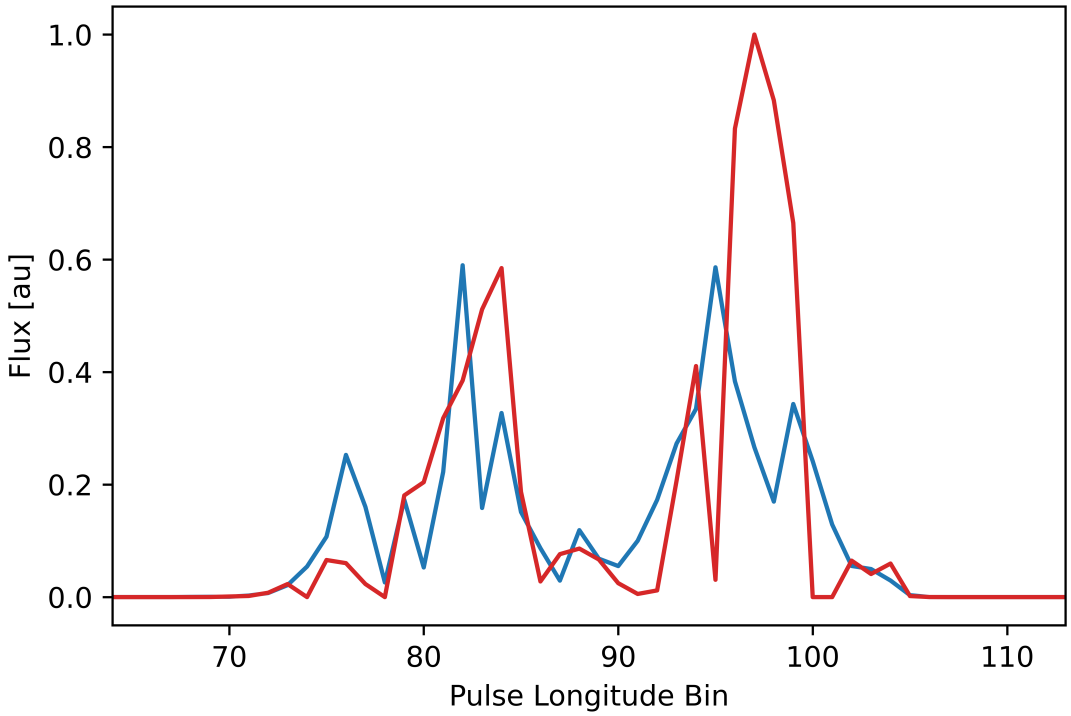

Figure 3.19: Cross-product of the real and imaginary axes of the primary eigenvector multiplied by the square root of the associated eigenvalue, where the blue solid line is the total linear polarisation, and the red solid line is the absolute value of circular polarisation.

Chapter 4

Interpretation and Discussion

The spectral analysis of the polarisation of drifting sub-pulses presented in this thesis takes much inspiration from previously published work, and uses it as a basis for exploring radio pulsar emission phenomena that currently are not well described by theory. Early studies of the periodic amplitude modulation in total intensity found well-defined features that are attributed to the drifting sub-pulses in the longitude-resolved fluctuation spectra (Backer, 1973). Our spectral analysis of the total intensity (Section 3.1.1) is consistent with the fundamental response observed by Backer (1973) for PSR B1919+21; furthermore, it is capable of providing more information on quasi-periodic fluctuations in both total intensity and polarisation.

As in the analysis of Edwards (2004), which is an extension and generalisation of the LRFS to fluctuations in the elements of the Stokes polarisation vector (polarisation longitude-resolved fluctuation spectrum; PLRFS), we perform a spectral analysis on the polarisation of the drifting sub-pulses. The PLRFS-based approach was demonstrated for only highly-periodic fluctuations in pulsars that exhibit coherent drifting signals (e.g. PSR B0809+74, PSR B0320+39, and PSR B0818−13), in which the fluctuation power in the LRFS and PLRFS is confined to a single harmonic bin. Generalisation of the PLRFS-based approach to pulsars that exhibit incoherent and quasi-periodic drifting

sub-pulses was offered as a suggestion, but not implemented before the research and development that was undertaken for this thesis. The signal of the pulsar on which we focus our attention, PSR B1919+21, is quasi-periodic: the fundamental response in the fluctuation spectra of the total intensity and polarisation is spread over a finite range of contiguous harmonic bins. It is clear in Figure 3.9 that the bandwidth and central frequency of the quasi-periodic signal vary as a function of time, in a way that is visually similar to the oblique drift-band modulation pattern. Previous studies (Backer, 1973; Lang, 1969; Rickett, 1970) of the variability of the drift period in PSR B1919+21 do not report on the quasi-periodic drifting of f_3. The method developed for this thesis has advanced the state of the art by making the spectral analysis of the polarisation of drifting sub-pulses applicable to a wider variety of sources; in particular, any quasi-periodic signal in which the fluctuation power is confined to a finite bandwidth of the fluctuation spectrum.

The PLRFS-based approach begins with the application of one-dimensional short-time Fourier transforms to the total intensity and polarisation signals at each pulse longitude, effectively decomposing them into their constituent frequencies as a function of time. For each pulse longitude and harmonic bin, there exists a time series of complex-valued Stokes polarisation vectors. The outer product of these vectors, averaged over time, yields the longitude-resolved polarisation fluctuation coherency matrix (PFCM) in each harmonic bin. The eigendecomposition of the PFCM, integrated over the full spectrum, describes the three-dimensional distribution of the Stokes polarisation vector in $\boldsymbol{p}$-space. The derivation of the polarisation statistics can, for the most part, be performed on pulsars that exhibit either coherent or incoherent drifting sub-pulses; however, it is not possible to obtain complete information about the distribution of quasi-periodic signals by utilising the methodology demonstrated by Edwards (2004). Due to their quasi-periodic nature, we cannot obtain the complex polarisation envelope that is formed by summing the coherent signal typically confined to a single coefficient from

each PLRFS, for each pulse longitude bin, after compensating them for an arbitrary, longitude-independent offset (Edwards & Stappers, 2003). In the case of sufficiently coherent signals, Edwards (2004) utilises the complex polarisation envelope as the complex vector $\boldsymbol{P}$ (Equation 2.7) that describes the geometric parameters of the elliptical path. For the signal of our pulsar that is spread over a number of harmonic bins, an alternative $\boldsymbol{P}$ is required to describe the ellipse's shape and orientation in $\boldsymbol{p}$-space. An appropriate substitute is determined as the primary eigenvector associated with the largest eigenvalue that characterises the process of the quasi-periodic cycling of the Stokes polarisation vector around the elliptical path. However, it can only be derived by implementing the methodology that was suggested by Edwards (2004) for the study of pulsars that exhibit quasi-periodic drifting sub-pulses. As a result, the methodology we carry out to study our pulsar PSR B1919+21 diverges after the one-dimensional Fourier transforms and requires a distinct and novel approach for the analysis of the polarisation statistics (Section 2.5.2).

4.1 Spectral Analysis of Quasi-Periodic Signals

Consider the spectral analysis demonstrated for the aforementioned three pulsars that exhibit highly-periodic drifting sub-pulses. Equation 2.8 is reduced to the limiting case of summing the spectral density tensor, computed from the outer product of the PLRFS, over all harmonic bins of the PLRFS. The result is a one-dimensional array of 3×3 real-valued covariance matrices that are equal to the real-valued covariance matrices computed by Primak et al. (2022) in the time domain. This is a consequence of Parseval's Theorem (see Section 3.2.1 for a full description). Eigendecomposition of the real-valued covariance matrix provides information on the three-dimensional distribution of the Stokes polarisation vector in $\boldsymbol{p}$-space. In particular, the distribution is characterised by the eigenvalues, which are the variance of the principal components.

Analogous to the findings in Primak et al. (2022), we also observe portions of the emission region in panel a of Figure 3.16 (or $\phi \approx -6.8^\circ$ in panel d of Figure 1 in Primak et al., 2022) that exhibit a prolate spheroidal distribution ($\sigma_1 > \sigma_2 = \sigma_3$), and a region of pulse longitude between $82 \lesssim l \lesssim 106$ (or $-5^\circ \lesssim \phi \lesssim 3^\circ$) that exhibits an unexpected and uncommon oblate spheroidal distribution ($\sigma_1 = \sigma_2 > \sigma_3$). The former is consistent with an incoherent superposition of orthogonally polarised modes, while the latter is inconsistent (van Straten & Tiburzi, 2017). A limitation of analysing the full spectrum is that it considers all periodic and non-periodic fluctuations. Thus, the three-dimensional distribution obtained in $\boldsymbol{p}$-space is, for the most part, an ellipsoidal cloud of white self-noise within which quasi-periodic or period processes are "buried".

The extension of the PLRFS-based approach is an analysis of finite ranges or subsets of the full spectrum, the result of which is a one-dimensional array of 3×3 complex-valued Hermitian coherency matrices (or polarisation fluctuation coherency matrices, PFCM). It enables one to obtain information on the fluctuations of the signal over the frequency range of interest. For example, we characterise the spectral noise from the off-signal regions and analyse the broad fundamental response of the quasi-periodic on-signal in isolation. The two subsets we identify in the fluctuation spectrum, on-signal and off-signal, were determined iteratively by utilising the subset classification algorithm developed for this thesis (Section 2.4). The lack of implementation in practice of the extension of the PLRFS-based approach meant that no algorithm existed for the detection of the finite bandwidth which confined the quasi-periodic signal in the fluctuation spectrum.

The modulation power of the off-signal polarisation fluctuations is insignificant and corresponds to the white self-noise of the pulsar that equally contributes to all harmonic bins of the fluctuation spectrum. On the other hand, the power of the on-signal amplitude fluctuations and how they differ from the spectral power of the off-signal subset is an instructive way of quantifying if the fluctuations are significant with respect to the

background level of white self-noise, or if they are negligible. This is an advantage of the extended methodology that is not possible to achieve in the analysis of the real-valued covariance matrices.

The eigendecomposition of the PFCM derived from the finite range of on-signal harmonic bins describes quasi-periodic processes that are present in the pulsar signal over the corresponding frequency range. Figure 3.17 displays a single significant eigenvalue over the whole emission region ($74 \lesssim l \lesssim 98$) that denotes one significant elliptical path that is cycled by the Stokes polarisation vector quasi-periodically. A second eigenvalue around pulse longitudes $99 \lesssim l \lesssim 102$ appears to be significant over all three of the (grey) eigenvalues derived from the off-signal range of harmonic bins, and could suggest that there is a second quasi-periodic process in $\boldsymbol{p}$-space. Over the rest of the on-pulse window, the second and third eigenvalues are nearly equal to the intensity of the two smallest off-signal eigenvalues and provide no evidence of other periodic processes present in the pulsar signal.

This is in contrast to the eigenvalues derived from the eigendecomposition of the real-valued covariance matrices which model the shape of the ellipsoidal cloud formed in $\boldsymbol{p}$-space. The analysis in the time domain implemented by Primak et al., (2022) cannot derive the dimensions of the elliptical path cycled by $\boldsymbol{p}$, rather, they can determine the shape of the cloud by the level of the eigenvalues as a function of pulse longitude. However, the cloud is primarily noise, so its dimensions do not necessarily characterise the periodic behaviour of the Stokes polarisation vector. The restriction to only the range of frequencies that contain significant spectral power reduces the level of white self-noise modelled in $\boldsymbol{p}$-space and allows for the geometric parameters of the elliptical path cycled by $\boldsymbol{p}$ to be described.

4.2 Drift-Synchronous Fluctuations of the Stokes Polarisation Vector

Evidence of the drift-synchronous relationship in PSR B1919+21, first discovered by Primak et al. (2022), is prevalent in the results of the spectral analysis in total intensity and polarisation (Section 3.1). The evidence is in the form of longitude-resolved (Figure 3.2) and time-resolved (Figure 3.9) fluctuation spectra of the Stokes parameters that all share a near-equal fundamental response and modulation pattern, which shows that the drifting sub-pulse pattern in total intensity is synchronised with the quasi-periodic cycling of the Stokes polarisation vector in $\boldsymbol{p}$-space. For approximately every 4.2 pulsar rotations: 1) sub-pulses will march through the pulse profile until a subsequent sub-pulse appears at the same pulse longitude as the previous sub-pulse. (They could be neighbouring sub-pulses or, in the case of spectral aliasing, separated by any integer number of sub-pulses); and 2) over certain regions of pulse longitude, the Stokes polarisation vector will complete one full revolution around an elliptical path in $\boldsymbol{p}$-space.

This drift-synchronous relationship is a rare phenomenon that has been observed in only three other pulsars: PSR B0320+39, PSR B0818−13, and in the trailing component of PSR B0809+74 (at 1380 MHz)(Edwards, 2004). Other pulsars, PSR B0809+74 (Taylor et al., 1971; Ramachandran et al., 2002; Ilie et al., 2020), PSR B1237+25 (Rankin & Ramachandran, 2003; Ilie et al., 2020), and PSR B0031−07 (Ilie et al., 2020), exhibit sharp switches of the polarisation state between orthogonally polarised modes as another form of drift-synchronous polarisation modulation. To explain their observations, Rankin and Ramachandran (2003) proposed an extension of the rotating carousel model in which adjacent beams have orthogonally polarised modes, possibly separated by birefringence. Edwards (2004) concluded that drift-synchronous cycling around elliptical paths are more complicated than this simple model can explain. With

only four known examples of this behaviour, the development of a more explanatory model would benefit from further observations of this phenomenon across a broader range of the pulsar population. The extent to which pulsars display periodic modulations of the Stokes parameters remains uncertain, and additional sources with similar characteristics might still be awaiting discovery. We discuss two possible interpretations of the PSR B1919+21 observations in Sections 4.3.2 and 4.4.

4.3 Elliptical Path in p-space

For each pulse longitude bin, the quasi-periodic cycling of the Stokes polarisation vector about an elliptical path systematically forms a three-dimensional distribution in $\boldsymbol{p}$-space as a function of pulse number. In other words, we obtain longitude-resolved distributions of $\boldsymbol{p}$ populated by the polarisation states of all pulses in a given pulse longitude. The eigenvalue derived from the on-signal subset of the full spectrum, that is significant over the whole pulse profile (Figure 3.17), denotes the presence of this quasi-periodic process in the signal. The geometric parameters of the elliptical path may be described by the real-valued orthogonal vectors $\boldsymbol{A}$ and $\boldsymbol{B}$ of any complex vector $\boldsymbol{P}$ (Equation 2.7; Edwards, 2004). (As an aside, the vectors need not be perfectly orthogonal to describe ellipses in $\boldsymbol{p}$-space; more importantly, the phase of any eigenvector $\boldsymbol{P}$ can be chosen such that $\boldsymbol{A}$ and $\boldsymbol{B}$ are orthogonal - see the Appendix B). The lengths $|\boldsymbol{A}|$ and $|\boldsymbol{B}|$ correspond to the semi-major and semi-minor axes of the ellipse, respectively, and we use them to describe its shape in terms of three cases: fluctuations of polarisation state are perfectly linear when the semi-minor axis is equal to zero ($|\boldsymbol{B}| = 0$); when one length is sufficiently greater than the other (i.e., $|\boldsymbol{A}| > |\boldsymbol{B}|$), the shape of the path is elliptical; and pulse longitude bins that display lengths that are equal ($|\boldsymbol{A}| = |\boldsymbol{B}|$) denote a perfectly circular path.

The shape of the ellipsoidal cloud formed by the systematic population of polarisation states in $\boldsymbol{p}$-space depends on the balance of spectral power between the quasi-periodic fluctuations (on-signal; Section 2.4.3) and the white self-noise (off-signal; Section 2.4.4) components of the SLRFS. In general, the cloud is mostly noise; its dimensions can be measured using the real-valued covariance matrix, which describes the combination of white self-noise and periodic drifting (Section 2.5.1). From the eigen-decomposition of the real-valued covariance matrix (Figure 3.16), a prolate spheroidal distribution is characterised by one single significant eigenvalue ($\sigma_1 > \sigma_2 = \sigma_3$), and two significant eigenvalues ($\sigma_1 \approx \sigma_2 > \sigma_3$) indicate an oblate spheroidal distribution. In the case of our pulsar, PSR B1919+21 is special in the sense that it exhibits a quasi-periodic component (owing to the elliptical cycling) that dominates the shape of the spheroidal distribution over most of the on-pulse window.

Figure 3.18 shows how the lengths of the elliptical path, and therefore the shape of the distribution in $\boldsymbol{p}$-space, vary as a function of pulse longitude. We observe evidence for a prolate spheroidal distribution throughout most of the on-pulse window, consistent with incoherent OPM superposition (van Straten & Tiburzi, 2017). Figure C.1 presents pulse longitude $l = 76$ that exhibits a distinct prolate spheroidal distribution of the Stokes polarisation vector (normalised by the total intensity). Our findings in the corresponding pulse longitudes are consistent with that of the uncommon toroidal distribution, as characterised by the shape of the elliptical path (Figure 3.18) and distribution of polarisation state in the scatter plots reproduced in Appendix C. An incoherent superposition of a single pair of orthogonally polarised natural modes will always produce a distribution consistent with a prolate spheroid (van Straten & Tiburzi, 2017), so it is unexpected to observe a distribution other than that. The prolate spheroidal distribution is common among radio pulsars; however, quasi-periodic cycling around a torus in $\boldsymbol{p}$-space requires explanation. The two possible models considered by Primak et al. (2022), Generalised Faraday Rotation and the Four-Mode Mixing model, are further

discussed and analysed in the following sections.

4.3.1 Generalised Faraday Rotation

It is plausible that generalised Faraday rotation (GFR) could explain the origin of the toroidal distribution (Primak et al., 2022). GFR is the (partially) phase-coherent superposition of arbitrarily and orthogonally polarised natural modes that produces a new polarisation state on the plane normal to the primary axis defined by the natural modes in $\boldsymbol{p}$-space. The position of this polarisation state on the normal plane can be described in terms of spherical coordinates: the radial distance from the origin depends on the amplitude and degree of polarisation of the natural modes and the degree of coherence between them; and the azimuthal angle is dependent on the phase relationship between the natural modes. For example, the coherent superposition of a pair of linearly polarised natural modes, Stokes Q and -Q, will produce a polarisation state that lies somewhere in the plane of Stokes U and V. A 0° or 180° phase shift between the modes will result in a perfectly linear polarisation state along the primary axis of Stokes U, and a phase shift of 90° or 270° will produce a right-handed or left-handed circular polarisation state (respectively) along the primary axis of Stokes V. All other possible phase shifts in between these special cases will place the polarisation state in one of the quadrants of the normal plane. We do not know the intrinsic degree of polarisation of the natural modes, so we assume that they are 100% polarised and have maximum length.

Given this interpretation, if the phase difference between the natural modes were to vary smoothly between 0° and 360° (2π) during one drift cycle, the new polarisation state will trace a circular path (assuming that the modes have equal amplitudes) in the normal plane. Over a large number of pulses of sufficiently high signal-to-noise ratio, the three-dimensional distribution formed by the population of the polarisation

states will manifest a toroidal distribution. In the absence of periodic cycling around an elliptical path, the phase variations during one drift cycle need not be smooth; that is, the polarisation states could populate the torus randomly instead of systematically. However, for PSR B1919+21, the polarisation state cycles around in synchrony with the period of the drifting sub-pulses (Section 4.2).

Figure 3.19 shows the magnitudes of the circular and linear polarisation of the natural modes as a function of pulse longitude. Kennett and Melrose (1998) predicted that the natural modes of a highly-relativistic plasma, such as that expected in the pulsar magnetosphere, should be strictly or highly linearly polarised; however, we observe unexpected levels of circular polarisation at certain pulse longitudes. The results are counter-intuitive and pose a challenge to accepting GFR as a plausible explanation for the toroidal distribution.

4.3.2 Four-Mode Mixing Model

Formation of the torus in $\boldsymbol{p}$-space could also be formed through an incoherent superposition of more than one pair of orthogonally polarised natural modes. In this section, we argue that the four-mode mixing model proposed by Primak et al. (2022) more readily explains the origin of the toroidal distribution than generalised Faraday rotation. The model requires an incoherent superposition of two pairs of orthogonally polarised natural modes (as opposed to the coherent superposition of four modes considered by Dyks et al., 2021). The two OPM pairs originate from different emission regions and define axes in $\boldsymbol{p}$-space that are orthogonal to each other. (There exists the possibility that they could also be non-orthogonal, since an ellipse with non-orthogonal axes cannot be differentiated from an ellipse with orthogonal axes). In a similar way to the natural modes that oscillate on the plane of the electric field perpendicular to the direction of propagation, the two OPM pairs quasi-periodically oscillate along their respective

primary axes. If the modulations of the OPM pairs are approximately 90° or 270° out of phase with respect to each other, the resulting polarisation state of their incoherent superposition will cycle about an ellipse as a function of pulse number and populate a three-dimensional distribution in the shape of a torus.

Four-mode mixing can explain several anomalous phenomena presented in Chapter 3. These include the presence and absence of the second drift harmonic feature in the LRFS and PLRFS (Section 3.1.1), quasi-periodic fluctuations of polarisation state where there is no evidence of drifting in total intensity (Section 3.1.2), or the apparent beat frequency produced by the interference between two modulating components (Section 3.1.4). Firstly, the second harmonic of the drift frequency (A.K.A. "$P_3 = 2P_0$ flickering"; Weltevrede et al., 2007) appears in the LRFS and PLRFS at several pulse longitudes (Section 3.1.2). With the four-mode mixing model, we are able to justify the presence of the second harmonic features, and also their absence in other regions of the pulse profile, in terms of the ratio between the sub-beam width and sub-beam separation and the amplitudes of the orthogonally polarised natural modes.

Presented in Appendix D is a simulation of the incoherent superposition of modes in total intensity and polarisation, where the variables are the separation between sub-beams and amplitude of the modes. The simulation allows us to describe some of the observational properties of the drift period in the slices of the LRFS and PLRFS (Section 3.1.2), such as: the presence of a significant fundamental response and double-frequency feature in total intensity; fluctuations in polarisation while there are little to none in total intensity; and the absence of double-frequency features in total intensity where the fundamental response of the quasi-periodic signal remains.

Fluctuations in total intensity can be doubled by the incoherent superposition of a pair of OPMs, where the natural modes are 180° out of phase and the sub-beam width-to-separation ratio is sufficiently small, i.e., the sub-beams are resolved (panel a of Figure D.1). Oscillations of the modes in total intensity are positive, and so during

one drift cycle there will be two peaks of the total intensity. In the same period, one of the two modes in polarisation is negative, and their incoherent superposition (while being 180° out of phase) will cycle through one maximum. The second harmonic in total intensity appears primarily in the leading component of the pulse profile, between pulse longitudes $78 \lesssim l \lesssim 81$, where two drift bands overlap 180 degrees out of phase with each other.

We also observe consecutive harmonic bins at high frequencies that appear to be above the white spectral power of the total intensity in the region of the trailing component where the toroidal distribution occurs. Here, the fundamental response of the total intensity is absent, which can be explained by matched mode intensities. In this case, the maximum intensities of the pairs are equal and the minimum intensities of the pairs are equal.

Significant weakening, or complete absence, of all periodic features in the fluctuation spectrum of the total intensity, including doubled-modulations, would require that the sub-beam width-to-separation ratio is sufficiently large such that the sub-beams are only partially resolved or unresolved (respectively). Panel b of Figure D.3 of the double-modulation simulation demonstrates this case when the parameter for the sub-beam separation is decreased. Total intensity modulations weaken as sub-beams become less resolved, while modulations in polarisation remain sufficiently significant. Periodicity exclusive to polarisation is observed over the region of pulse longitude that exhibits the torus of polarisation state in $\boldsymbol{p}$-space ($94 \lesssim l \lesssim 98$; Section 3.1.2).

In the fluctuation spectra of pulse longitude bins $l \approx 83$ and $100 \lesssim l \lesssim 102$, the total intensity exhibits a fundamental response, but the periodic feature at double the frequency is not present. If we attribute the absence of the second harmonic feature to unresolved sub-beams, there should also be an absence of all other features in the fluctuation spectrum of the total intensity. In order to explain this case, we consider the fact that the amplitudes of the modes of the OPM pair need not be equal. As in the

simulation of double-modulations (Figure D.4), if the amplitude of mode A is larger than that of mode B (and they are 180° out of phase with respect to each other), and the sub-beams have a sufficiently large width-to-separation ratio, the incoherent superposition of the intensities of the modes would result in only the fundamental response, and only the doubled modulations would be unresolved. In a single rotating carousel composed of alternating orthogonally polarised sub-beams (Rankin & Ramachandran, 2003), modes with unequal amplitudes can be obtained in the case when the line of sight passes through the centre of mode A (i.e., its peak) and through the minima or off-centre of mode B, making it appear dimmer than mode A.

As reported in Sections 3.1.1 and 3.1.2, there are hints of a second drift harmonic in the longitude-resolved fluctuation spectra of Stokes Q and U around pulse longitudes $99 \lesssim l \lesssim 101$. We speculate that supporting evidence for the significance of these features is in the form of a second on-signal eigenvalue that exhibits statistical significance over all three off-signal (grey) eigenvalues in the corresponding pulse longitude bins (Section 3.2.2). The on-signal subset of the full spectrum and the quasi-periodic fluctuations that it confines could be investigated further to find the origin of the second drift harmonic in polarisation.

4.4 Two-Carousel System

In the rotating carousel model, sub-beams are split owing to the birefringent nature of the pulsar magnetosphere (Rankin et al., 2006), resulting in two spatially-separated beams that have orthogonally polarised modes. Rotation of the carousel and simultaneous sweep of the radio emission beam under our line of sight periodically alternates the polarisation state between a pair of OPMs. The origin of the four-modes discussed above can be interpreted as the OPMs of a two-carousel system in which each OPM pair belongs to a distinct rotating carousel. Thus, the toroidal distribution of polarisation

state would arise from the incoherent superposition of the two rotating carousels when they are superposed and 90° out of phase with respect to each other. Observational properties derived from the spectral analysis performed in this thesis lend credence to this concept.

Consider the decomposition of the LRFS and PLRFS into the time-resolved fluctuation spectra presented in Section 3.1.3. The drift-period varies almost, but not quite, systematically as a function of time, and its modulation pattern consists of long-period variations. The long-period variations in all Stokes parameters may be a form of quasi-periodic beating that results from the interference of two modulating carousels. Each carousel gives rise to the observed quasi-periodic sub-pulse drifting within the on-signal range of harmonic bins ($0.2 \lesssim f_3 \lesssim 0.25$; Figure 3.9). Where the spectral power of those harmonic bins oscillates with a frequency equal to the difference in the frequencies of the component carousels. Given that the two OPM pairs oscillate quasi-periodically, it is plausible that each rotating carousel can have a slightly different rotational frequency and produce the beating modulation pattern observed in the fluctuation spectra. Two different rotational frequencies of a two-carousel system potentially could be explained by a theoretical model that relates the (magnetic) latitudinal separation between each carousel to the difference in rotational frequency; however, such a model would also require an accurate description of the beam geometry, which has proven difficult to date (Primak et al., 2022).

4.5 Next Steps

The spectral analysis of the polarisation of drifting sub-pulses has yielded a rich variety of novel results, and there exists the possibility to discover more than what is reported in this thesis.

Section 3.1.2 reveals quasi-periodic features of the pulsar signal at low frequencies

and at double the frequency of the fundamental response in the fluctuation spectra of the total intensity and polarisation. To statistically quantify the significance of the series of contiguous harmonic bins that form these spectral features, we propose to compute the standard deviation and mean of the off-signal subset of the full spectrum only, and set the threshold to three times the standard deviation above the mean. Unlike the approach we take in Section 2.4, where the threshold is set to three times the MADM above the median, there are no obvious outliers (for example, owing to the on-signal range) and we can obtain a local estimate of the white self-noise. Determining the statistical significance of the double-frequency feature would provide confidence in our interpretation of its presence and absence in terms of the four-mode mixing model (Section 4.3.2) and two-carousel system (Section 4.4).

The ellipsoidal cloud in $\boldsymbol{p}$-space is mostly influenced by the spectral power of the white self-noise, and its dimensions can be measured only by the real-valued covariance matrix that describes all of the periodic and non-periodic fluctuations in the full spectrum. The elliptical cycling of the Stokes polarisation vector is "buried" within this cloud of noise; uncovering the distribution of only the quasi-periodic components of the LRFS and PLRFS would make it more consistent with the shape of the elliptical path, and would provide more information on the polarisation state of the natural modes, the origin of the torus, and the origin of the double-frequency features in polarisation. To achieve this, for every pulse longitude bin, the average of the off-signal harmonic bins would be subtracted from the spectral power of the finite on-signal bandwidth to remove biases owing to the pulsar's white self-noise. Then, performing an inverse Fourier transform on the resultant would revert the signal to the time domain where the polarisation states from all pulses in a given pulse longitude can be plotted in $\boldsymbol{p}$-space.

The observations of PSR B1919+21 analysed in this thesis are taken at a central frequency of 1414 MHz over a bandwidth of only 20 MHz. Studying the way in which the observational findings, such as the elliptical cycling of the Stokes polarisation vector

in $\boldsymbol{p}$-space, evolve with radio frequency may provide more information and help us to differentiate between the different models we consider. For example, GFR is expected to vary strongly with radio wavelength; e.g., with observable effects proportional to λ^3 (Kumar et al., 2023). In contrast, the refraction of the beams involved in four-mode mixing can be expected to vary much more slowly with radio wavelength; e.g., on a wavelength scale typical of profile shape evolution. Proposed models for the spectral dependence of partial-coherence (Gangadhara, 1997; Dyks et al., 2021; Oswald et al., 2023) and refractive/polarisation properties of the pulsar magnetosphere (von Hoensbroech et al., 1998; Petrova & Lyubarskii, 2000) could be tested using our extension of the PLRFS-based approach to gain a better understanding of the radio emission mechanism and propagation through the pulsar magnetosphere.

Studies of single-pulse variability are typically limited to pulsars that are sufficiently bright such that their individual pulses may be resolved (van Straten & Tiburzi, 2017). Most of the pulsars in the wider population are too faint, and novel statistical methods are required to interpret their average pulse profiles. To this end, the extension of the PLRFS-based approach developed for this thesis will be generalised and applied to other bright radio pulsars from which statistically significant descriptions can be obtained and applied to the general pulsar population. This will open opportunities to quantify the prevalence of anomalous phenomena observed in rare cases, such as the toroidal distribution of polarisation state, drift-synchronous cycling of the Stokes polarisation vector, and periodicity that is exclusive to polarisation.

Chapter 5

Conclusion

Pulsars, the cosmic lighthouses of our Universe and some of the most extreme natural laboratories of physics, are mysterious objects that, despite over five decades of research, remain only partially understood.

For this thesis, we extended the work of Edwards (2004) such that the PLRFS-based approach can be applied to a quasi-periodic signal in which the fluctuation power is confined to a finite bandwidth of the fluctuation spectrum, progressing beyond the study of only pulsars that exhibit highly-coherent drifting.

The Stokes longitude-resolved fluctuation spectra reveal a synchronicity between the Stokes polarisation vector that cycles about an elliptical path in $\boldsymbol{p}$-space and the period-varying drifting sub-pulses. This drift-synchronous phenomenon has been observed in only three other pulsars (Edwards, 2004); however, PSR B1919+21 stands out as it was found that the polarisation state forms a toroidal distribution in $\boldsymbol{p}$-space over a narrow region in the trailing component of the pulse profile (Primak et al., 2022). Over a similar range of pulse longitudes, we observe that there is a decrease in periodic fluctuations in total intensity while fluctuations in polarisation remain significant. Drifting in only polarisation, and not in total intensity, has been observed only once before and is much more clearly evident when using spectral techniques like those developed in this thesis.

We discovered that for PSR B1919+21 the drift period of the drifting sub-pulses varies quasi-periodically with peaks in total intensity and polarisation occurring over long-periods. Generalisation of our method to a broader range of radio pulsars (that are faint and/or exhibit quasi-periodic variations) will allow us to quantify the prevalence of rare and anomalous phenomena among the wider pulsar population.

The results derived from the spectral analysis were used to consider models, including generalised Faraday rotation and four-mode mixing, for the origin of the toroidal distribution of polarisation state and drift-synchronous phenomenon. We conclude that four-mode mixing is more readily able to explain more of the observable properties of the radio signal than generalised Faraday rotation, such as the second-harmonic features and apparent beat frequency produced by the interference between two modulating pairs of OPMs. Our proposed two-carousel model provides a plausible explanation for the origins of both the four modes and the apparent beat frequency between them. Further observations across a wide range of the pulsar population and over a broad spectrum of radio frequencies may help to better illuminate this picture.

References

Abdo, A. A., Ackermann, M., Ajello, M., Atwood, W. B., Axelsson, M., Baldini, L., ... Barbiellini, e., G. (2010, April). The First Fermi Large Area Telescope Catalog of Gamma-ray Pulsars. *ApJS*, *187*, 460-494. doi: 10.1088/0067-0049/187/2/460

Allen, M. & Melrose, D. (1982). Elliptically Polarized Natural Modes in Pulsar Magnetospheres. *PASA*, *4*, 365.

Armstrong, J. W., Rickett, B. J. & Spangler, S. R. (1995). Electron density power spectrum in the local interstellar medium. *ApJ*, *443*, 209-221.

Arons, J. & Barnard, J. J. (1986). Wave propagation in pulsar magnetospheres:dispersion relations and normal modes of plasmas in superstrong magnetic fields. *ApJ*, *302*, 120.

Baade, W. & Zwicky, F. (1934). Cosmic rays from super-novae. *Proc. Nat. Acad. Sci.*, *20*, 259-263.

Backer, D. C. (1970). Peculiar pulse burst in PSR 1237+25. *Nature*, *228*, 1297-1298.

Backer, D. C. (1973). Pulsar fluctuation spectra and the generalized drifting-subpulse phenomenon. *ApJ*, *182*, 245.

Backer, D. C., Rankin, J. M. & Campbell, D. B. (1976, September). Orthogonal mode emission in geometric models of pulsar polarisation. *Nature*, *263*, 202-207.

Bhat, N. D. R., Rao, A. P. & Gupta, Y. (1999). Long-term scintillation studies of pulsars. i. observations and basic results. *ApJS*, *121*, 483-513.

Carozzi, T., Karlsson, R. & Bergman, J. (2000). Parameters characterizing electromagnetic wave polarization. *Physical Review E*, *61*, 2.

Chugunov, Y. V., Eidman, V. I. & Suvorov, E. V. (1975, January). The motion of charged particles in a strong electromagnetic field and curvature radiation. *Astrophysics and Space Science*, *32*, L7-L10. doi: 10.1007/BF00646233

Cocke, J. (1973). Stimulated linear acceleration radiation: A pulsar radio emission mechanism. *ApJ*, *184*, 291-300.

Cordes, J. M. (1986). Space velocities of radio pulsars from interstellar scintillations. *ApJ*, *311*, 183-196.

Deller, A. T., Tingay, S. J., Bailes, M. & Reynolds, J. E. (2009, August). Precision Southern Hemisphere VLBI Pulsar Astrometry. II. Measurement of Seven Parallaxes. *ApJ*, *701*, 1243-1257. doi: 10.1088/0004-637X/701/2/1243

Demorest, P. B., Pennucci, T., Ransom, S. M., Roberts, M. S. E. & Hessels, J. W. T. (2010, October). A two-solar-mass neutron star measured using Shapiro delay. *Nature*, *467*, 1081-1083. doi: 10.1038/nature09466

Dennis, M. R. (2004). Geomteric interpretation of the three-dimensional coherence matrix for nonparaxial polarization. *Journal of Optics A: Pure and Applied Optics*, *6*, S26-S31.

Drake, F. D. & Craft, H. D. (1968). Second periodic pulsations in pulsars. *Nature*, *220*, 231-235.

Dyks, J., Weltevrede, P. & Ilie, C. (2021, February). Circular polarization in radio pulsar PSR B1451-68: coherent mode transitions and intrabeam interference. *MNRAS*, *501*(2), 2156-2173. doi: 10.1093/mnras/staa3762

Edwards, R. T. (2004, November). The polarization of drifting subpulses. *A&A*, *426*, 677-686.

Edwards, R. T. & Stappers, B. W. (2003). Pulse-to-pulse intensity modulation and drifting subpulses in recycled pulsars. *A&A*, *407*, 273-287.

Edwards, R. T. & Stappers, B. W. (2004). Ellipticity and deviations from orthogonality in the polarization modes of PSR B0329+54. *A&A*, *421*, 681-691.

Edwards, R. T., Stappers, B. W. & van Leeuwen, A. G. J. (2003). Unusual subpulse modulation in PSR B0320+39. *A&A*, *402*, 321-329.

Ekers, R. D. & Moffet, A. T. (1969, October). Polarization of Pulsating Radio Sources. *ApJ*, *158*, L1. doi: 10.1086/180419

Gangadhara, R. (1997). Orthogonal polarization mode phenomenon in pulsars. *A&A*, *327*, 155.

Gold, T. (1968). Rotating neutron stars as the origin of the pulsating radio sources. *Nature*, *218*, 731-732.

Goldreich, P. & Julian, W. H. (1969). Pulsar electrodynamics. *ApJ*, *157*, 869-880.

Hankins, T. H. & Rankin, J. M. (2010, January). Arecibo Multi-Frequency Time-Aligned Pulsar Average-Profile and Polarization Database. *AJ*, *139*, 168-175. doi: 10.1088/0004-6256/139/1/168

Heger, A., Fryer, C. L., Woosley, S. E., Langer, N. & Hartmann, D. H. (2003). How massive single stars end their life. *ApJ*, *591*, 288-300.

Hewish, A., Bell, S. J., Pilkington, J. D. H., Scott, P. F. & Collins, R. A. (1968). Observation of a rapidly pulsating radio source. *Nature*, *217*, 709-713.

Hotan, A. W., van Straten, W. & Manchester, R. N. (2004). PSRCHIVE and PSRFITS: An Open Approach to Radio Pulsar Data Storage and Analysis. *PASA*, *21*, 302-309.

Ilie, C. D., Weltevrede, P., Johnston, S. & Chen, T. (2020, January). The drifting sub-pulses of PSR B0031-07 and its synchronously modulated radio polarization. *mnras*, *491*(3), 3385-3394. doi: 10.1093/mnras/stz3167

Johnston, S., Kramer, M., Karastergiou, A., Keith, M. J., Oswald, L. S., Parthasarathy, A. & Weltevrede, P. (2022, December). The Thousand-Pulsar-Array programme on MeerKAT XI: Application of the rotating vector model. *MNRAS*, *000*, 1-9. doi: 10.1093/mnras/stac3636

Kennett, M. & Melrose, D. (1998). Propagation-induced circular polarisation in synchrotron sources. *PASA*, *15*, 211-216.

Kramer, M., Stairs, I. H., Manchester, R. N., McLaughlin, M. A., Lyne, A. G., Ferdman, R. D., ... Camilo, F. (2006, October). Tests of General Relativity from Timing

the Double Pulsar. *Science*, *314*, 97-102. doi: 10.1126/science.1132305

Kroll, N. & McMullin, W. (1979). Stimulated linear acceleration bremsstrahlung. *ApJ*, *231*, 425.

Kumar, P., Shannon, R. M., Lower, M. E., Deller, A. T. & Prochaska, J. X. (2023, August). Propagation of a fast radio burst through a birefringent relativistc plasma. *Physical Review D*, *108*. doi: 10.1103/PhysRevD.108.043009

Lang, K. R. (1969). Periodic Variations in Pulsar Radiation Intensity. *ApJ*, *158*, L175.

Lyutikov, M. (2002). Radio emission from magnetars. *ApJ*, *580*, L65.

Manchester, R. N., Taylor, J. H. & Huguenin, G. R. (1975). Observations of pulsar radio emission II. Polarisation of individual radio pulses. *ApJ*, *196*, 83-102.

McKinnon, M. M. (2002). Statistical Modeling of the Circular Polarization in Pulsar Radio Emission and Detection Statistics of Radio Polarimetry. *ApJ*, *568*, 302-311.

McKinnon, M. M. (2004). On the Excess Dispersion in the Polarization Position Angle of Pulsar Radio Emission. *ApJ*, *606*, 1154-1166.

McKinnon, M. M. & Stinebring, D. R. (2000). The Mode-separated Pulse Profiles of Pulsar Radio Emission. *ApJ*, *529*, 435–446.

Melrose, D. B. (1978). Amplified linear acceleration emission applied to pulsars. *ApJ*, *225*, 557-573.

Melrose, D. B. (1979). Propagation effects on the polarization of pulsar radio emission. *Aust. J. Phys.*, *32*, 61-70.

Melrose, D. B. (2017, July). Coherent emission Mechanisms in Astrophysical Plasmas. *Reviews of Modern Plasma Physics*, *1*, 5. doi: 10.1007/s41614-017-0007-0

Melrose, D. B. & Gedalin, M. E. (1999). Relativistic plasma emission and pulsar radio emission: A critique. *ApJ*, *521*, 351–361.

Melrose, D. B., Gedalin, M. E., Kennett, M. P. & Fletcher, C. S. (1999, August). Dispersion in an intrinsically relativistic, one-dimensional, strongly magnetized pair plasma. *Journal of Plasma Physics*, *62*, 233-248. doi: 10.1017/S0022377899007795

Melrose, D. B. & Yuen, R. (2016, Apr). Pulsar electrodynamics: an unsolved problem. *Journal of Plasma Physics*, *82*(2), 635820202. doi: 10.1017/S0022377816000398

Oswald, L. S., Karastergiou, A. & Johnston, S. (2023). Pulsar polarization: a partial-coherence model. *MNRAS*, *525*, 840-853.

Pacini, F. (1968). Rotating neutron stars, pulsars, and supernova remnants. *Nature*, *219*, 145-146.

Petrova, S. A. (2001). On the origin of orthogonal polarization modes in pulsar radio emission. *A&A*, *378*, 883-897.

Petrova, S. A. & Lyubarskii, Y. E. (2000, March). Propagation effects in pulsar magnetospheres. *A&A*, *355*, 1168–1180.

Primak, N., Tiburzi, C., van Straten, W., Dyks, J. & Gulyaev, S. (2022, October). The polarization of the drifting sub-pulses from PSR B1919+21. *A&A*, *657*, 14.

Prószyński, M. & Wolszczan, A. (1986). A cross-correlation analysis of subpulse drift in PSR 0809+74, PSR 1237+25 and PSR 1919+21. *ApJ*, *307*, 540-544.

Radhakrishnan, V. & Cooke, D. J. (1969). Magnetic poles and the polarization structure of pulsar radiation. *Astrophys. Lett.*, *3*, 225-229.

Ramachandran, R., Rankin, J. M., Stappers, B. W., Kouwenhoven, M. L. A. & van Leeuwen, A. G. J. (2002). Pulsar "drifting"-subpulse polarization: No evidence for systematic polarization-angle rotations. *A&A*, *381*, 993-999.

Rankin, J. M. & Ramachandran, R. (2003). Toward an Empirical Theory of Pulsar Emission. VIII. Subbeam Circulation and the Polarization-Modal Structure of Conal Beams. *ApJ*, *590*, 411-423.

Rankin, J. M., Ramachandran, R., van Leeuwen, J. & Suleymanova, S. A. (2006, August). Phenomenology of pulsar B0809+74's rotating subbeam system. II. "Carousel" configuration and polarization. *A&A*, *455*(1), 215-221. doi: 10.1051/0004-6361:20054417

Rickett, B. J. (1970). Interstellar scintillation and pulsar intensity variations. *MNRAS*, *150*, 67–91.

Ruderman, M. A. & Sutherland, P. G. (1975). Theory of pulsars: Polar gaps, sparks, and coherent microwave radiation. *ApJ*, *196*, 51-72.

Samson, J. C. (1973). Descriptions of the polarization states of vector processes: Applications to ulf magnetic fields. *Geophys. J. R. astr. Soc.*, *34*, 403-419.

Song, X., Weltevrede, P., Szary, A., Wright, G., Keith, M. J., Basu, A., ... Serylak, M. (2023, January). The Thousand-Pulsar-Array programme on MeerKAT - VIII. The subpulse modulation of 1198 pulsars. *MNRAS*, *000*, 1-78. doi: 10.1093/mnras/stad135

Staelin, D. H., Ewing, M. S., Price, R. M. & Sutton, J. M. (1970). Slow periodic variations in pulsars. *ApJ*, *160*, L7-L10.

Stinebring, D. R., Cordes, J. M., Rankin, J. M., Weisberg, J. M. & Boriakoff, V. (1984). Pulsar polarization fluctuations. I. 1408 MHz statistical summaries. *ApJS*, *55*, 247-277.

Taylor, J. H., Huguenin, G. R., Hirsch, R. M. & Manchester, R. N. (1971). Polarisation of the drifting subpulses of pulsar 0809+74. *Astrophys. Lett.*, *9*, 205-208.

Taylor, J. H., Manchester, R. N. & Huguenin, G. R. (1975). Observations of pulsar radio emission. I. Total–intensity measurements of individual pulses. *ApJ*, *195*, 513.

Usov, V. V. (2000). Radiating Regions in Pulsar Magnetospheres: From Theory to Observations and Back. *Pulsar Astronomy - 2000 and Beyond*, *202*, 417-420. doi: 10.48550/arXiv.astro-ph/9911403

van Straten, W. (2009, April). The Statistics of Radio Astronomical Polarimetry: Bright Sources and High Time Resolution. *ApJ*, *694*, 1413-1422. doi: 10.1088/0004-637X/694/2/1413

van Straten, W. & Tiburzi, C. (2017, February). The Statistics of Radio Astronomical Polarimetry: Disjoint, Superposed, and Composite Samples. *ApJ*, *835*, 293. doi: 10.3847/1538-4357/835/2/293

van Straten, W., Demorest, P. & Osłowski, S. (2012, July). Pulsar data analysis with PSRCHIVE. *Astronomical Research and Technology*, *9*(3), 237–256.

von Hoensbroech, A., Lesch, H. & Kunzl, T. (1998). Natural polarization modes in pulsar magnetospheres. *A&A*, *336*, 209-219.

Weltevrede, P., Stappers, B. W. & Edwards, R. T. (2007, July). The subpulse modulation properties of pulsars at 92 cm and the frequency dependence of subpulse modulation. *A&A*, *469*, 607-631. doi: 10.1051/0004-6361:20066855

Weltevrede, P., Stappers, B. W., van den Horn, L. J. & Edwards, R. T. (2003, September). Refraction in a pulsar magnetosphere - the effect of a variable emission height on pulse morphology. *A&A*, *412*, 473-479. doi: 10.1051/0004-6361:20031461

Wolszczan, A. & Frail, D. A. (1992). A planetary system around the millisecond pulsar PSR 1257+12. *Nature*, *355*, 145-147.

Appendix A

On-Pulse Subset Classification Flowchart

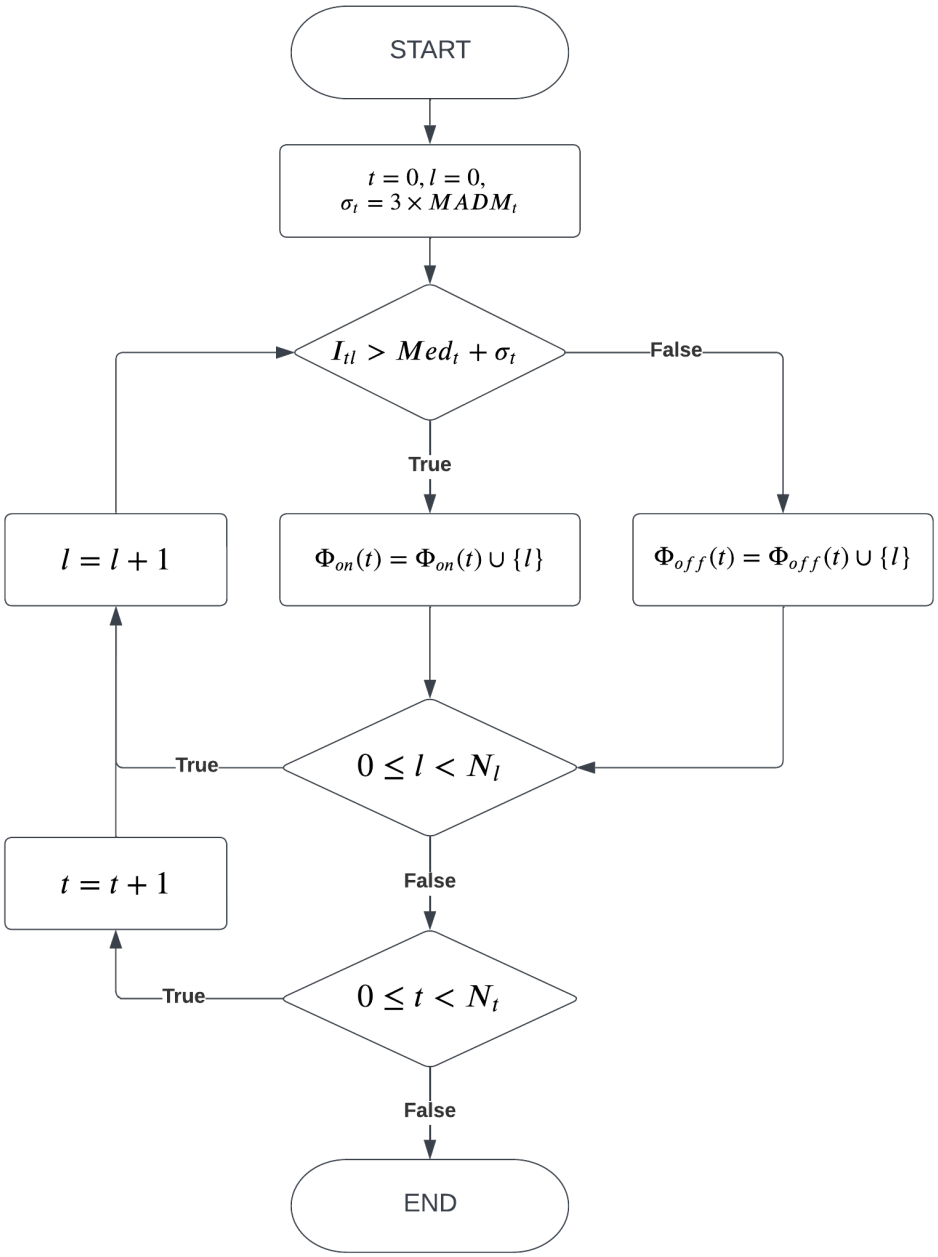

Figure A.1: Flowchart for the classification and detection of the on-pulse window, where t is pulse number and l is pulse longitude. MADM_t is the median absolute deviation from the median (see Section 2.4), and Med_t is the median, of the total intensity, I_{tl}, of each pulse. Φ_{on} and Φ_{off} denote the subsets of the pulse longitude bins that correspond to the on-pulse and off-pulse regions, respectively, and the union with the pulse longitude of a given pulse denotes the appendage of it to the appropriate subset of Φ. N_l and N_t denote the total number of pulse longitude bins in each pulse and pulses in the dataset, respectively.

Appendix B

Complex Phase of an Ellipse

The following derivation has been provided by A. Prof. W. van Straten:
Consider a complex-valued vector, $\boldsymbol{P} = \boldsymbol{A} + i\boldsymbol{B}$, where $\boldsymbol{A} = \mathrm{Re}(\boldsymbol{P})$ and $\boldsymbol{B} = \mathrm{Im}(\boldsymbol{P})$ are the (real-valued) real and imaginary parts of $\boldsymbol{P}$. In general, $\boldsymbol{A}$ and $\boldsymbol{B}$ are not perpendicular. To describe the ellipse drawn by $\mathrm{Re}(\boldsymbol{P}e^{i\omega t})$ we seek the vector in which $\boldsymbol{A}$ and $\boldsymbol{B}$ are perpendicular and oriented along the semi-major and semi-minor axes of the ellipse, respectively. To find such a vector, first note that

$$\boldsymbol{P} \cdot \boldsymbol{P} = |\boldsymbol{A}|^2 - |\boldsymbol{B}|^2 + i2\boldsymbol{A} \cdot \boldsymbol{B}; \tag{B.1}$$

therefore, if $\boldsymbol{A}$ and $\boldsymbol{B}$ are perpendicular, then $\boldsymbol{P} \cdot \boldsymbol{P}$ is real-valued. Furthermore, if $\boldsymbol{P} \cdot \boldsymbol{P} > 0$, then $|\boldsymbol{A}| > |\boldsymbol{B}|$, in which case $|\boldsymbol{A}|$ is the length of the semi-major axis and $|\boldsymbol{B}|$ is the length of the semi-minor axis. Second, note that if $\boldsymbol{P}$ is an eigenvector, then $\boldsymbol{P'} = e^{i\phi}\boldsymbol{P}$ is also an eigenvector (with the same length); therefore, we seek ϕ such that

$$\boldsymbol{P'} \cdot \boldsymbol{P'} = e^{i2\phi}\boldsymbol{P} \cdot \boldsymbol{P} \tag{B.2}$$

is real-valued and positive. This is satisfied when 2ϕ is equal and opposite to the phase of $\boldsymbol{P} \cdot \boldsymbol{P}$; i.e.

$$\phi = -\frac{1}{2} \tan^{-1} \frac{2\boldsymbol{A} \cdot \boldsymbol{B}}{|\boldsymbol{A}|^2 - |\boldsymbol{B}|^2} \tag{B.3}$$

Appendix C

Scatter Plots of Polarisation State

As in Primak et al. (2022), for a given pulse longitude bin, scatter plots of the three-dimensional normalised Stokes polarisation vector, $(Q, U, V)/I$, are used to visualise the distribution of polarisation state as a function of pulse number in the following figures.

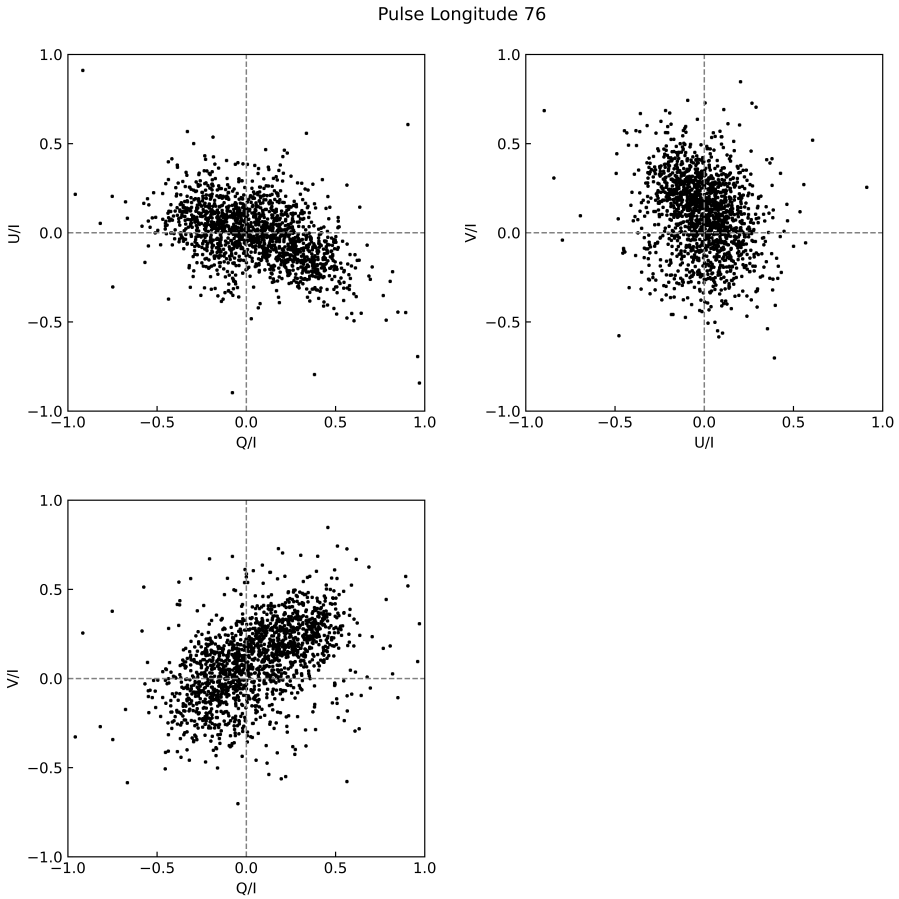

Figure C.1: Common prolate spheroidal distribution of the Stokes polarisation vector at pulse longitude l = 76, presented as two-dimensional projections onto the major planes of $\boldsymbol{p}$-space.

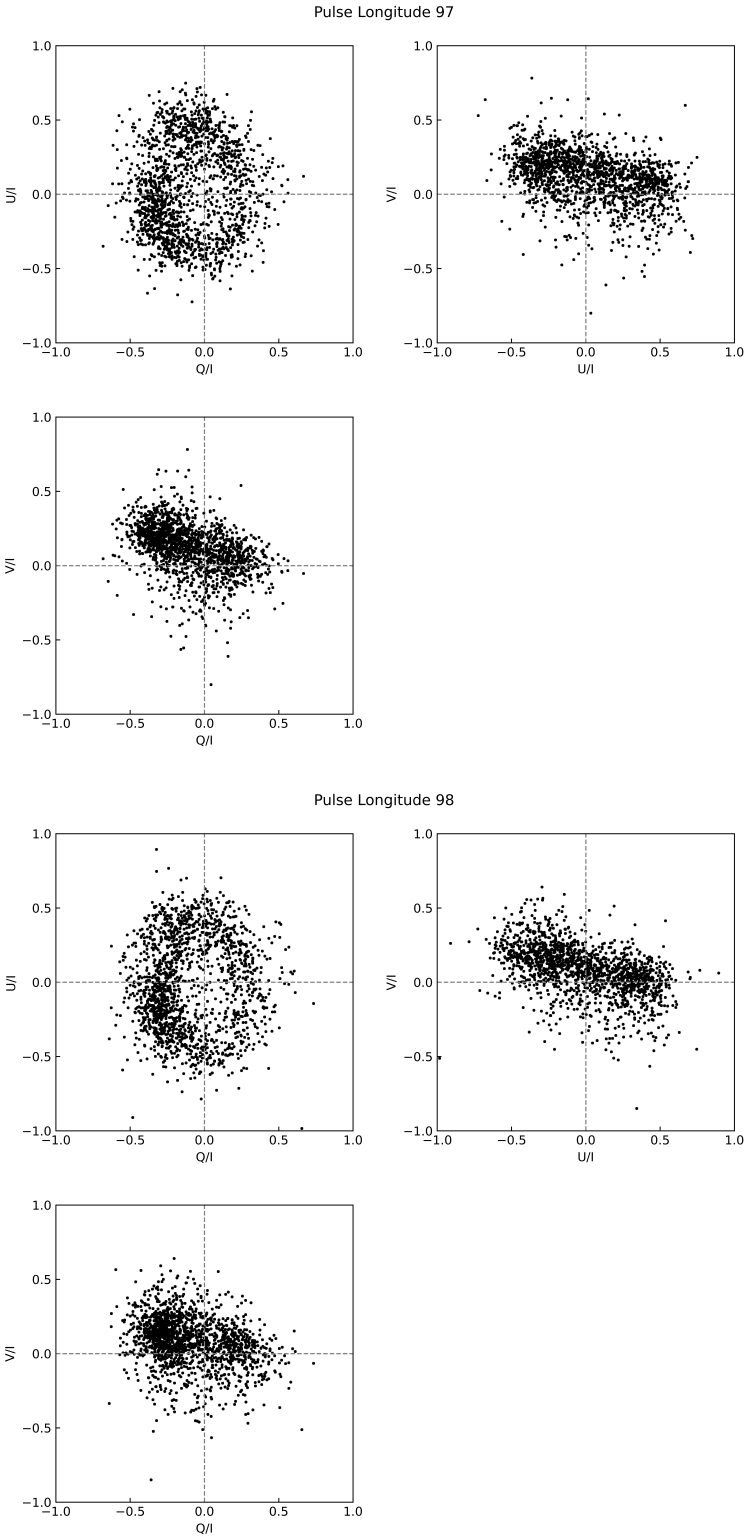

Figure C.2: Unexpected toroidal distribution of the Stokes polarisation vector at pulse longitudes l = 97 and l = 98, presented as two-dimensional projections onto the major planes of $\boldsymbol{p}$-space.

Appendix D

Simulation of the Double Modulations

In order to explain the observable properties of the quasi-periodic pulsar signal in the LRFS and PLRFS, we simulated the incoherent superposition of the orthogonally polarisation natural modes in total intensity and polarisation. The variables of the simulation are the sub-beam separation (T) and amplitude of the modes. Panels on the left have a sub-beam separation of T = 5, and panels on the right have T = 3.

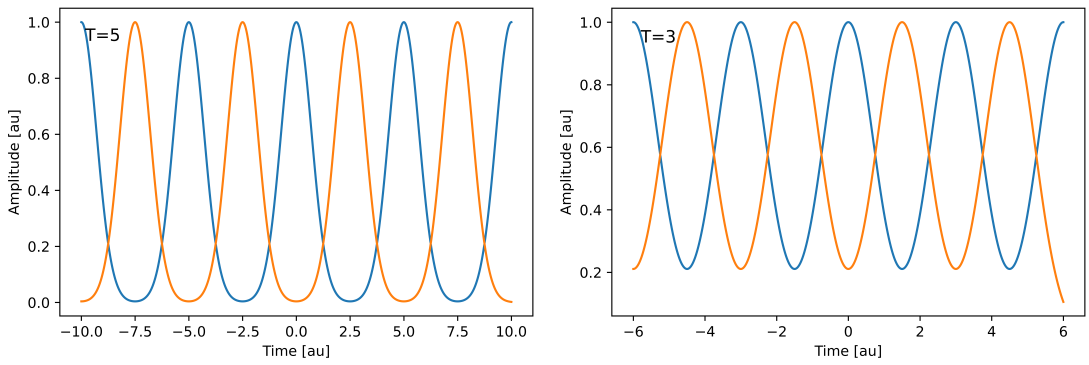

Figure D.1: The blue and orange solid lines represent mode A and B, respectively, of the total intensity.

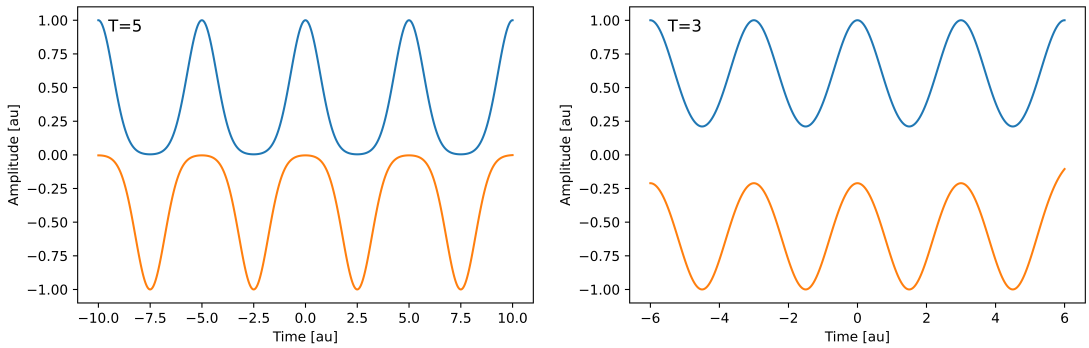

Figure D.2: The blue and orange solid lines represent mode A and B, respectively, of Stokes Q.

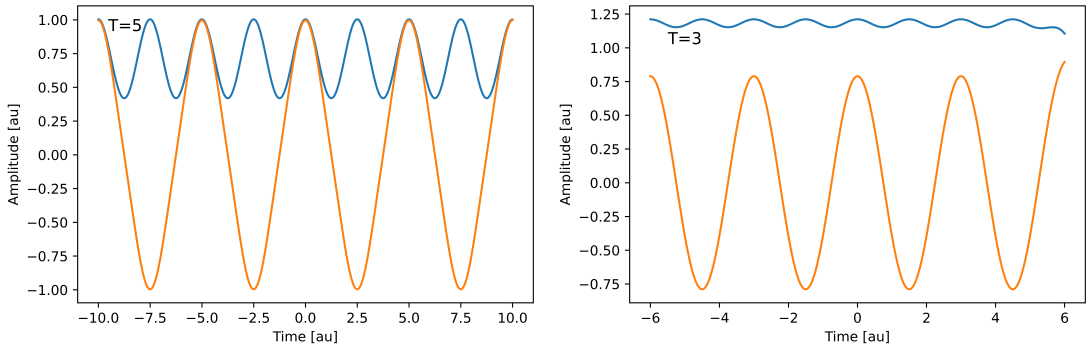

Figure D.3: Incoherent superposition of mode A and B. The blue and orange solid lines represent the total intensity and Stokes Q, respectively.

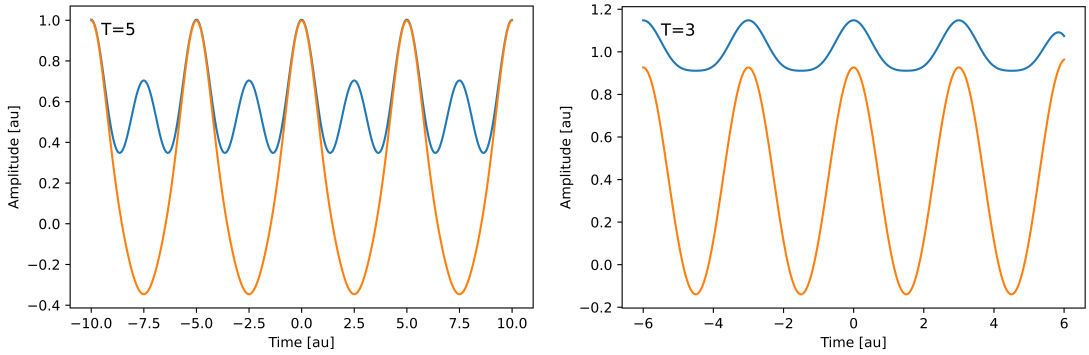

Figure D.4: Incoherent superposition of mode A and B, where the modes have unequal amplitudes. The blue and orange solid lines represent the total intensity and Stokes Q, respectively.

Appendix E

Nomenclature

The following is a glossary of mathematical symbols and acronyms used in the thesis. Bold parameters indicate vector quantities.

FFT Fast Fourier transform

Harmonic Spectral bin in a fluctuation power spectrum

LRFS Longitude-resolved fluctuation spectrum

PLRFS Polarisation longitude-resolved fluctuation spectrum

PFCS Polarisation fluctuation cross spectrum

PFCM Polarisation fluctuation coherency matrix

SLRFS Stokes longitude-resolved fluctuation spectrum

SEFD System Equivalent Flux Density

t Pulse number, time

N_t Total number of pulses in the dataset

T Pulse-data segment

N Number of pulses in a pulse-data segment

N_T Number of pulse-data segments

$N_{\rm step}$ Number of pulses between each pulse-data segment

$g(t)$ Gain

S_{tl} Intrinsic intensity of the pulsar

P_{tl} Total pulsar signal

P_1 Pulsar spin period

P_2 Sub-pulse separation in pulse longitude

P_3 Drift period, vertical separation between drift bands in a pulse stack

P_4 Period of the oscillating drift period

ν_3 Drift frequency

f_3 Relative drift frequency, $\nu_3 \cdot P_1$

f_4 Frequency of the varying drift frequency, $1/P_4$

I Total intensity, Stokes I

$\boldsymbol{p}$ Stokes polarisation vector

Q Stokes Q, linear polarisation, +horizontal and −vertical

U Stokes U, perpendicular/diagonal linear polarisation, $+45°$ and $-45°$

V Stokes V, circular polarisation, +RH and −LH

L_{Tkl} LRFS

$\boldsymbol{P}_{Tkl}$ PLRFS

k Harmonic bin

K Set of all harmonics in a fluctuation spectrum

K_+ Set of harmonic bins in the analytical signal

K_{on} Set of all on-signal harmonics that correspond to the quasi-periodic signal

K_{off} Set of all off-signal harmonics that do not correspond to the quasi-periodic signal

$K' = (K_{\text{on}} \cup K_{\text{off}}) \subset K$ Subset of all harmonics included in the analysis

$K_{\text{excl}} = \overline{(K_{\text{on}} \cup K_{\text{off}})} \subset K$ Subset of all harmonics not included in the analysis

l Pulse longitude bin

ϕ Pulse longitude in degrees (Primak et al., 2022)

Φ Set of all pulse longitudes in a pulse

Φ_{on} Set of all pulse longitudes that correspond to the on-pulse window

Φ_{off} Set of all pulse longitudes that do not correspond to the on-pulse window

$\boldsymbol{P}$ Complex vector

$\boldsymbol{A}$ Real-valued vector, real part of the complex vector $\boldsymbol{P}$

$\boldsymbol{B}$ Real-valued vector, imaginary part of the complex vector $\boldsymbol{P}$

$\mathbf{C}_l(\kappa)$ Longitude-resolved PFCM

$\boldsymbol{S}_{kl}$ Longitude-resolved PFCS

$S_{kl\mu}$ SLRFS

$S_{k\mu}(T)$ On-pulse Stokes fluctuation spectra as a function of time